Study into Surface Properties of
Plasma Nitrided and Laser Melted Workpieces

by

Mahmoud A. Mohammed, BSc. & MSc. in Petr. Eng.

Ph.D.   **1998**

Study into Surface Properties of
Plasma Nitrided and Laser Melted Workpieces

by

Mahmoud A. Mohammed, BSc. & MSc. in Petr. Eng.

This thesis is submitted to Dublin City University as the fulfilment of the
requirement for the award of degree of

Doctor of Philosophy

Supervisors

Professor M.S.J. Hashmi

Professor B.S. Yilbas

School of Mechanical & Manufacturing Engineering
Dublin City University

September 1998

DECLARATION

I hereby certify that this material, which I now submit for assessment on the programme of study leading to the award of Doctor of Philosophy is my own work and has not been taken from the work of others save and to the extent that such work has been cited and acknowledged within the text of my work.

Signed: _____   **I.D No.:**   95971262

Date: 31st August, 1998

This thesis is dedicated to my beloved Mother
Wife, Teachers, Brothers, Sisters, Daughters and Son

ACKNOWLEDGMENT

Title of Thesis: Study into Surface Properties of Plasma Nitrided
and Laser Melted Workpieces.

Name of Student: Mahmoud A. Mohammed   **Student No:** 95971262

ABSTRACT

The present work was carried out to study the surface properties of plasma nitrided, TiN PVD coated and laser-melted Ti-6Al-4V workpieces. The work consists of two phases. The first phase of the study was conducted to investigate the tribological and mechanical properties of plasma nitriding and TiN PVD coating of Ti-6Al-4V alloy. Specimens were nitrided in a N_2/H_2 (8/2 ratio) plasma. Workpiece temperature was varied from 450-520°C during the nitriding process. Pin-on-disc wear tests were carried out to evaluate the wear properties of the resultant samples and ball-on-disc experiments were conducted to measure the friction coefficient. Micro-hardness tests, SEM, EDS and XRD were carried out to investigate the phases developed in the nitrided zone. It was found that the wear resistance improved considerably after the nitriding process. Three distinguished layers were identified. These include an inner layer, where δ–TiN + ϵ–Ti_2N phases formed, an intermediate layer, where α–TiN with or without ϵ–phase developed and an outer layer, where precipitation was dominant.

In the second phase, the surface properties of the Ti-6Al-4V alloy due to laser melting after plasma nitriding process was investigated. A CO_2 laser with nominal output power of 1.6 kW was employed to melt the nitride layers. In order to achieve low and high melting regions, the laser output power intensity was varied. It was found that the laser melting altered the friction coefficient considerably as compared to untreated samples. The microstructures were analyzed before and after the laser melting process using SEM microphotography. It was found that the scratch developed at the untreated surface was deeper than those compared to plasma nitrided and nitrided/laser-melted surfaces. A mathematical model governing the laser melting process was developed using a Fourier theory, which permitted the heating and cooling rates to be predicted.

Table of Contents

CHAPTER – I

CHAPTER – II

Equipment and Procedure

CHAPTER – III

Heat Transfer Modelling

CHAPTER – IV

Results and Discussions

CHAPTER – V

Conclusions and Future Work

References

Papers in Conference & Journal

LIST OF TABLES

LIST OF FIGURES

NOMENCLATURE

A,B   :   Constants of integration

A_b :   Absorption factor

b   : $\dfrac{V}{2\sqrt{\alpha}}$

c   : $b - \delta\sqrt{\alpha}$

C_p :   Specific heat capacity (J/kgK)

h   :   Heat transfer coefficient

I_0 :   Peak of power intensity of laser beam (W/m^2)

I   :   Power intensity of laser beam (W/m^2)

k   :   Thermal conductivity (W/mK)

k_B :   Boltzmann's constant

L   :   Latent heat of fusion (kJ/kg)

L^{-1} :   Inverse Laplace transformation

p   :   Laplace transform variable

$q^2\alpha$

R   :   Surface reflectance

Sq   :   Energy generation rate per unit volume

t   :   Time (s)

T   :   Temperature (K)

Ts	:	Surface temperature (K)
V	:	Instantaneous velocity of evaporating front (m/s)
x	:	Distance from the surface (m)
α	:	Thermal diffusivity (m^2/s)
		$\dfrac{k}{\rho C_p}$
δ	:	Absorption coefficient (1/m)
ρ	:	Density (kg/m^3)
θ	:	The temperature rises above the initial temperature $= T - T_0$

CHAPTER- 1

1.1 INTRODUCTION

The surface treatment of engineering materials has developed rapidly in recent years. Surface engineering technology is being used to reduce the cost arising due to the deterioration of engineering components in service by providing acceptable service life, reduced downtime costs and the opportunity, where possible, to repair the part after use by re-surfacing. The cost to industry of any destructive forms of attack is high and recognition lies behind the continuing development of the technology known as surface engineering, which includes applications of coatings to metal surfaces to improve their performance in specific working conditions. A coating must be selected according to the physical, chemical and biological characteristics of the environment. It should also be free from defects, pinholes and mechanical damage. In all cases, it is important to provide a good physical bond between a coating and the surface. In many of these applications, surface coatings are used to enhance the functional properties of the surface. As a result, development is continuing and taking place in all directions [1-3].

Surfacing technology includes welding, thermal spraying, surface treatments, electro-deposition and vapour deposition. To begin with the first method for treating a surface is by welding and a wide range of materials is available for welding coatings. Welding provides the highest bond strength between the deposit and the substrate. It is capable of applying deposits of considerable thickness, if required. In addition, welding can be operated manually or be mechanized and programmed. Welding processes involve application of some heat to the component, depending on the material from which it is made and its condition. The coating material is raised to its melting point during melt surfacing, which means that the metals and alloys used must have a melting point less than, or equal to, that of the substrate.

Thermal spraying provides an excellent and reliable service in applications such as aircraft gas turbine engines. Using this process both the weldable and non-weldable materials, such as ceramics, can be deposited. In all thermal-spraying processes, the consumable coating material fed to the spray gun is raised in temperature and projected in a particular form to strike the workpiece. On arrival, the hot particles form splats which interlock and gradually build up a coating of the desired thickness. The consumables used are available as solid drawn wire for metallising processes and in powder form for high-energy processes.

Electro-deposition is a well-established process for applying metallic coatings to improve surface properties of materials used in engineering practice. In theory, there is no limit to the thickness to which many metals and alloys can be electro-deposited. Process economics is an important factor due to the cost and speed of the process compared with other surfacing methods. The low temperature of deposition provides

2

advantages of low distortion, better access to internal surfaces and accurate control of deposit thickness. The electro-deposition process can be successfully used to deposit thinner engineering coatings, thus offering considerable scope and flexibility to the designer. Electro-deposition is used extensively, not only to apply coatings to new components, but also to restore the dimensions of parts, which have, either become worn in service, or which have been over-machined and, therefore, are outside the required tolerances.

Vapour deposition provides a limited range of coating material possibilities, but can be used with materials difficult or impossible to apply by other techniques or to produce thin coatings of controlled thickness. The involved methods are used for producing overlay inorganic coatings, which are formed on the surface of a substrate by condensation or reaction from the vapour phase. The two techniques are Physical Vapour Deposition (PVD) and Chemical Vapour Deposition (CVD) [14]. The methods of PVD are vacuum deposition processes and gas sputtering processes. The PVD coating techniques are almost wholly confined to the production of relatively thin films (ranging from 10^{-7} to 10^{-4} m), whereas CVD is used for both thin films and for coatings in excess of 1 mm. The PVD techniques are many and varied and include warm or hot treatment in vacuum, whereas CVD employs at least two highly reactive gases, which generate the coating by high temperature reaction, either in the gas phase or on the substrate. All vapour deposition processes involve treatment in a vacuum chamber, or in one, which can withstand the high temperature, and corrosive gases. This limits the size and shape of the object to be coated but this limitation is imposed by the capital expenditure involved rather than by any fundamental characteristics of the process [5].

PVD coating vapours are generated either by evaporation from a molten source, or by ejection of atoms from a solid source which is undergoing bombardment by an ionized gas (i.e., sputtering). The vapour may then be left as a stream of neutral atoms in a vacuum evaporation, or it may be ionized to a greater or lesser extent. A partially ionized stream is usually mixed with an ionized gas and deposits on an earthed or biased substrate (ion plating and sputter coating), but a highly ionized stream, which forms plasma, is attracted to a biased substrate (arc plasma evaporation). Alternatively, a 100% ionized beam may be focused and accelerated to sufficiently high energies to penetrate into the substrate (ion implantation) [6-11].

No vapour deposition method gives an adhesion acceptable for engineering purposes, unless the substrate is truly clean. The standard of cleanliness involves removal of contaminated layers. As such preparation is done in air, the most appropriate technique is ion bombardment. The ion bombardment cleaning is performed by a low-pressure gas discharge. The work chamber contains argon and the workpiece is made negative with respect to earth. Positive argon ions generated in the discharge are accelerated to the workpiece at high energies and eject surface atoms when they impact. The substrate is thus cleaned by an erosion process which 'sputters' contaminant and substrate atoms into the chamber. On the other hand, CVD processes normally require that only the substrate be properly degreased and are free from obvious oxide films. A cleaning cycle involving reducing gas at elevated temperatures is required before the coating process begins [5,12].

Most metals, alloys, ceramics and some intermetallic compounds can be applied as coatings either individually or as mixtures, but their characteristics often

limit the processes. The material/process relationship does not only identify where they can be used together, but also determines their properties, which can be expected from the coatings, such as density and adhesion to the substrate. It is important to clearly define the area to be treated in order to obtain optimum results as actual positioning of the coating. The surface treatments are, therefore, aimed to provide resistance to various forms of wear and/or corrosion, possibly over a wide temperature range [13-15].

The principal characteristics of the processes, which distinguish one method from the other methods of the surface treatment, are the coating thickness, adhesion to substrate, range of the processes and resurfacing. Although there is a lot of overlap between the characteristics of the various processes in terms of the coating thickness, coating rate, coating materials and the areas of application, it is difficult to make direct comparisons because so much depends upon the applications involved. Moreover, many of the processes are in an active stage of their evolution and the suitability of a particular technique for any given application may change dramatically with the advent of new development [16-18].

Coating thickness is often determined by the application and not by the process capability. The thickness of the coating material is normally consistent with the amount of destructive forms of attack, which can be permitted before the component is no longer fit for use. Comparison of coating rates for a given material is complicated by the fact that different processes use different source to substrate distances. Virtually all process rates can be increased by a multitude of sources and by an increase in the power input, but the coating quality may suffer if too high a rate is

5

attempted. Direct comparison of the coating cost is not generally possible, but a broad generalization can be made. In addition, correctly selected materials and properly operated processes provide a metallurgical bond to the substrate, which withstands thermal and mechanical shock without detachment. Moreover, most processes are used for the application of surface coatings, bringing the operation within the scope of most engineering activities and enabling on-site work to be carried out in certain circumstances. Furthermore, the opportunity to carry out repairs on worn parts, whether previously coated or not, is a feature exploited in many industries [19-21].

Notwithstanding the continuous efforts in developing advanced processing methods or new findings in surface modification, the basic understanding for the appropriate assessment of surface layers still remains very challenging. In this regard, plasma nitriding or ion nitriding has been a well-known technique for many years. Although the process is well-developed, several scientific questions on the basic understanding of the process and limits concerning its upscaling for industrial use still remain to be investigated [22-24].

Plasma nitriding, plasma carburizing and plasma carbonitriding are the most frequently used plasma diffusion techniques for the surface treatment of various mechanical parts in industry [25]. The basic concept in using ion implantation to improve the surface properties of a titanium alloy is the possibility of forming nitrides or carbides below the surface by means of either nitrogen or carbon ions. Titanium nitrides and carbides are hard materials, which can improve the tribological properties of the surface, i.e., increase the wear resistance and surface hardness. It has been demonstrated that when nitrogen forms a solid solution as a consequence of

implantation in titanium, it results in the hardening of dislocation-pinning effects [26,27].

Titanium and steels with alloying elements are suitable for thermal and plasma nitriding [28]. Two major methods are generally used for titanium nitride synthesis, abbreviated for simplicity as TiN: (a) TiN molecules are formed in the gaseous phase and then deposited on a substrate; (b) nitrogen atoms are allowed to diffuse into the titanium matrix. With regard to TiN deposition, two techniques can be utilized, i.e., PVD and CVD. In both techniques titanium reacts with nitrogen in the gaseous phase to form TiN. The formation of TiN molecules can occur either in the gaseous phase or on the surface. The first process involves excited states of both titanium atoms and nitrogen molecules, while the second mechanism involves a recombination reaction between Ti and N atoms on the surface [29,30].

Titanium and its alloys are widely used in industry owing to their outstanding properties, which include light weight, excellent strength-to-weight ratio and high corrosion resistance due to their electro-negative potential [31-33]. Consequently, Ti and its alloys such as Ti-6Al-4V have been used in the aerospace industry as well as in the chemical and automobile industries. Since the tribological properties of these alloys are quite poor [26,34], they require some form of surface treatment in engineering applications such as gears and bearings. In order to improve the tribological properties, many surface engineering techniques (e.g. plasma nitriding and ion implantation, thin film oxidation coating, laser and electron beam treatment) have been applied to the surface of titanium and its alloys. Titanium, with alloying elements such as aluminum, chromium, molybdenum, vanadium and tungsten, is

suitable for thermal and plasma nitriding [35-37], since these elements have a strong affinity for nitrogen, which in turn plays an important role in surface hardening [28,38].

Multiple treatment of a surface may introduce properties that are unobtainable through any single surface treatment process [39-41]. The ferrous alloys can be hardened to considerable depths through solid-state thermo-chemical diffusion treatments. This technique however, is not yet available for titanium alloys with deep penetrated layers. In this case, the use of a high-energy beam may appear to be the most promising tool for deep penetration for surface melting or alloying. The need for a deep case in components being in contact is due to the development of the maximum shear stress in a substance at some depth below the surface [42]. Many factors affect the shear stress distribution (including contact geometry, the elastic moduli etc.). Consequently, changing the mechanical properties of the sub-surface may influence the surface properties. Increasing the strength modulus of the sub-surface causes an increase in holding the maximum shear stress. Laser heating is, therefore, a potential candidate to improve the load-bearing ability of the primary treated surfaces [43,44]. The presence of an alloying substance alters the nucleation conditions, but basically the experience gained in re-solidification processes can be applied. The laser offers the possibility of various types of surface treatments. The properties of a laser beam provide the formation of the micro-structures and hence the desired characteristics can be achieved by alternative methods. Laser melting of a surface, therefore, becomes necessary [45,46].

1.2 LITERATURE REVIEW

Field experience with TiN-coated cutting tools over the last few years demonstrated their increased performance compared to non-coated tools. A large number of laboratory pin-on-disk tests were performed by Malliet et al. [47] to investigate the specific interaction between TiN and a chromium steel counter-body. Based on an analysis of the wear track appearance, the friction coefficient and the wear debris, two wear modes were identified. The occurrence of these wear modes and a transition between them were analyzed as a function of the surface roughness of the TiN coating and the normal load applied. It appeared that two wear modes were predominant in a load-roughness plane. An adhesive transfer of steel material onto the TiN coating, resulting in a steel-steel wear system characterized wear mode-1. If the imposed normal load and/or the original roughness of the TiN coating is above a critical value, a mainly abrasive wear mode-2 appears after a varying time interval, and the actual wear is then a combination of both wear modes.

The effects of nitrogen ion implantation on the mechanical properties of metallic surfaces commonly encountered in machine building, such as electroplated hard chromium, sacrificial phosphate coating on cast iron, and plasma-face-coated hard molybdenum were studied by Fischer et al. [48]. It was found that ion implantation is capable of improving substantially the tribological properties of common mechanical parts without special pre-treatment. The standard production samples, with no special surface preparation prior to the treatment, were investigated. This made results immediately relevant to a production environment. In the parameter range explored, the treatment resulted in up to 31% wear reduction and 79% friction

coefficient reduction for the chromium surface; and up to 24% wear reduction and 13% friction coefficient reduction for the phosphate coating; and up to 90% wear reduction (to a tenth of the original value) and 84% surface hardness increase for the molybdenum deposit. The mechanisms responsible for the observed effects were discussed and the trends in the tribological properties as a function of ion energy and dose were defined. These results demonstrated the potential of employing ion implantation in industrial applications.

Friction tests were performed by Singer et al. [49] on TiN-coated substrates at low speed (less than 0.1 m/s) in air. Optical and scanning electron microscopy, Auger electron spectroscopy and transmission electron microscopy (TEM) were used to characterize the transferred films and debris generated during sliding against steel and sapphire balls. Friction coefficients were correlated with the formation of transfer layers, the accumulation of debris in wear tracks and the structure and composition of transfer films and debris. In addition, friction coefficient of steel against rougher ($R_a \sim$ 60-100 nm) TiN coatings started and remained relatively high (0.5-0.7) owing to wear and transfer of the steel. After the TiN coating was polished ($R_a \sim$ 4 nm), transfer was reduced and the initial friction coefficients ranged from 0.15 to 0.2. The initial friction coefficients with sapphire balls sliding against polished TiN were even lower. However, friction coefficients with both types of balls increased as debris formed and transferred to the wear track. Auger analysis showed that the steel balls accumulated metallic iron and/or iron oxide as well as titanium oxide layers and debris, whereas the sapphire balls acquired only titanium oxide transfer layers. TEM of debris stripped from contact areas of the steel and sapphire balls identified the phases of debris as a rhombohedral ternary oxide ($FeTiO_3/ \alpha-Fe_2O_3$) and rutile (TiO_2) respectively.

Chemical interaction between the transfer films led to an increase in the friction coefficient. Wear of TiN during low friction sliding took place in two stages. An air-formed oxide layer on TiN was transferred to the ball. Then, oxide debris was transferred back to the TiN surface. A thermo-chemical basis for oxide debris formation was given and the friction behaviour was interpreted in terms of an oxide wear mechanism.

The microstructure of Ti/TiN multilayer films deposited by hollow cathode discharge ion plating was studied by Huang et al. [50] using transmission electron microscopy and μ-μ-diffraction in combination with X-ray diffraction. It was found that the Ti/TiN multilayer films consisted of hexagonal α-Ti, tetragonal ε-Ti$_2$N and cubic δ-TiN. They had a clearly layered structure of Ti/Ti$_2$N/TiN/Ti$_2$N/Ti ..., with single layer thickness of titanium and TiN ranging from several to several hundred nanometers. Interfacial chemical reaction during deposition produced a Ti$_2$N transition layer between every adjacent pair of titanium and TiN layers. A transition layer of FeTi between the film and the substrate was observed, which resulted in good adhesion between the film and the substrate. Ti/TiN multilayer films had fibrous crystallites. The grain size of both titanium and TiN decreases with decreasing nominal single layer thickness of Ti/TiN films. The hardness of Ti/TiN films increases at first with decreasing nominal single layer thickness and then decreases.

Nitrogen ion implantation into titanium and Ti-6Al-4V was conducted by Mucha and Braun [51] at an acceleration voltage of 80 kV and with target temperatures between 30°C and 450°C during irradiation. It was found that the optimum wear characteristics were obtained at a temperature of around 450°C using

11

ball-on-disc tests. Auger electron spectroscopic and Rutherford backscattering surface analyses showed that there was a saturation dose above which no further nitrogen was retained in the material of the ion-implanted samples. The improved wear characteristics are attributed to precipitation of TiN, which is assumed to be promoted by the higher temperature employed. No dependence of the wear properties on the ion flux was observed within the range of ion beam current densities studies (i.e., 1-15 $\mu A/cm^2$), experiments in which no temperature control exists may result in mistaken interpretations since target temperatures rise with the increase in the ion beam flux.

The target temperature during nitrogen plasma source ion implantation of Ti-6Al-4V was estimated by Chen et al. [52]. The diffusion coefficient was measured by comparing measured nitrogen concentration profiles to Monte Carlo simulations. The high-temperature nitrogen treatment can increase the thickness of the implantation-affected zone from 2000Å to approximately 5000Å on Ti-6Al-4V. Auger electron results indicated that the affected zone of implantation was about 0.5 μm thick. Surface Knoop hardness improved from 400 to 900 HK for one gram applied load. The wear behaviour was studied using a pin-on-disk wear tester. The wear data showed a factor of 30 increase in wear lifetime. The failure criterion was chosen to be 1 μm wear depth. After high-temperature nitrogen treatment, the wear behaviour of Ti-6Al-4V was as good as that of cobalt-chromium alloy.

The effect of ion implantation on the friction and wear behaviour of 304 stainless, AISI 1010 and D2 tool steels was investigated by Mehrotra et al. [53]. The stainless steel specimens were implanted with approximately 20% N, and those of 1010 and D2 tool steel with approximately 20% Ti and 14-20% C. The ion-implanted

specimens were characterized using XRD, optical microscopy, Auger electron spectroscopy and wavelength dispersive X-ray spectroscopy. The friction and wear tests were performed on ball-on-disk and pin-on-disk machines. In the pin-on-disk tests, the ion-implanted pin specimens were rubbed against steel (heat treated to Rc 62-64) disks lubricated with tool and instrument oil. In the ball-on-disk method, the disk specimens were rubbed against 440 C steel balls under dry conditions. Scanning electron microscopy of the wear tracks on disk specimens was performed to investigate the wear mechanism. The results indicated that wear rates of the Ti + C implanted specimens of 1010 and D2 tool steel were lower than those of the non-implanted specimens. Mixed results were obtained for the effect of nitrogen implantation on the wear of 304 stainless steel.

Various potential surface treated materials paired with multiple cathodic arc plasma deposition TiN coated specimens, to be used for screw and rollers, were tested by Su et al. [54] on an oscillating wear machine under reciprocating wear conditions. The processing parameters of the TiN coatings, including the bias voltage, arc current and partial pressure of N_2 was optimized before the wear testing. The polishing pre-treatment of the substrate yielded the highest wear resistance. The indentation test showed that adhesive strength decreased with increasing coating thickness. If the coating was too thin, it was easily worn through. The optimum coating thickness was 3 μm. It was concluded that PVD coated TiN paired with surface treated specimens possessed less wear resistance under HD150 and base oil lubrication. Under water-based cutting fluid, the self-mated TiN and TiN-surface treated specimen pairs showed no measurable wear, only surface polishing on the TiN surface was noticed. They were potential sliding pairs for TiN coating in machine element applications.

The wear mechanisms of TiN included local flaking of the coating layer at the edge of the wear scar, surface polishing and surface pitting under oil-lubricated wear. The wear mechanisms under dry wear resulted in a residual TiN unworn layer with or without a transferred layer. The exposed substrate region covered with a transferred layer in suitable sliding pairs were self-mated TiN and TiN-surface treated specimens under cutting fluid lubrication, and carburized specimens paired with TiN coated specimens under base oil lubrication.

Ball-on-disc experiments were performed by Vancoille et al. [55] under dry sliding ambient conditions to characterize the tribological of TiN, (Ti, Al) N, and Ti(C, N) coatings. The coefficient of friction and the wear resistance against a corundum counterbody were determined as a function of the coating composition and the sliding speed. The wear of the (Ti, Nb)N coatings were found to be comparable to that of the TiN coatings and this was related to the formation of a similar type of oxide in the tribo-contact. In the case of the (Ti, Al)N coatings, the wear volume increased markedly as the aluminum in the coating increased, and the tribo-oxide formed was found to be Al_2TiO_5. Ti(C, N) coatings, which exhibited an extremely low, wear because of the low coefficient of friction. A mild-oxidational wear model was found to give a qualitative fit to the experiments. Measuring the coating wear as a function of the sliding speed opened the possibility of calculating the activation energy for the tribo-oxidation processes of thin coatings.

Su and Lin [56] investigated, through wear testing, the potential for carburized and nitrided surface treated steels and the TiN, CrN and TiN + CrN physical vapor deposited (PVD) surface treatments to be used in the screw and rollers of the variable

14

lead screw transmission mechanism (VLSTM). Indentation test results revealed that the thicker the PVD CrN coating, the lower was its adhesive strength, with the desired coating thickness being 10 μm. Surface treated steels (upper moving specimen) paired with PVD coated parts possessed very poor wear resistance under base oil lubrication, even worse than under dry wear. Suitable sliding pairs for VLSTM applications included: surface treated steels paired with either SKH51 or PVD coated specimens under cutting fluid lubrication; PVD coated specimens paired with SKH51 specimens under cutting fluid lubrication; and PVD coated specimens paired with PVD coated specimens under base oil and cutting fluid lubrication.

The wear mechanism of high-speed steel coated with TiN by arc ion plating during sliding against alumina and AISI 52100 steel under lubricated conditions was experimentally investigated by Yoon et al. [57]. The results showed that a transition in the wear behaviour occurred after a defined period of sliding time for both of the countermaterials. Examinations of samples showed that the wear transition mechanism differs, however, depending on the countermaterials. When slid against alumina, which was harder than the coating, the coating wore slowly by abrasion in the initial stage until the substrate was exposed, this led to the onset of rapid substrate abrasion in the following wear stage. The time required for this transition did not relate to the substrate hardness but increased with increasing coating thickness and decreasing applied load. On the other hand, when slid against AISI 52100 steel, which was softer than the coating, the coating did not wear significantly in the initial stage, but delaminated abruptly after a definite sliding time only under heavy loads. The time required for this delamination increased with increasing substrate hardness and decreasing applied load, and there existed an optimal coating thickness for the

delayed coating delamination. It was suggested that severe plastic flow in the form of twins observed in the substrate at the vicinity of the interface could play an important role in this coating delamination.

Shehata et al. [58] used a 400 W pulsed Nd:YAG laser to alloy BN and Ti/BN on AISI M2 steel using hexagonal BN powder and Ti foil (25 μm thickness). The clearance (flank) faces of the single-point tool were lasers alloyed using BN and Ti/BN. Optical metallography, scanning electron microscope, Vicker's microhardness and X-ray diffraction were employed to characterize the alloyed layers. The depths of the laser-alloyed zones of BN- and Ti/BN-alloyed tools were about 140 μm and 260 μm respectively. The hardness of the laser-alloyed layer with BN was about 640 HV while that of the alloyed layer with Ti/BN was about 680 HV. The alloyed layers were free from cracks and porosity. Both the alloyed and unalloyed tools were then tested on a 14.7 kW engine lathe to turn AISI 1045 steel workpieces. The results indicated that the tool life of BN-alloyed tools was about 200% higher than that of the unalloyed tools, while the tool life of Ti/BN-alloyed tools was about 260% higher when the tool life criterion was chosen as 0.3 mm flank wear. Also, about 30% and 50% for BN-and Ti/BN-alloyed tools reduced the tool wear rate, respectively. The reduction in tool wear of the alloyed tools was attributed to a reduction of the chip-tool contact length and to the different chip formation mechanisms. Consequently, the friction coefficient between the tool and the workpiece material was reduced.

Stappen et al. [59] pointed out that it is possible to optimize the adhesion of a TiN coating on some pre-nitrided tool steel surfaces. Two industrial applications were chosen to demonstrate the possibilities of tools treated by the duplex process. A steel

milling tool consisting of 14 high speed teeth and knives made of M2 tool steel for tube cutting were plasma nitrided and subsequently PVD coated. Applying different intermediate steps between the nitriding and coating processes could obtain a good coating adhesion. Scratch tests were used to evaluate the adhesion behaviour of both coating systems. After producing a certain number of workpieces, the laboratory performance of the duplex treatment was compared with tool wear and lifetime evaluation data from industry. It was found that the duplex treatment gives a much better wear resistance for both applications, resulting in a reduced cohesive failure pattern. Extrapolation of laboratory performance to industrial conditions seems to be possible if a close collaboration between industry and research groups is set up.

A test machine with a thrust-washer adapter was used to carry out experiments by Lin and Horng [37]. A rotating upper specimen was pressed against a stationary lower specimen. This setup was employed to simulate the surface contacts between the steel (of the ring) and the titanium nitride coating (on the washer). The existence of an electroless nickel interlayer on the washer was also investigated. The effect of the coating layers on the tribological behaviour was evaluated for different thickness combination of the titanium nitride layer (top layer) and the electroless nickel layer (interlayer). The interlayer was found to increase the wear volume, but was advantageous for strengthening resistance against chemical corrosion. The wear volume was controlled by the thickness of the two coating layers. A thicker TiN layer in conjunction with a thinner interlayer constituted the appropriate combination for two coating layers from the viewpoint of lowering the wear volume. The friction coefficients arising from the TiN coating generally varied in the narrow range between 0.5 and 0.55, regardless of the interlayer thickness. The applied load and the

17

sliding speed affected both the friction coefficient and the wear volume very much. In the test operating conditions, the primary wear mechanisms of the coating layers, such as micro-abrasion, semicircular or curved cracking, plucking and grooving, characterized the surface failures. The surface failures due to friction and wear that occurred within the top layer appeared to be nearly independent of the adhesive strength of the interface.

A ball-on-disc testing machine was used by Huang et al. [60] to investigate the sliding friction behaviour of PVD TiN, CrN and (TiAl)N coatings against steel under both dry and lubricated conditions. Different applied loads and sliding speeds were employed. The initial transient state and the steady state characterized the curves of friction coefficient versus sliding distance for the coatings was investigated, and the friction behaviour during the initial transient state and the steady state could be determined. The results showed that (TiAl)N coating which had the highest hardness and surface roughness exhibited the highest friction coefficient under both dry and lubricated conditions and vice versa. The friction coefficient of all investigated coatings could be significantly reduced by lubrication.

Hogmark and Hedenqvist [61] presented the methods used for mechanical and tribological characterization of thin, hard coatings. The tribological tests included dry sliding wear, solid particle erosion and micro-abrasion. In addition to tribological characterization, the thickness, hardness, adhesion, and residual stress state were assessed. The survey showed that the tribological performance of a coating could not be predicted by one single parameter. A general tribological characterization of a coated component had to encompass several reproducible lab tests to obtain a

tribology profile. The performance of the best combination for any given application could be achieved.

Dingremont et al. [62] commented on multifunctional coatings combining a nitriding treatment and physical vapour deposition to allow the performance of cutting and forging tools to be boosted. The improved mechanical support of the coating makes them withstand higher loads. This treatment was used for wear parts made from construction steels to increase their fatigue and wear resistance. Hard coatings applied on nitrided layers could replace or enhance the e or g' layers currently used. These treatments were made in a discontinuous mode using dedicated equipment for the nitriding and coating treatment or in a continuous mode, i.e. directly in the coating reactor. These treatments were applied and optimized for construction steel 35NCD16 and hot working steel Z38CDV5-1. Coating conditions had a decisive impact on the thermal stability of the iron nitride layers. This aspect was studied and several technical solutions were identified. Finally, it was shown that in contradiction to previous findings the coatings had only a negligible influence on the stress intensity in the nitrided zone.

Muller et al. [63] studied the interface fracture toughness and the fracture energy of the coating systems of TiN on high speed steel (HSS), and titanium on austenitic steel, copper and HSS that were measured by three-point bend test. The interface fracture toughness and especially the fracture energy can be used to characterize the adhesion strength of a coating system. The coatings were produced by a magnetron sputtering process. The average thickness and a negative bias voltage were chosen to show the effects of the process parameters on the fracture energy. The

mechanical data were compared with micro-hardness and scratch test data obtained from samples subjected to an identical treatment. The results demonstrated that the trends of the experimental data observed with different testing methods differ significantly, since the contribution of the interface and bulk properties of the coating and the substrate material were different.

The oxidation behaviour of the CrN and TiN hard coatings prepared by reactive sputtering at 200 °C was studied by Milosev et al. [64] using X-ray photoelectron spectroscopy (XPS). The formation of thin surface over-layers on top of the nitride coatings was observed even at room temperature. At elevated temperatures the mechanism of nitride oxidation proceeds by a progressive displacement of nitrogen by oxygen. At sufficiently high temperatures a tendency towards phase separation between the nitride and oxide was observed, resulting in the formation of Cr_2O_3 and TiO_2 layers, respectively.

Alonso et al. [65] investigated the effect of C^+, N^+ and O^+ light ions implantation on the properties of Ti-6Al-4V alloy. Energies from 50 to 180 keV and doses of the order of 10^{17} ion cm^{-2} were used by keeping the substrate temperature below 500°C. Mechanical properties were evaluated by means of micro-indentation tests with a loading and unloading cycle at loads up to 10 mN. An increase of more than 100% in the surface hardness was observed in most of the implanted samples. Pin-on-disc wear tests under lubricated conditions were carried out to evaluated and compare the tribological behaviour of implanted samples against ultrahigh molecular weight polyethlene. A decrease in the friction coefficient from 0.1 to 0.05 was observed due to ion implantation. Unlubricated wear tests using an alumina ball on a

Ti-6Al-4V disc were also performed. Optical profilometry and scanning electron microscopy showed that implantation can improve the abrasive wear resistance by two orders of magnitude. X-ray photoelectron spectroscopy analyses showed the presence of hard phases such as oxides or carbides in the implanted samples.

Larsson et al. [66] presented the development of multilayered coatings with increased fracture resistance, retained hardness and adhesion to the substrate. One way of obtaining this effect was to deposit multilayered coatings consisting of alternating thin layers of hard and softer, more ductile materials. A modified commercial PVD deposition process was used for the deposition of multilayered Ti-TiN coatings on both high speed steel (HSS) and cemented carbide (CC) substrates in order to explore this idea. The multilayer coatings were evaluated with respect to fundamental properties such as morphology, microstructure, hardness, adhesion and fracture resistance. The deposition process was found to yield well-adhered coatings with an increased fracture resistance due to the multilayered structure, on both HSS and CC substrates.

Ma et al. [67] carried out a study to establish the mechanical properties of single and multilayer hard coatings. However, the mechanisms of deformation, cracking and delamination of coatings under ploughing and shear stress were not fully understood. A fractured cross-sectional specimen preparation technique through hardness indentation and scratch tests on hard coatings was used in conjunction with high resolution SEM to observe the deformation and fracture behaviour occurring as a result of these tests. TiN and T-TiN multilayer coatings were deposited on M2 high-speed steel and silicon substrates using an unbalanced magnetron sputtering system.

Hardness measurements and scratch tests were performed to monitor the mechanical properties. X-ray diffraction was used for phase identification. Coatings comprising fine columnar TiN behaved like closely congregated strong fibers: they were found to accommodate a large amount of ploughing and shear stress through densification and shear deformation. On increasing the load above a certain value, rupture of heavily deformed TiN initiated at defect locations and the cracks propagated and coalesced into macro-cracks. When the applied load was increased to near the critical load, the close packed columns separated from each other and detached from the substrate, resulting in total failure. For Ti-TiN multilayers, hardness and critical load were related to the different monolayer thickness of the Ti and TiN. The Ti layers dissipate most of the energy by means of shear deformation during the scratch test. At higher scratch loads, cracks occurred at Ti-TiN interfaces or multilayer-substrate interfaces depending on the relative interface strengths.

Bienk et al. [68] studied the tribological properties of physically vapour deposited coating of TiN, TiAlN and CrN deposited on discs made of two different tool steels using different pin-on-disc test procedures. The wear resistance was determined by using an Al_2O_3 ball while the friction properties were studied by using a flat steel pin under low load. By a step-load test using a steel ball, the seizing and adhesive wear investigated. The results showed that all the tested PVD coatings improved the performance of the samples, reducing seizing and wear considerably. TiAlN exhibited the most stable friction and wear mode and best properties compared with TiN, TiCN and CrN under conditions where unlubricated friction and severe seizing against steel occur. This is attributed to a stable aluminium oxide surface layer. The wear tests against Al_2O_3 showed that the Ti-based coatings reduced the

severe wear of the uncoated hardened steel by about 4 times while the softer but more ductile, CrN, reduced the wear by a factor of 2. In particular, the results for TiAlN seem to be in very good accordance with practical results from field tests. If proper test procedures are applied, the pin-on-disc test can make up a relevant and convenient test method for evaluating some of the fundamental tribological properties of PVD coatings.

The erosion-corrosion behaviour of Ti-6Al-4V exposed to air environment up to 800°C was studied by Zhou and Bahadur [69]. Erosion experiments were performed in a sandblast type of test rig at seven different temperatures. The specimens were heat treated by annealing and solution treating and aging. The target specimens were eroded with 120 grit silicon carbide particles at impact velocities from 55 to 110 m/s and impingement angles from 10 to 90°. The oxidation behaviour and the morphological features of the eroded surfaces were studied by scanning electron microscopy and the deformation characteristics of the oxide scales were determined by static indentation tests. It was found that the erosion rate increased with the temperature ranging from 200 to 800°C where the increase in erosion rate with temperature was fairly rapid within the range of 650 to 800°C. Oxidation was also fairly high in this temperature range and the interaction between the erosion and corrosion was quite significant.

Robinson and Reed [70] reported the effect of laser surface treatments on the water droplet erosion resistance of a commercial alloy of nominal composition Ti-6Al-4V. Use was made of a continuous wave CO_2 laser to melt the Ti-6Al-4V in both inert and dilute nitrogen atmospheres. The gas composition of the atmosphere was set

at either 100% Ar, 90 Ar + 10% N_2 or 80% Ar + 20% N_2 by volume. The successive inter-track overlap was set at either 50% or 75% of the surface width of a single melt track. The cumulative mass lost during water droplet erosion of the laser surface melted material decreased substantially relative to the untreated material for all processing conditions examined. The enhanced erosion resistance was attributed to the increases in the surface layer micro-hardness as well as the resistance of the martensitic microstructure to the hydraulic penetration mechanism of erosion. The benefits of nitrogen alloying over surface melting in an inert environment were not substantial, but this might be attributed to the pre-existing micro-cracks in the nitrogen alloyed surface layers.

The ability of the laser nitriding process to improve the water droplet erosion resistance of Ti-6Al-4V alloy was studied by Gerdes et al. [71]. Using a CO_2 continuous laser, a layer of about 400 μm thickness was nitrided and another layer of 400-500 μm was only heat affected. Electron microscopy observations showed that the microstructure of nitrided layers consisted essentially of TiN compounds which were embedded in Ti(α) matrix. Depending on the nitrogen concentrations within the feeding gas, the titanium nitrides exhibited plate-like shape or dendritic morphologies. Below the nitrided layer a thickness of 50-100 μm of samples underwent martensitic structure which in turn gives rise progressively to bimodal ($\alpha+\beta$) base material. Laser nitriding increased micro-hardness from 370-400 to 650-800 HV, and enhanced erosion resistance significantly compared with untreated Ti-6Al-4V and hardened 12% Cr stainless steel. The mechanism of material removal by erosion was changed from work hardening and platelets detachment in untreated samples to brittle fracture by formation of large flakes and spalling in nitrided layers. Advanced stages of

24

erosion were accompanied by the appearance of macro-creaks often in the nitrided zone, but some of them propagate even into the heat-affected area. The annealing at 650 and 700°C of the laser-nitrided samples resulted in the precipitation of b phase rich in vanadium.

The tribological properties of plasma nitrided hot-worked tool steel AISI H11 were examined by Yilbas et al. [72]. Different nitriding temperatures and duration were considered. To characterize the composite structures, wear tests, XRD analysis, SEM and micro-hardness tests were carried out. The nitride zone depth was measured using the nuclear reaction analysis (NRA) technique. The micro-hardness, wear properties and morphology were considerably affected by plasma nitriding. As the process temperature increased, the depth profile of the nitrided zone was increased. They also found that an increase in nitriding time and process temperature resulted in the increase in the compound layer thickness. A microphotograph of nitride zone showed that almost homogeneous precipitation occurred in the cross-sectional zone.

The surface nitridation of titanium was carried out by Kobayashi [73] at a low pressure in nitrogen atmosphere using a gas tunnel type plasma jet. The TiN film could be formed in 10 seconds (10 μm thick and 2000 HV) The TiN ratio was 91% on the surface of the TiN film and the structure was approximately homogeneous over the irradiated surface. The structure of the TiN film was analyzed using XRD and the surface of the film was measured by Vickers hardness testing machine to investigate the effects of the deposition conditions on the properties of titanium nitride films. The measured values of both the Vickers hardness and the TiN ratio were directly related to the TiN film thickness.

Cold forging of spur gears from Ti-6Al-4V material was introduced by Yilbas et al. [74]. Plasma nitriding was carried out to improve the surface properties of the resulting gears. Nuclear reaction analysis was conducted to obtain the nitrogen concentration whereas the micro-pixe technique was used to determine the elemental distribution in the matrix after the forging and nitriding processes. Scanning electron microscopy and XRD analysis were used to investigate the metallurgical properties and the formation of nitride components in the surface region. Micro-hardness and friction tests were carried out to measure the hardness depth profile and the friction coefficient at the surface. Scoring failure tests were conducted to determine the rotational speed at which the gears failed. Three distinct regions were obtained in the nitride region, and at the initial stages of the scoring tests, failure in surface roughness was observed in the vicinity of the tip of the gear tooth. This occurred at a particular rotational speed and work input.

The tribological behaviour of specimens coated by two layers, titanium nitride film as the top layer and titanium film as the under layer were studied by Guu et al. [75]. The coating layers of the bottom specimens were deposited using the cathodic arc ion plating process. Experiments were carried out on a wear test machine using a thrust-washer adapter to simulate the surface contacts between the steel ring (the upper specimen) and the titanium nitride coated washer (the bottom specimen). The influence of the thickness of the two coating layers on the tribological behaviour, wear mechanism, specimen hardness and adhesive strength were addressed. A thin titanium nitride film in combination of a thick titanium film attenuates the adhesive strength, resulting in a significant increase in the wear rate. The influence of the titanium nitride on titanium film on the friction coefficient was quite limited at higher

sliding speeds. The specimen's hardness was increased by thickening the titanium nitride layer, but it was lowered by increasing the titanium thickness. When the specimen's sliding speed was increased, both the wear rate and the friction coefficients showed significant reduction.

Guu and Lin [76] made comparison of some tribological parameters for specimens coated with titanium nitride as the top layer but using different materials as the underlayer. For the specimens coated by the cathodic arc plasma deposition method, electroless nickel films of various thicknesses were deposited as the under layer. For the specimens coated by the cathodic arc ion plating method, a titanium film with various thicknesses was deposited as the under layer. The tribological performance of the two kinds of coating specimens was compared for the following parameters: wear rate, friction coefficient, adhesive strength, and specimen's hardness. The role of the thickness of the two different coating layers, and of the material of the underlayer on the friction and wear behaviour was investigated.

The pressure-distance scaling law for pulsed laser deposition was examined by Kwok et al. [77] for several thin film systems. This scaling law was due to the plasma dynamics occurring within the laser plasma plume near the location of the substrate. Time-of-flight studies of both the ions and the neutrals confirmed the existence of an optimal velocity distribution for optimal film deposition. Fast ions played a major role in determining the quality of the films deposited. They might provide surface activation of the film or induce damage to the film depending on their kinetic energies.

Krebs et al. [78] characterized the pulsed laser deposited (PLD) metallic alloys and multilayers by the formation of amorphous or metastable nano-crystalline phases with the high solid solubilities, the unusually enlarged lattice spacing in growth direction and the intermixed interfaces. The differences between the sputtered and the evaporated samples were discussed with respect to the high instantaneous deposition rate, which was about 10^5 times greater than that for the sputtering or thermal evaporation processes. In addition, the high kinetic energy of the deposited particles of up to more than 100 eV at high laser fluxes inducing atomic mixing produced a large number of defects and a high stress in the deposited films.

Xingzhong et al. [79] investigated the wear behaviour of Ti (C, N) ceramic when cutting the austenic stainless steel AISI 321. The wear tests were carried out on a pin-on-disc tribo-meter, which could simulate frictional characteristic a real cutting process. The selected load range was 58.8 - 235.2 N; the selected speed range was 0.8 - 3.2 m/s. The test results showed that the wear of Ti(C, N) ceramic was mainly caused by adhesion between the rubbing surfaces; the wear increased with increasing load and increasing speed. When oil was used for lubrication, the friction coefficient of the sliding pairs and the wear rate of the ceramic were reduced. Scanning electron microscopy, energy-dispersive X-ray analysis and X-ray diffraction analysis were used to examine the worn surfaces.

Plasma spray coatings were evaluated by Davis et al. [80] as surface treatments for aluminum, titanium and steel substrates prior to adhesive bonding. These treatments were environmentally benign in that they involved no chromates and emit no liquid or gaseous wastes. The coatings could be engineered for specific

applications and were better suited for localized repair than chemical processes. For aluminum adherends, a polyester coating gave a performance equivalent to that of the best chemical treatment (phosphoric acid anodization) for some epoxy adhesives. With stronger, tougher adhesives, a Ti-6Al-4V coating provided improved performance to match that of phosphoric acid anodization. A Ti-6Al-4V coating on titanium substrates exhibited identical initial strength and durability to the best chemical controls under moderate temperature conditions. At high temperatures, the plasma spray coating continued to exhibit excellent durability while oxide-based treatments readily failed due to oxygen dissolution into the metal. For steel adherends, an Ni-Cr-Zn coating provided enhanced corrosion resistance and bondability even after exposure to aggressive environments or ambient conditions over long periods of time. Additionally, rubber bonds with the plasma spray coating were more tolerant to surface contamination than those with grit-blasted surfaces. These investigations indicated that the plasma spray process was more robust than conventional processes and could give equivalent or (in some cases) superior performance.

The behaviour of PVD TiN on high-speed steel (HSS) under low stress abrasion was examined by Scholl [81]. HSS bars were coated with TiN by a cathodic arc process and by a magnetron sputtering process. The samples were then tested using the dry-sand-rubber-wheel abrasive test. The phenomenon observed was multiple cracks (i.e., micro fissuring) of the surface that were long, narrow and parallel to each other. Coatings less than 1.5 μm exhibited a failure mode of continuous coating removal by micro-fissuring and subsequent fracture and loss of the TiN layer. Thicker coatings over 1.5 μm thick also failed only at free edges where a macro-particle had been removed. The results indicated that as long as coating

integrity was maintained under the flow of abrasive material, the wear rate of the TiN was small.

Molinari et al. [82] demonstrated that plasma nitriding had a positive effect on the dry sliding behaviour of Ti-6Al-4V alloy based on the treatment temperature. They carried out dry sliding tests under different load and sliding speed conditions at three temperatures; 973, 1073 and 1137°K. The wear mechanisms was studied by interpreting the results on the basis of the evolution of the friction coefficient and by characterizing the wear debris and worn surfaces. The wear mechanisms were found to be dependent on the nitriding percentage and nitriding temperature. When the wear was determined by the resistance of the compound layer (low loads and low sliding speeds), the nitriding treatment had to be carried out at 1073°K to obtain the proper compromise between the thickness of the compound layer and the hardness of the diffusion layer. When the material was exposed to delamination (high loads and high sliding speeds), the compound layer tended to be destroyed rapidly. Under these conditions, the strength of the diffusion layer had to be maximized by heating to higher temperatures, e.g. 1137°K in order to enhance the hardness of the diffusion layer.

Novak and Komac [83] studied the wear mechanisms of TiN (physically vapour deposited) coated TiC-based cermets. The insert samples were characterized in terms of mechanical properties and their tool life during machining of steel. Static diffusion experiments were conducted to simulate the diffusion process across the tool-workpiece interface at high temperature and pressure. The depth profiles of the worn edges in both uncoated and TiN-coated cermets were analyzed and tested by

machining of steel. To identify the dominant wear mechanisms, the worn cutting tools and the diffusion couples were analyzed by scanning electron microscopy, energy-dispersive spectroscopy and Auger electron spectroscopy. The results of cutting tests with the inserts confirmed the beneficial effect of TiN coating on the cutting tool life of cermet leading to the effective suppression of carbide or carbonitride grain decomposition in the cermet surface layers.

Khedkar et al. [84] investigated the influence of structural, as well as operational, parameters on the sliding wear and friction behaviour of plasma sprayed and subsequently laser alloyed coatings under dry and marginally lubricated conditions. A pin-on-disc apparatus was used to characterize the adhesive and abrasive wear resistance of two different steels, plasma sprayed and laser alloyed with WC-Co, Mo, and Cr. They reported that the plasma-coated Mo was relatively soft and was prone to failure. The lower coefficient of friction associated with Mo coatings was attributed to the dominant role played by the thick, adherent oxide film at the interface. The lower bond strength and the stress gradient associated with the plasma sprayed coatings made them susceptible to fail along the interface, but the laser alloying caused improvement.

The dry sliding behaviour of the Ti-6Al-4V alloy was studied by Molinari et al. [85] to determine the responsible mechanisms for the poor wear resistance in different load and sliding speed conditions. They also confirmed the low resistance to plastic deformation of the alloy even at low loads and the poor protection provided by the surface oxide. The maximum wear resistance was found at a decreasing sliding speed as the load was increased, where a transition from oxidative wear to

delamination occurs. This point was found at a decreasing speed as the load was increased. It was concluded that an increase in the mechanical properties of the surface was necessary to avoid plastic deformation and to retard thermal softening which promote delamination and cause mechanical instability of the surface. At the lower sliding speeds, the chemical characteristics of the surface have to be modified to avoid the formation of the scarcely protective oxide.

De Sousa and Alves [86] studied AISI 304 stainless steel workpieces with cylindrical blind holes plasma nitrided in an atmosphere of H_2-$20N_2$ at 1000 Pa, 773°K, for 2 hours. The influence of the hole dimensions on the temperature uniformity was investigated. The maximum temperature difference was found to be 45°C between the surface and the bottom of the cylindrical holes for a hole 10 mm in diameter and 17 mm deep. This could be attributed to the effect of the ratio between the surface area and the volume at different points in the samples. The effect of overheating was observed at working pressure of 1000 Pa.

Novak et al. [87] discussed the results of a study to understand wear mechanisms of a TiN (PVD) coated Ti(C,N)-based cermets. Static diffusion experiments were carried out in order to simulate the diffusion process across the tool-work piece interface at high temperature and pressure, thus permitting the wear to be determined. Experimentally, coated and uncoated tool materials were tested in machining CK45 steel under different cutting conditions. It was confirmed that the coating can increase the tool life of cermets significantly. The diffusion couples and the worn cutting tools were analyzed by SEM, EDS, and AES in order to identify the dominant wear mechanisms. A TiN coating containing a high concentration of defects

32

is not as efficient a diffusion barrier as one would expect. The association of defects into micropores can cause enhanced diffusion not only of carbon and nitrogen, but also of metals through the apparently dense TiN layer.

Franco et al. [88] studied the microstructure and the electrochemical behaviour of coated AISI 4340 steel substrates. Titanium, reactive titanium nitride (TiN) and TiN film, obtained from a titanium film nitrided at 900°C, and were deposited on steel substrates by magnetron sputtering. Also, a solid titanium sample was nitrided at 900°C. The potentiodynamic polarization technique was used to evaluate the samples processed in a solution of 3% NaCl, for the corrosion resistance. In addition, the samples were examined by SEM to determine the quality of the coated surface. They found that from the potentiodynamic analysis the reactive TiN coatings and nitrided titanium films were characterized by low porosity and pinhole concentration. However, the low corrosion resistance of reactive TiN films indicated that the metal substrate was not entirely coated, leaving large and deep pinholes. As a consequence of the presence of microstructural defects such as surface roughness and porosity, the reactive TiN coatings were more prone to corrosion attack than plasma-nitrided Ti coatings (TiN). While plasma-nitrided Ti coatings showed intragranular, the reactive Ti coatings showed intergranular corrosion. Galvanic corrosion between the coating and substrate resulted in significant attack of the metal, allowed by the penetration of small pinpoints into the substrate.

1.3. SCOPE OF THE PRESENT WORK

The present study was conducted to determine the surface properties of TiN coated, plasma nitrided and plasma nitrided/laser melted Ti-6Al-4V samples. A TiN coating and plasma nitriding units were used to nitride the workpieces while a CO_2 laser was used to coat and irradiate the nitrided surfaces. X-ray diffraction (XRD) was utilized to determine the nitride compounds at the surface and in the nitride zone before and after the laser melting process. The wear properties and friction coefficient of untreated, TiN coated, plasma-nitrided and nitrided/laser-melted surfaces were investigated through pin-on-disc experiments. The microstructure of the nitrided and laser melted zones was studied using a scanning electron microscopy (SEM) technique. The micro-hardness tests were conducted across the melted and unaffected regions. A mathematical model governing the laser heating process was developed using a Fourier theory and the heating and cooling rates were predicted. To achieve this goal, the step input intensity of the laser pulse with and without convection boundary conditions were considered.

CHAPTER - 2

Equipment and Procedure

2.1 Introduction

In this chapter, experimental apparatus for TiN coating, plasma nitriding, laser treatment and wear test of the Ti-6Al-4V samples are introduced. The topics will be presented under the relevant sub-headings.

2.2 PVD TiN Coating

There are two major coating processes: Physical Vapor Deposition (PVD) and Chemical Vapor Deposition (CVD). These techniques allow effective control of coating composition, thickness and porosity. Three basic types of PVD processes are available. These include vacuum or arc evaporation, sputtering, and ion plating. These processes are, in general, carried out in a high vacuum at temperatures in the range of

200 - 500°C. In physical vapor deposition, the particles to be deposited are carried physically to the workpiece [89-91].

In vacuum evaporation, the metal to be deposited is evaporated at high temperatures in a vacuum and is deposited on the substrate, which is usually at room temperature or slightly higher. Uniform coatings can be obtained on complex shapes. In arc evaporation, on the other hand, the coating material i.e., cathode is evaporated by a number of arc evaporators, using highly localized electric arcs, which produce highly reactive plasma consisting of ionized vapor of the coating material. The vapor condenses on the substrate i.e., anode and coats it. Applications for this process may be functional or decorative.

In sputtering, an electric field ionizes an inert gas usually argon. The positive ions bombard the coating material (cathode) and cause sputtering (ejecting) of its atoms. These atoms then strike and condense on the workpiece, which is heated to improve bonding. In reactive sputtering, the inert gas is replaced by a reactive gas, such as oxygen, in which case the atoms are oxidized and the oxides are deposited.

The last type is ion plating which is a generic term describing the combined process of sputtering and vacuum evaporation. An electric field causes a glow discharge, generating plasma. The vaporized atoms in this process are only partially ionized.

The production of thin layers of TiN on Ti-6Al-4V substrate surfaces was carried out using the following method: Ti-6Al-4V samples were ground, polished, ultrasonically cleaned in chemical solvents and put into a PVD unit. A titanium film

was sputter deposited onto the substrate at 260°C by a d.c. magnetron source in an argon atmosphere. It was then implanted with N^+ ions at an acceleration potential of 50 keV. Vacuum annealing was carried out at 540°C, after the implantation process, for one hour. A series of nominal constant thickness single layer of 400 nm film was formed. Consequently, after a series of trials the total thickness of the multi-layer film in the range 2–4 μm was obtained. The lattice parameters of the coat interface varied between 4.22 Å and 4.275 Å. In the lattice, aluminium atoms have substituted some titanium atoms, which decreases the lattice parameter. After examining SEM results, it appears that the coverage area of defects is less than 1% of the surface.

2.3 Plasma Nitriding

Workpieces were placed in the nitriding unit as shown in figure (2.1), which operated within the d.c. bias voltage range 400-700 V. The plasma nitriding unit used in this study, consists of power supply, a computer control unit, a gas mixing device and a stainless steel vacuum chamber as shown in figure (2.2). Prior to the nitriding process, the samples were cleaned by surface sputtering in argon and hydrogen (3/1 ratio) plasma for 45 minutes. The nitriding was performed in an N_2/H_2 (8/2 ratio) plasma with the total volume flow rate varied between 40 and 120 cm^3/s. The temperature of the samples during nitriding was varied in the range 450 - 520°C. A plasma nitriding cycle was carried out by evacuation of the chamber and then followed by initialization of the glow and the introduction of the treatment gas heating up to the treatment temperature. Heating occurs as the colloiding particles give up

their energy to the metallic surface. Only the plasma provides the heat and no external heating source is required. In addition, the amount of heating is proportional to the current density. The nitriding process conditions are given in Table-2.1.

Temperature Range (°C)	450 – 520
Time (ks)	54 – 72
d.c. Voltage (V)	400 – 700
Total Pressure (kPa)	0.46 - 0.51
Total Volume flow rate (cm^3/s)	40 - 120

Table-2.1   Nitriding Process Conditions
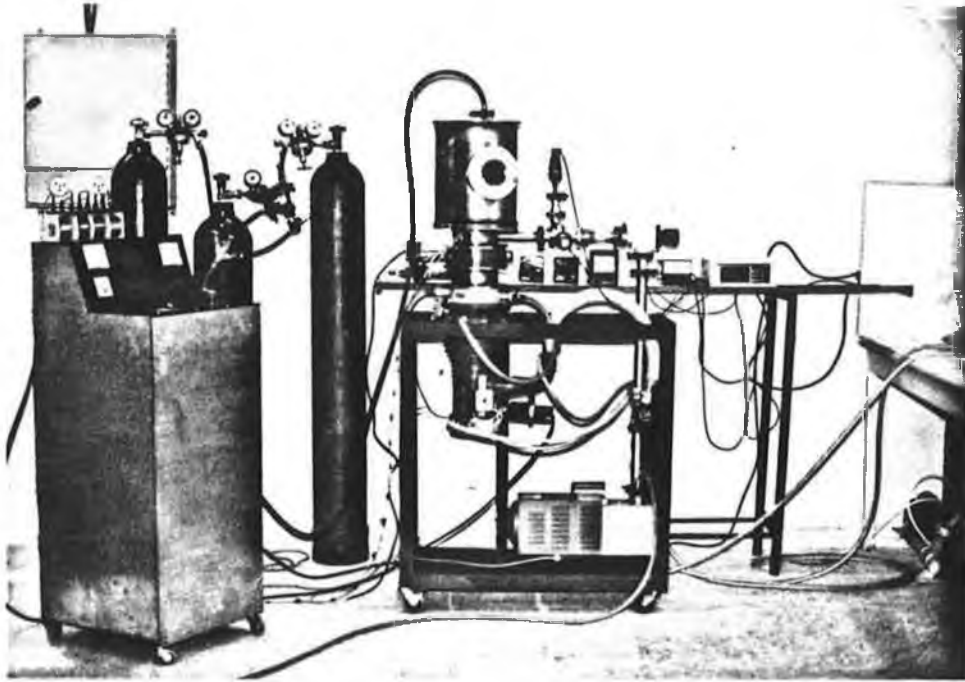
Figure-2.1   Photograph of Plasma Nitriding Unit
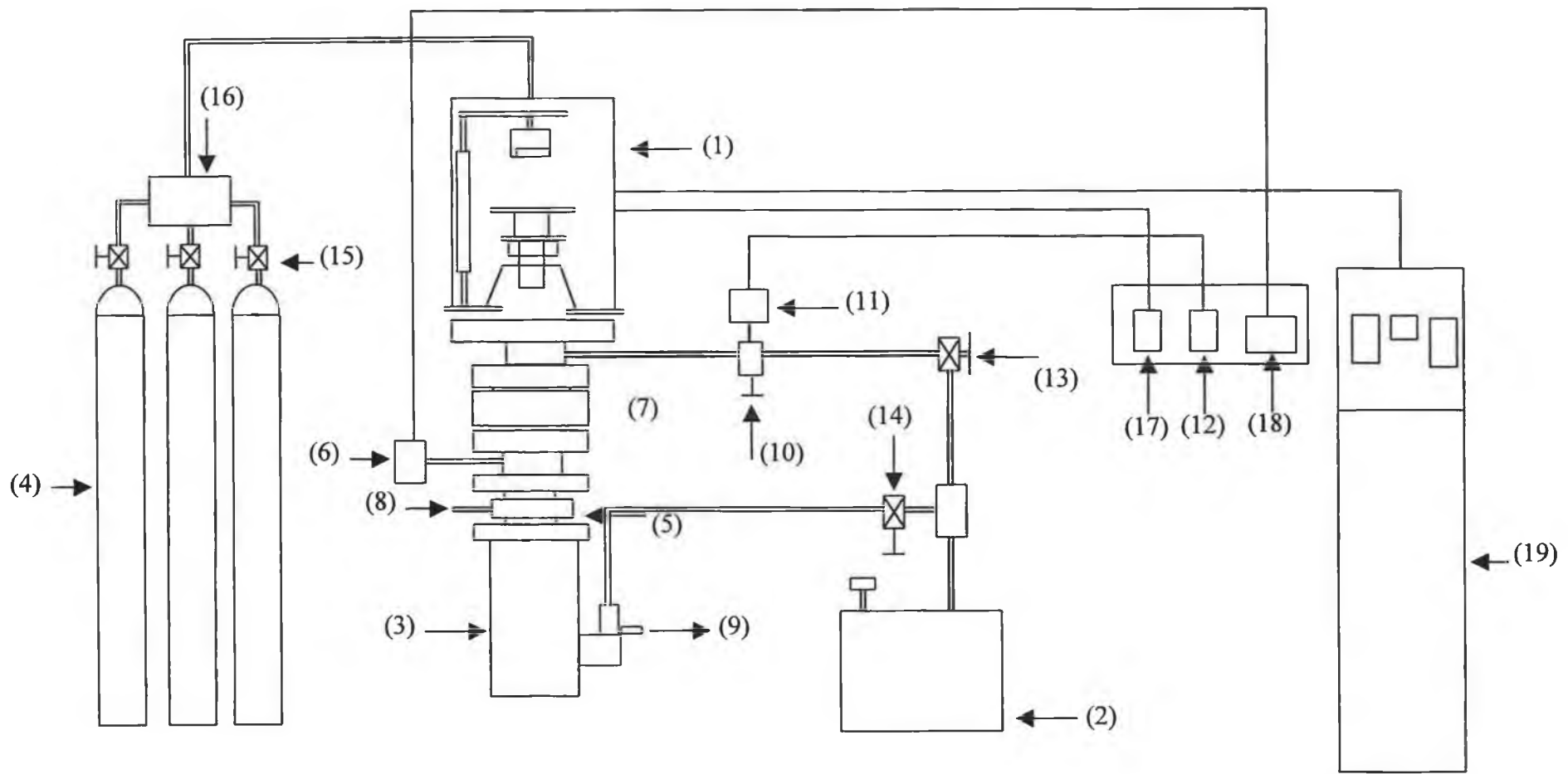
Figure-2.2   Schematic View of Plasma Nitriding Unit

(1) Vacuum chamber, (2) Rotary vacuum pump, (3) VHS-4 diffusion pump, (4) Gas cylinders (N_2, Ar, O_2), (5) Baffle, (6) Cold cathode gauge, (7) Valve, (8) Cooling water inlet, (9) Cooling water outlet, (10) Air discharge valve, (11,12) Pirani gauge, (13,14) Two-way valve , (15) Niddle valve, (16) Mixture, (17) Temperature sensor, (18) Multi-gauge controller, (19) Power supply.

2.4 Workpiece Material (Ti-6Al-4V alloy)

The Ti-6Al-4V alloy contains α and β structures; 6% aluminum and 4% vanadium, stabilizing the alpha and beta phases respectively. The elemental weight percentages of the Ti-6Al-4V alloy are given in Table-2.2.

Element	Ti	Al	V	Cu	Cr	Fe	O
Amount (wt. %)	Bal.	6	4	0.03	0.01	0.32	0.20

Table-2.2   Chemical Composition of Ti-6Al-4V Alloy (% wt)

The original microstructure was α and intergranular β resulting from mill annealing as shown in figure (2.3). The workpieces were cut into a rectangular shape, with dimensions of 30 mm x 150 mm x 5 mm, to obtain the cross sections. They were later ground and polished with 0.25 µm diamond suspension, then degreased ultrasonically in acetone and dried in air before being treated. The peak-to-valley surface roughness was measured as 0.7 µm workpieces.
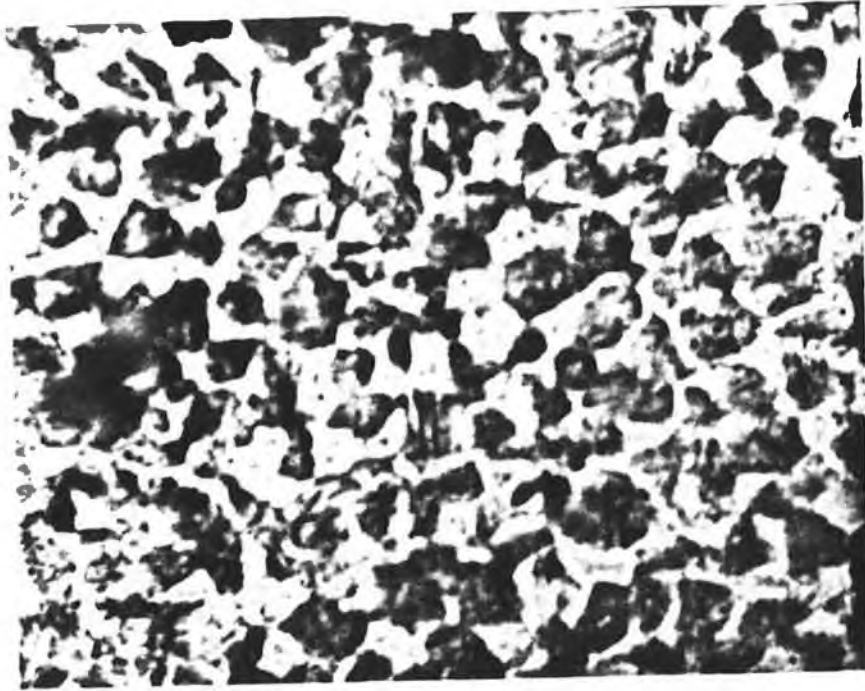
Figure-2.3   The Base Material Microstructure

2.5 Material Characterization

The specimens were prepared for the scanning electron microstructural investigation by appropriate sectioning, mounting and mechanical polishing on grinding papers. Etchants used to reveal the features of the treated regions were: -

$$[3 \text{ ml HF} + 6 \text{ ml HNO}_3 + \text{water}] \text{ or}$$

$$[20 \text{ ml HF} + 20 \text{ ml HNO}_3 + 40 \text{ ml Glycerol}]$$

The polished and etched microstructures were studied and recorded using optical microscopy and SEM for higher magnification. A sputtered layer of gold film was needed to prevent charging of the sample surface during the SEM photography, and to increase the contrast for higher resolutions.

2.5.1 SEM and EDS

The purposes of these techniques are: (1) to provide high resolution and high magnification (up to 180,000X) images of solid samples to show surface structure by SEM microphotography and optical microscopy, to investigate the metallographic changes in the nitride and nitride/melted regions and (2) to give quantitative and qualitative elemental analyses of the microscopic regions imaged, using the energy dispersive spectrometer (EDS) to obtain the elemental distribution in respective regions [92,93].

2.5.1.a   Scanning Electron Microscopy

The scanning electron microscope may be regarded as a more powerful version of the conventional optical microscope enabling the study of very small objects. The optical microscope uses a beam of photons for imaging and has a maximum magnification of ~1,000x, together with a point to point resolution of ~200 nm. In comparison, the SEM uses a beam of electrons for imaging and has a maximum magnification of ~200,000x, together with a resolution of ~6 nm. The SEM not only permits observation of very fine details, e.g., high resolution, but also exhibits good focus over a wide range of specimen surfaces, i.e., large depth of field.

The SEM consists of five main components. These are: (1) electron gun, fitted into the column, produces a large and high intensity electron beam; (2) column controls that shapes the beam into a size useable for scanning microscopy; (3) scanning system scans the beam over the sample in a television type raster. The beam scanning over the sample releases electrons from it; (4) electron collector and display collects these electrons and converts them to an image, which can be viewed by the operator and (5) control electronics contains all circuits necessary to control the performance of SEM.

The principle of operation of the microscope is as follows. Electrons are emitted from a heated filament and are then accelerated through the column by applying a potential of -25 kV. The electron beam is de-magnified in the condenser lens and then focused onto the sample by the objective lens. The surface of the

specimen is then scanned by the finely focussed electron beam, and the chosen signal output is displayed on a cathode ray tube (CRT), which is scanned synchronously with the electron probe. The interaction of the electron beam with the sample produces a large number of emitted signals. The signal most frequently used for imaging purposes is that of secondary electrons. These are low energy electrons which have been absorbed by the sample and subsequently ejected for collection by a positively biased detector, which consists of a scintillator / light pipe / photomultilier tube assembly. The amplified signal is then used to modulate the brightness of the viewing CRT. The emitted flux of secondary electrons is dependent upon the surface topography and thus a recognizable image of the sample is formed. The magnification factor is simply the ratio between the area of the sample scanned by the incident electron beam and the fixed viewing area. Thus increased magnification is achieved by simply decreasing the area of the specimen that is scanned.

2.5.1.b   Energy Dispersive Spectrometer

Qualitative and quantitative information can be obtained from the sample by monitoring emitted X-rays. The incident electrons induce characteristic X-ray emission from different elements in the sample. These X-rays may be analyzed either by their wavelength or by their energy. Both approaches have their merits and drawbacks and they are usually seen as complementary. For rapid qualitative and semi-quantitative analysis, however, energy dispersive systems utilizing sophisticated computer analysis routines are preferred. This type of spectrometer is currently being

operated with the SEM for elemental analysis or, alternatively, to show the distribution of a particular element within the scanned area. The presence of the beryllium window means those elements lighter than sodium can not be detected.

The electron probe micro-analyzer uses the characteristic peaks of the X-ray spectrum resulting from the bombardment of the specimen by the beam of electrons. The wavelengths and intensities of these peaks can yield valuable information about the chemical composition of the specimen. An electron probe micro-analyzer is thus basically a SEM equipped with X-ray detectors. Two basic types of detectors are used. In the energy-dispersive X-ray spectrometer, a solid-state detector develops a histogram showing the relative frequency of the X-ray photons as a function of their energy. The wavelength-dispersive spectrometer uses X-ray diffraction to separate the X-ray radiation into its component wavelengths.

2.5.2   X-ray Diffraction Analysis

The X-ray diffractometer (XRD) is a device, which measures the intensity of the X-ray reflections from a crystal employing an electronic device such as a Geiger countertube or an ionization chamber instead of a photographic film. The apparatus is so arranged that both the crystal and the intensity measuring device (Geiger countertube) rotate. The countertube, however, always moves at twice the speed of the specimen, which keeps the intensity-recording device at the proper angle during the rotation of the crystal, so that it can pick up each Bragg reflection as it occurs. In a

modern instrument of this type, the intensity-measuring device is connected through a suitable amplification system to a chart recorder, where the intensity of the reflection is recorded on a chart by a pen. In this manner, one obtains an accurate plot of intensity against Bragg angles. As the X-ray diffractometer is capable of measuring the intensity of Bragg reflections with greater accuracy, both qualitative and quantitative chemical analyses can be made by this method [94].

The analysis of different phases present in the nitrided samples for their structural information was performed by XRD. The vertical placement of the device in a radiation protecting housing is controlled by computer and is thus capable of fully automatic operation. A molybdenium tube, emitting Mo k-alpha radiation provided the X-ray source. To suppress the k-beta reflections, a zirconia filter was used. The selection of the X-ray tube and, hence, the penetration depth of the X-ray produces many lines in the low angle range with high intensity. An XRD trace was obtained between the 2 theta angles 14 and 44 degree, using in step scans mode with step-width at a counting time of 15 seconds.

After the nitriding process, the layers were analyzed by XRD using CuK_α and MoK_α radiations. XRD profiling of the treated cases were performed by periodic removal of the surface by grinding with SiC abrasive papers. The lattice parameters of the unit cell were calculated from the diffraction data obtained with CuK_α radiation. The error in determination of the lattice parameters was found to be ±0.6 Å. An XRD was carried out to analyze the nitride species in the melted and untreated regions.

2.6 CO_2 Laser Melting

Laser machining belongs to the large family of material removing or machining processes. It provides a feasible production method for hard-to-machine materials and involves special applications such as micro-machining. However it does have limitations in some applications in terms of material removal rate and surface quality, when compared with traditional machining methods. Nevertheless, interest is growing in the use of lasers in welding, soldering, surface modification, marking, cutting, hole drilling and scribing.

The dominant lasers used in material processing are CO_2, Nd-YAG and Nd-Glass lasers, with CO_2 lasers accounting for the largest percentage of sales. In this section, a CO_2 laser and its output characteristic are described.

CO_2 lasers come in a variety of power range, sizes and designs. All use the molecular vibration of CO_2 as a "lasing" mechanism. Generally, a mixture of CO_2, nitrogen and helium are employed, the nitrogen is active in the excitation process and helium acts as an internal heat sink. Sometimes a small amount of oxygen is added to reduce contamination from CO and carbon. CO_2 lasers emit radiation at 10.6 µm wavelength, which is quite far into the infrared region. This causes problems with respect to the reflectance in processing metals such as copper, silver and gold, but, alternatively, these metals can be used as mirror materials internally or externally. Some small sealed-off CO_2 lasers, such as the waveguide types, use RF excitation, but most use DC electrical discharge excitation. The three major designs used in industrial processing applications are the slow axial gas flow with axial discharge, the

fast axial gas flow with axial discharge and the fast transverse gas flow with transverse discharge. The slow flow design relies on thermal conduction for cooling of the gases and, consequently, the cross section area of the discharge region is limited. Roughly 50 to 70 watts of power per meter tube length can be obtained from this type of design. Beam quality is generally good, with near Gaussian output being attainable because of the long narrow bore tube. The fast designs use convection cooling, so that much larger discharge cross sections can be achieved. Hence, the power per unit length is much higher, 600 watts per meter for fast axial flow and 2,500 watts per meter for transverse fast flow. In fast transverse flow designs the beam is folded back and forth through the discharge region several times. Unstable resonator configurations are frequently employed for multi kilowatt CO_2 lasers to eliminate transmissive optics. The efficiency of these CO_2 lasers is approximately 10% (total input power divided into useful output power). This is about three times the efficiency of the other two industrial lasers (i.e., Nd-YAG and Nd-Glass lasers) [95,96].

The production of a uniform hardened layer can be achieved by scanning the laser beam over an area. An overlapping array of tracks made by such means produces a uniform depth of modified surface. During this procedure, short-cycle re-melting and aging of adjacent tracks occurs. Re-melting or thermal cycling of one point may occur several times, depending upon the degree of overlap.

In surface melting, the laser is successfully used to successively melt a controlled area of the surface. The solidification occurs during the cooling cycle of the process resulting in metallurgical properties different to conventionally cooled

surfaces. This may provide high strength and high ductility together with good corrosion and wear properties of the substance [97,98]. Some of the alloys on surface melting can not result in the optimum effect, although grain refinement is always likely. The laser surface nitriding, particle injection, cladding and surface alloying have also been introduced to improve the tribological properties of the surface [3,33,99].

In general, there are two main factors, determining the structure resulting from a laser melting process, there are: the composition of the melt, and the solidification parameters. The parameters, which either directly or indirectly affect the structure, are the power of the laser beam, the distance between focal points and the surface, and the traverse speed. For any comparison between results from different sources, the important parameters are the power density and the interaction or dwell time.

A CO_2 laser delivering a maximum output power of 1.6 kW at the TEM_{00} mode was used to melt the workpiece surface as depicted in figure (2.4). The laser output power intensity attained was of the order of 10^{12} W/m^2 with a nominal spot radius of 0.2 mm. The focus diameter of the laser beam at the workpiece surface was, however, altered by varying the focus setting of the focusing lens. A nozzle was designed to introduce the shielding gas and to keep the gas pressure constant during the melting process. Nitrogen was used as shielding gas in the melting environment. The experiment was repeated for different shielding gas pressure levels. In order to achieve low and high melting regions, the laser output power intensity was varied. It should be noted that high melting corresponds to the melting occurring at a temperature in between melting and evaporation temperatures, while low melting

50

corresponds to the melting occurring at melting temperature of the substrate. The laser output power and shielding gas pressure parameters are given in Table-2.3. Three levels of power intensity were used in the melting process to obtain the low and high melting regions.

Laser Output Power (kW)	Assisting Gas Pressure (kPa)	Table Speed (m/min.)
1.20	110	0.60
1.40	125	0.80
1.60	140	0.90

Table-2.3   Laser Parameters for Surface Melting Process
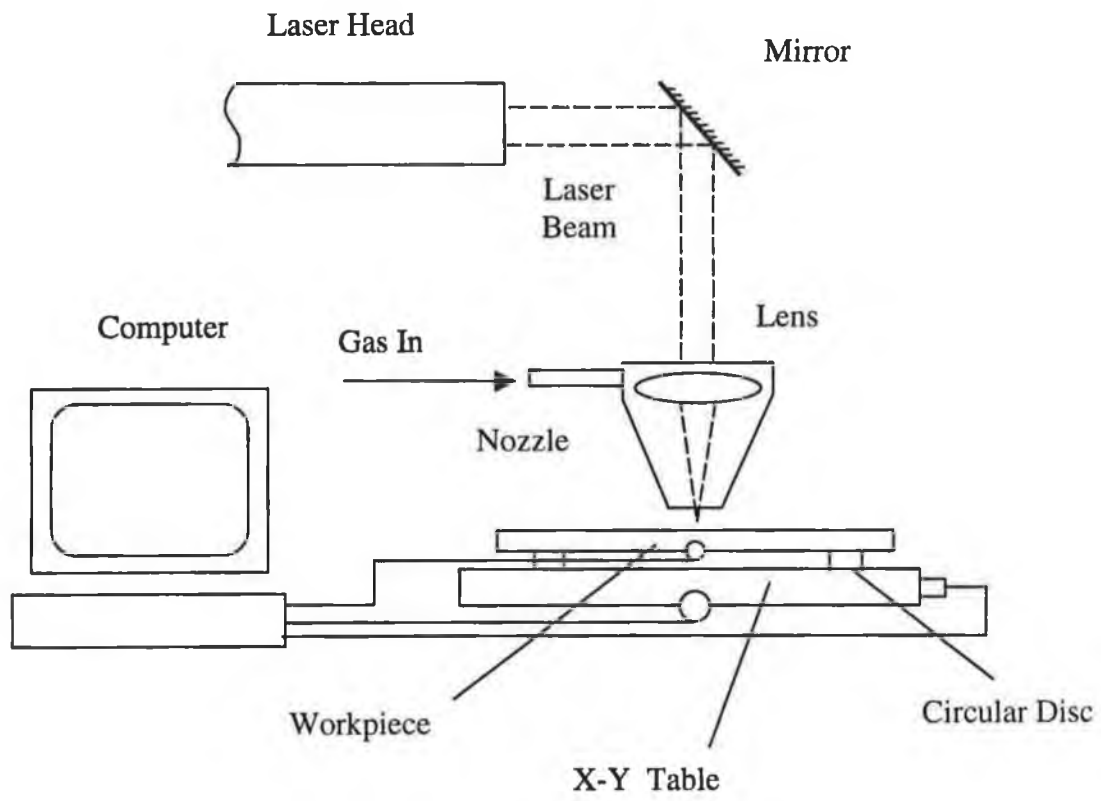
Figure-2.4   Experimental Set-Up

2.7 Wear Testing

Wear may be defined as the progressive loss of substance from the operating surface of a body, occurring as a result of relative motion of the surface with respect to another body. The concept embraces metal to metal, metal to other solids and metal to fluid contact. Traditionally, wear has been described in terms of adhesion and abrasion [100,101]. The former occurs when two bodies slide over each other and the surface forces cause the transfer of fragments of material. The latter occurs when particles or protuberances cut fragments from a contacting softer surface in relative motion. While abrasion and adhesion are regarded as the predominant wear processes, it has become apparent that practically every material damage mechanism can contribute to wear. Consequently, almost every physical, mechanical and chemical characteristic of a material is liable to affect its wear performance [102-105].

Wear tests of untreated, plasma-nitrided, and laser-melted samples were carried out using a pin-on-disc wear tester, with a hard ball 3 mm diameter equipment with ET025 oil as lubricant. The rotational speed of the disc was 35 rpm, giving two levels for the linear relative speed (pin relative to the disc). These include $V_1=25$ mm/s for a wear track with a diameter of 13.6 mm and $V_2=30$ mm/s for a wear track of 16.37 mm diameter. The scars developed during the wear operation were examined using SEM. The friction coefficient was measured using a ball-on-disc machine for all tests. The ball material was hardened AISI 52100 steel, which was allowed to slide dry on the rotating sample at 100 rpm (corresponding to 120 mm/s) under a range of load 1 to 100 N. The friction force was measured during sliding as a function of time.

At the time of break-through, the friction increased drastically and showed critical behavior thereafter, indicating scuffing-like wear characteristics.

2.8 Hardness Tests

One of the most common tests for assessing the mechanical properties of material is the hardness test. Hardness of a material is generally defined as its resistance to permanent indentation or a measure of a material's resistance to localized plastic deformation. The depth or size of the resulting indentation is measured, which in turn is related to a hardness number: the softer the material, the larger and deeper the indentation and the lower the hardness index number. Less commonly, hardness may also be defined as resistance to scratching or to wear. Various techniques have been developed to measure the hardness of material using different indenter materials and geometries. As resistance to indentation depends on the shape of the indenter and the load applied, hardness is not a fundamental property. Measured hardnesses are only relative (rather than absolute) and care should be exercised when comparing values determined by different techniques. Among the most common standardized hardness tests are the Brinell, Rockwell, Vickers, Knoop and Scleroscope tests [89,93,106].

For each test, a very small diamond indenter having pyramidal geometry is forced into the surface of the specimen. The resulting impression is observed under a microscope and measured. This measurement is then converted into a hardness number. Careful specimen surface preparation (grinding and polishing) may be

necessary to ensure a well-defined indentation that may be accurately measured. The Vickers test is suitable for testing materials with a wide range of hardness, including very hard steels.

Hardness tests are performed more frequently than any other mechanical test for several reasons. These include (1) simple and inexpensive-ordinarily no special specimen preparation is needed; (2) nondestructive-the specimen is neither fractured nor excessively deformed, small indentation is the only deformation and (3) other mechanical properties often may be estimated from hardness data, such as tensile strength.

In this study, the micro-hardness of the workpiece cross-section was measured using the Vickers tester. It uses a pyramid-shaped diamond indenter with loads ranging from 100 to 500 gm. The Vickers hardness number is designated by HV and referred to as micro-hardness testing method on the basis of load and indenter size. The micro-hardness measurements were, therefore, carried out across the workpiece cross-sections before and after the nitriding process.

CHAPTER- 3

Heat Transfer Modelling

3.1 Introduction

Lasers are widely used as a tool to modify the surface of engineering materials. This is due to a rapid precision heating process and the attainment of high heating and cooling rates. Through laser surface melting process, fine-grained, homogeneous microstructures can be obtained which exhibit a high degree of metastability [107]. Subsequent consolidation and heat treatment promotes the precipitation of extremely fine second phase particles which provide increased room temperature strength and more importantly significant improvements in elevated temperature strength and creep resistance [31]. The laser heating process is governed by an absorption mechanism, which takes place through photon interaction with the bound and free electrons in the material structure. These electrons are then raised to a higher energy level [108]. The re-distribution of energy takes place through various collision processes involving electrons, lattice phonons, ionized impurities and defect structures. The average free collision time is in the order of 10^{-12} to 10^{-14} seconds [109]. The absorbing electrons have, therefore, sufficient time to undergo many

collisions at the period of laser machining pulses ($\sim 10^{-6}$ s) and Q-switched pulses ($\sim 10^{-9}$ s) take place. This leads to the two assumptions to be considered. The laser energy is instantaneously converted to heat at the point at which absorption takes place. The other assumption of local equilibrium and the validity of the concept of local temperature follow, thereby allowing a conventional heat transfer analysis to be made.

The basic idea of laser heat-treating is to harden the surface of materials. The laser irradiates the surface and cause very rapid heating of a thin layer of material near the surface. When the laser beam is moved to a different area on the surface, the heat gained by the thin layer will be quickly conducted away and the heated area will cool rapidly. This can be regarded as quenching of the surface region. This yields an increase in hardness of the surface layer [45]. Lasers are not efficient for heating large volumes of substances, but they can rapidly rise the temperature of the localized area.

Two regimes are of interest in laser machining of materials, which correspond to low, and high intensity irradiation. The terms low and high are relative and apply when the machining processes are conduction-limited and non-conduction limited cases, respectively [108]. In low intensity irradiation, the heating mechanism takes place in the solid phase of the material. Consequently, the phase change is avoided and the process is limited with a small depth of operation. Thus, a few microns of hardening depth may result. In general, laser heat treatment of material surfaces is a conduction-limited process. However, in the case of high intensity irradiation, material removal rates due to evaporation are considered. Consequently, the phase change is considered including melting and heating occurs which in turn results in

57

considerable depth of hardening. Thus, the heat-affected zone can extend for a few hundreds of microns.

On the other hand, the heat transfer mechanism governing the laser heating is highly important. Laser processing is of commercial interest because of its ability to accurately change the properties of a very localized surface region without affecting the material as a whole. It is, however, this scale of the operation that makes accurate predictions of the in-situ process variables so difficult. It is, consequently, the change of the microstructures and the mechanical as well as chemical properties of the treating subsurface. Therefore, modelling the physical process that can yield much insight into the phenomena occurring within the region activated by the high-power laser beam is useful. It should be noted that modelling could reduce substantially the time required for process optimization, scale-up, and control [114].

3.2 Mathematical Analysis

Heat transfer mechanism initiating the laser heating process may be outlined as follow:

The energy supplied to a material in laser heating arrives in the form of photons. Photon-electron interactions taking place results in a local increase in the electron temperature. This is an absorption process, which takes place over a very short time period [110] and is described by the Beer-Lambert's law [111]:

$$I = I_0 \exp(-\delta x) \qquad (3.1)$$

After this initial absorption process, the free electron gas in the metal proceeds to import its excess energy, through electron-molecule (phonon) collision process, to the bulk of the material [112]. Where I_0 is the peak intensity of incident irradiance and the absorption coefficient 'δ' is, in general, a function of both wavelength and temperature [109] and the negative sign indicates the reduction in beam irradiance due to absorption as a 'δ' is a positive quantity. The absorption of an incident laser beam energy results in an increase of the internal energy of the substance, which in turn initiates the conduction heat transfer [113]

The heat transfer mechanism governing the laser heating process is taken from the previous studies [108-113] and will be given under the following subheadings:-

3.2.1 Step Input Intensity Laser Pulse without Convection Boundary Conditions:

3.2.1.a. Conduction-Limited Heating

The Fourier heat conduction equation appropriate to conduction limited laser heating can be written as [108,114]:

$$k\left(\frac{\partial^2 T}{\partial x^2}\right) + A_b I_0 \,\delta \exp(-\delta x) = \rho \, C_p \, \frac{\partial T}{\partial t} \qquad (3.2)$$

For most of the engineering materials, the absorption factor 'A$_b$' is almost unity for the Nd:YAG laser wavelength [115], therefore, equation (3.2) reduces to:

$$\frac{\partial^2 T}{\partial x^2} + \frac{I_0 \delta \exp(-\delta x)}{k} = \frac{1}{\alpha}\frac{\partial T}{\partial t}$$

(3.3)

where $\alpha = \dfrac{k}{\rho\, C_p}$

with the initial and the boundary conditions:

$$\left.\frac{\partial T}{\partial x}\right|_{x=0} = 0 \quad , T(\infty, t) = 0 \ \text{and} \ T(x,0) = 0$$

The solution of equation (3.3) becomes visible in the Laplace domain, i.e., applying a Laplace transformation to equation (3.3) and the boundary conditions, with respect to 't' and introducing the Laplace transform variable 'p' yields the solution. The mathematical arrangements of this transformation may be started by the governing equation: -

$$\frac{\partial^2 \overline{T}}{\partial x^2} - \frac{1}{\alpha}\left[p\overline{T} - T(x,0)\right] = -\frac{I_0 \delta \exp(-\delta x)}{kp}$$

(3.4)

$$T(x,0) = 0$$

(3.5)

$$\left. \frac{d\overline{T}}{dx} \right|_{x=0} = 0 \quad \text{and} \quad \overline{T}(\infty, p) = 0 \qquad (3.6)$$

where $\quad \overline{T} = T(x, p)$

Substitution of the initial condition (3.5) into equation (3.4) and setting $q^2 = \dfrac{p}{\alpha}$ into

the transformed equation, it yields:

$$\frac{d^2\overline{T}}{dx^2} - q^2\,\overline{T} = -\frac{I_0\delta\exp(-\delta x)}{kp} \qquad (3.7)$$

which has a solution:

$$\overline{T} = A\,\exp(qx) + B\,\exp(-qx) + \frac{I_0\alpha\delta\exp(-\delta x)}{kp(p - \alpha\delta^2)} \qquad (3.8)$$

where 'A' and 'B' are constants and can be obtained using the boundary conditions.

Therefore, substituting of the boundary conditions $\left. \dfrac{d\overline{T}}{dx} \right|_{x=0} = 0$ into equation (3.8)

gives:

$$A = B + \frac{I_0\alpha\delta^2}{p\,k\,q\left(p - \alpha\delta^2\right)}$$

and boundary condition $T(\infty, p) = 0$ gives:

$$A = 0$$

and

$$B = \frac{-I_0 \, \delta^2}{k \, p \, q \, (q^2 - \delta^2)}$$

Therefore, the transformed equation has a solution:

$$\overline{T} = \frac{I_0 \alpha \delta \exp(-\delta x)}{kp(p - \alpha \delta^2)} - \frac{I_0 \delta^2 \exp(-qx)}{kpq(q^2 - \delta^2)}$$

or

$$\overline{T} = \frac{I_0 \alpha \delta \exp(-\delta x)}{kp(p - \alpha \delta^2)} - \frac{I_0 \delta \exp(-qx)}{2kpq}\left[\frac{1}{q - \delta} - \frac{1}{q + \delta}\right] \qquad (3.9)$$

Performing an inverse Laplace transformation to equation (3.9) yields [108]:

$$T(x,t) = -\frac{I_0\delta}{2k}\left[-\frac{4}{\delta}\left(\frac{\alpha t}{\pi}\right)^{\frac{1}{2}}\exp\left(-\frac{x^2}{4\alpha t}\right)\right.$$

$$-\left(\frac{1-\delta x}{\delta^2}-\frac{1+\delta x}{\delta^2}\right)\text{erfc}\left(\frac{x}{2\sqrt{\alpha t}}\right)$$

$$+\frac{1}{\delta^2}\exp\left(\alpha\delta^2 t-\delta x\right)\text{erfc}\left(\frac{x}{2\sqrt{\alpha t}}-\delta\sqrt{\alpha t}\right) \qquad (3.10)$$

$$+\frac{1}{\delta^2}\exp\left(\alpha\delta^2 t+\delta x\right)\text{erfc}\left(\frac{x}{2\sqrt{\alpha t}}+\delta\sqrt{\alpha t}\right)$$

$$\left.+\frac{2}{\delta^2}\exp(-\delta x)\left[1-\exp\left(\alpha\delta^2 t\right)\right]\right]$$

where:

$$\text{erfc}(x) = \frac{2}{\sqrt{\pi}}\int_x^\infty e^{-\eta^2}\,d\eta$$

knowing that

$$\text{ierfc}(x) = \int_x^\infty \text{erfc}\,\xi\,d\xi = \frac{1}{\sqrt{\pi}}\exp(-x^2) - x\,\text{erfc}(x)$$

Rearrangement of equation (3.10) gives:

$$T(x,t) = \frac{2I_0}{k}\sqrt{\alpha t}\,\text{ierfc}\left(\frac{x}{2\sqrt{\alpha t}}\right) - \frac{I_0}{k\delta}\exp(-\delta x)$$

$$+\frac{I_0}{2k\delta}\exp\left(\alpha\delta^2 t-\delta x\right)\text{erfc}\left(\delta\sqrt{\alpha t}-\frac{x}{2\sqrt{\alpha t}}\right) \qquad (3.11)$$

$$+\frac{I_0}{2k\delta}\exp\left(\alpha\delta^2 t+\delta x\right)\text{erfc}\left(\delta\sqrt{\alpha t}+\frac{x}{2\sqrt{\alpha t}}\right)$$

Equation (3.11) gives the temperature profile inside the material for a step input in beam intensity. It should be noted that, as the time tends to infinity,

$$\lim_{t \to \infty} T(x, t) = \infty$$

Therefore, no steady state solution exists for the temperature distribution.

3.2.1.b.   Non-Conduction Limited Heating

The Fourier equation governing the unsteady laser heating process may be written as [116-119]:

$$k\left(\frac{\partial^2 T}{\partial x^2}\right) + \rho\,C_p\,V\frac{\partial T}{\partial x} + I_0\,\delta\exp\left(-\delta\,x\right) = \left(\frac{\partial T}{\partial t}\right)\rho\,C_p \qquad (3.12)$$

where:

$$V = \left(\frac{k_B T_s}{2\pi m}\right)^{\frac{1}{2}} \exp\left(-\frac{L}{k_B T_s}\right)$$

It is evident that the problem is non-linear, since the melting front velocity 'V' is changing with temperature. Consequently, a complete solution to the heat transfer equation is extremely difficult, but a quasi-steady solution is feasible. The set of initial and boundary conditions relevant to equation (3.12) is: -

$$k\frac{dT}{dx}\bigg|_{x=0} = \rho VL \;\; ; \;\; \text{and} \;\; T(\infty, t) = 0 \;\; \text{and} \;\; T(x,0) = 0 \qquad (3.13)$$

The solution of equation (3.12) with the appropriate initial and boundary conditions can be obtained using a Laplace transformation with respect to time 't', as follows: -

The governing equation is: -

$$\frac{\partial^2 \overline{T}(x,p)}{\partial x^2} + \frac{V}{\alpha}\frac{\partial \overline{T}(x,p)}{\partial x} - \frac{p}{\alpha}\overline{T}(x,p) = -\frac{I_0\delta}{kp}\exp(-\delta x) \qquad (3.14)$$

The inversion of the boundary conditions gives:

$$T(x,0) = 0 \quad \text{and} \quad \left.\frac{\partial \overline{T}(x,p)}{\partial x}\right|_{x=0} = \frac{\rho VL}{kp} \qquad (3.15)$$

and

$$\overline{T}(\infty, p) = 0 \qquad (3.16)$$

The solution to equation (3.14) gives the result: -

$$\overline{T}(x,p) = A.\exp\left(-\frac{x}{\sqrt{\alpha}}\left(b - \sqrt{b^2 + p}\right)\right) + B.\exp\left(-\frac{x}{\sqrt{\alpha}}\left(b + \sqrt{b^2 + p}\right)\right)$$
$$-\frac{I_0\delta\alpha}{kp}\left[\frac{\exp(-\delta x)}{c^2 - (b^2 + p)}\right] \qquad (3.17)$$

where $b = \dfrac{V}{2\sqrt{\alpha}}$, $c = b - \delta\sqrt{\alpha}$; and 'A' and 'B' are constants of integration.

Using the initial and the boundary conditions in equation (3.13), it yields:

$$A = 0$$

Furthermore, substitution of the boundary conditions in equation (3.13) gives: -

$$B = \frac{\sqrt{\alpha}}{b + \sqrt{b^2 + p}} \left[\frac{I_0 \delta^2 \alpha}{k \cdot p(c^2 - b^2 - p)} - \frac{\rho VL}{kp} \right]$$

Therefore, the complete solution to the transformed equation is: -

$$T(x,p) = \frac{\sqrt{\alpha}}{b + \sqrt{b^2 + p}} \left[\frac{I_0 \delta^2 \alpha}{k \cdot p(c^2 - b^2 - p)} - \frac{\rho VL}{kp} \right] \exp\left[-\frac{x}{\sqrt{\alpha}} \left(b + \sqrt{b^2 + p} \right) \right]$$
$$- \frac{I_0 \delta \alpha}{kp} \left[\frac{\exp(-\delta x)}{c^2 - b^2 - p} \right]$$

$$(3.18)$$

In inversion of the transformed solution, a difficulty arises because of the first term, which is a rather complicated function of the subsidiary variable 'p'. A more elegant method is to make use of the observation that the first term may be written as the indefinite integral, that is:

$$f(x,p) = -\int_0^x \left[\frac{I_0 \delta^2 \alpha}{kp(c^2 - b^2 - p)} - \frac{\rho VL}{kp} \right] \exp\left(-\frac{x}{\sqrt{\alpha}} \left(b + \sqrt{b^2 + p} \right) \right) dx$$

$$f(x,p) = -\int_0^x g(x,p) dx$$

The inverse transformation of this function may be carried out in the following manner: -

67

$$L^{-1} f(x,p) = -L^{-1} \int_0^x g(x,p)\, dx = - \int_0^x L^{-1} g(x,p)\, dx$$

where L^{-1} is the inverse Laplace transformation. The function $g(x,p)$ is easier to invert than the function $f(x,p)$, but involves indefinite integration after the inversion process. The result of this procedure for inverting the solution is the same as that obtained in the following method of expansion into partial fractions.

Using the relationship:

$$L^{-1}\left[\varphi(p+a)\right] = e^{-at} L^{-1}\left[\varphi(p)\right]$$

It yields: -

$$L^{-1}\left[\frac{\sqrt{\alpha}}{b+\sqrt{b^2+p}} \frac{I_0\delta^2\alpha}{k.p(c^2-b^2-p)} \exp\left(-\frac{x}{\sqrt{\alpha}}\left(b+\sqrt{b^2+p}\right)\right)\right] =$$

$$-\exp\left[-\left(\frac{b.x}{\sqrt{\alpha}}+b^2 t\right)\right] L^{-1}\left[\frac{I_0\delta^2\alpha \exp(-qx)}{k(p-b^2)(p-c^2)\left(q+\dfrac{b}{\sqrt{\alpha}}\right)}\right]$$

where $\quad q^2 = \dfrac{p}{\alpha}, \quad b = \dfrac{V}{2\alpha} \quad$ and $\quad c = b - \delta\sqrt{\alpha}$

This expression may be expanded into partial fractions using the residual theorem:

68

$$-\frac{I_0\delta^2}{k\alpha}\exp\left[-\left(\frac{bx}{\sqrt{\alpha}}+b^2 t\right)\right]L^{-1}\left[\frac{\alpha\sqrt{\alpha}\ \exp(-cx)}{2b\left(b^2-c^2\right)\left(q+\dfrac{b}{\sqrt{\alpha}}\right)^2}\right.$$

$$-\frac{\alpha^2\left(5b^2-c^2\right)\exp(-qx)}{4b^2\left(b^2-c^2\right)^2\left(q+\dfrac{b}{\sqrt{\alpha}}\right)}+\frac{\alpha^2\exp(-qx)}{4b^2\left(b^2-c^2\right)\left(q-\dfrac{b}{\sqrt{\alpha}}\right)}$$

$$\left.-\frac{\alpha^2\exp(-qx)}{2c\left(b+c\right)\left(b^2-c^2\right)\left(q-\dfrac{c}{\sqrt{\alpha}}\right)}+\frac{\alpha^2\exp(-qx)}{2c\left(b-c\right)\left(b^2-c^2\right)\left(q+\dfrac{c}{\sqrt{\alpha}}\right)}\right]$$

which gives on inversion and after much algebraic manipulations:

$$\frac{I_0\delta\sqrt{\alpha}}{2\rho C_p(\alpha\delta-V)}\left\{4\sqrt{t}\ \mathrm{ierfc}\left(\frac{x}{2\sqrt{\alpha t}}+b\sqrt{t}\right)+\frac{3b^2+c^2}{2b\left(b^2-c^2\right)}\ \mathrm{erfc}\left(\frac{x}{2\sqrt{\alpha t}}+b\sqrt{t}\right)\right.$$

$$+\frac{1}{2b}\ \exp\left(-\frac{2bx}{\sqrt{\alpha}}\right)\mathrm{erfc}\left(\frac{x}{2\sqrt{\alpha t}}-b\sqrt{t}\right)$$

$$-\frac{1}{(b-c)}\ \exp\left[-\left[\delta x+\left(b^2-c^2\right)t\right]\right]\mathrm{erfc}\left[\left(\frac{x}{2\sqrt{\alpha t}}+c\sqrt{t}\right)\right]$$

$$\left.-\frac{1}{(b+c)}\ \exp\left[\frac{x}{\sqrt{\alpha}}(b+c)+\left(b^2-c^2\right)t\right]\mathrm{erfc}\left(\frac{x}{2\sqrt{\alpha t}}-c\sqrt{t}\right)\right\}$$

(3.19)

The second part of the term in the transformed solution may be inverted in a similar

manner:

$$L^{-1}\left[\frac{\rho VL\sqrt{\alpha}}{kp}\ \frac{\exp\left(-\dfrac{x}{\sqrt{\alpha}}\left(b+\sqrt{b^2+p}\right)\right)}{\left(b+\sqrt{b^2+p}\right)}\right]$$

$$=\frac{\rho VL}{4kb^2}\exp\left[-\left(b^2t+\frac{bx}{\sqrt{\alpha}}\right)\right]L^{-1}\left[\frac{\exp(-qx)}{\left(q-\dfrac{b}{\sqrt{\alpha}}\right)}-\frac{\exp(-qx)}{\left(q+\dfrac{b}{\sqrt{\alpha}}\right)}-\frac{2b}{\sqrt{\alpha}}\frac{\exp(-qx)}{\left(q+\dfrac{b}{\sqrt{\alpha}}\right)^2}\right]$$

which after transformation gives: -

$$\frac{\rho VL}{4bk}\left\{4b\sqrt{\alpha t}\ \text{ierfc}\left(\frac{x}{2\sqrt{\alpha t}}+b\sqrt{t}\right)-\sqrt{\alpha}\ \text{erfc}\left(\frac{x}{2\sqrt{\alpha t}}+b\sqrt{t}\right)\right.$$
$$\left.+\sqrt{\alpha}\ \exp\left(\frac{-2bx}{\sqrt{\alpha}}\right)\text{erfc}\left(\frac{x}{2\sqrt{\alpha t}}-b\sqrt{t}\right)\right\}$$

(3.20)

Finally the term:

$$L^{-1}\left[\frac{I_0\alpha\delta}{k}\ \frac{\exp(-\delta x)}{p\left(p+b^2-c^2\right)}\right]$$

$$=\frac{I_0\delta}{\rho C_p}\exp(-\delta x)L^{-1}\left[\frac{1}{\left(c^2-b^2\right)\left(p+b^2-c^2\right)}-\frac{1}{\left(c^2-b^2\right)p}\right]$$

(3.21)

or

$$L^{-1}=\frac{I_0\delta\sqrt{\alpha}}{\rho C_p\left(\alpha\delta-V\right)}\left[\frac{\exp\left[-\left(\delta x+\left(b^2-c^2\right)t\right)\right]}{\left(b-c\right)}-\frac{\exp(-\delta x)}{\left(b-c\right)}\right]$$

where $b-c=\delta\sqrt{\alpha}$

Substitution of all these terms (equations 3.19, 3.20 and 3.21) into equation (3.18) gives the complete solution of equation (3.12) yields:

$$
\begin{aligned}
T(x,t) = \frac{I_0 \delta \sqrt{\alpha}}{2\rho C_p (\alpha\delta - V)} &\left\{ 4\sqrt{t}\ \text{ierfc}\left(\frac{x}{2\sqrt{\alpha t}} + b\sqrt{t}\right) \right. \\
&+ \frac{3b^2 + c^2}{2b(b^2 - c^2)}\ \text{erfc}\left(\frac{x}{2\sqrt{\alpha t}} + b\sqrt{t}\right) + \frac{1}{2b}\exp\left(-\frac{2bx}{\sqrt{\alpha}}\right)\text{erfc}\left(\frac{x}{2\sqrt{\alpha t}} - b\sqrt{t}\right) \\
&+ \frac{1}{(b-c)}\exp\left[-\left(\delta x + (b^2 - c^2)\,t\right)\right]\text{erfc}\left[-\left(\frac{x}{2\sqrt{\alpha t}} + c\sqrt{t}\right)\right] \\
&+ \frac{1}{(b+c)}\exp\left[-\frac{x}{\sqrt{\alpha}}(b+c) + (b^2 - c^2)\,t\right]\text{erfc}\left(\frac{x}{2\sqrt{\alpha t}} - c\sqrt{t}\right) \\
&\left. - \frac{2}{(b-c)}\exp(-\delta x)\right\} - \frac{\rho VL}{4bk}\left\{ 4b\sqrt{\alpha t}\ \text{ierfc}\left(\frac{x}{2\sqrt{\alpha t}} + b\sqrt{t}\right) \right. \\
&\left. -\sqrt{\alpha}\ \text{erfc}\left(\frac{x}{2\sqrt{\alpha t}} + b\sqrt{t}\right) + \sqrt{\alpha}\exp\left(-\frac{2bx}{\sqrt{\alpha}}\right)\text{erfc}\left(\frac{x}{2\sqrt{\alpha t}} - b\sqrt{t}\right)\right\}
\end{aligned}
\tag{3.22}
$$

Setting x = 0 in equation (3.22) results in the surface temperature, that is:

$$
\begin{aligned}
T(0,t) = \frac{I_0 \delta \sqrt{\alpha}}{2\delta C_p (\alpha\delta - V)} &\left(4\sqrt{t}\ \text{ierfc}(b\sqrt{t}) + \frac{(b^2 + c^2)}{b(b^2 - c^2)}\ \text{erfc}(b\sqrt{t}) + \frac{1}{b} \right. \\
&\left. + \frac{\exp\left[(b^2 - c^2)t\right]}{(b-c)}\text{erfc}(-c\sqrt{t}) - \frac{\exp\left[-(b^2 - c^2)t\right]}{(b+c)}\text{erfc}(-c\sqrt{t}) - \frac{2}{(b-c)} \right) \\
&- \frac{\rho VL}{4bk}\left[4b\sqrt{\alpha t}\ \text{ierfc}(b\sqrt{t}) - \sqrt{\alpha}\ \text{erfc}(b\sqrt{t}) + \sqrt{\alpha}\,(2 - \text{erfc}(b\sqrt{t})) \right]
\end{aligned}
$$

rearrangement gives: -

71

$$T(0,t) = \frac{I_0 \, \delta \sqrt{\alpha}}{2 \rho \, C_p \, (\alpha \, \delta - V)} \left(4 \sqrt{t} \; \mathrm{ierfc} \, (b \sqrt{t}) + \frac{(b^2 + c^2)}{b \, (b^2 - c^2)} \; \mathrm{erfc} \, (b \sqrt{t}) \right.$$

$$+ \frac{2c}{b^2 - c^2} \exp \left[-(b^2 - c^2) \, t \right] \mathrm{erfc} \, (-c \sqrt{t}) - \frac{(b+c)}{b \, (b-c)} \right) \tag{3.23}$$

$$- \frac{\rho V L}{2 \, b \, k} \left[2 \, b \sqrt{\alpha t} \; \mathrm{ierfc} \, (b \sqrt{t}) + \sqrt{\alpha} \; \mathrm{erfc} \, (b \sqrt{t}) \right]$$

Equations (3.22) and (3.23) are the complete quasi-steady solution of the governing equation and can be used to form the basis for a more accurate solution which can be obtained by an iterative procedures. It is expected that this solution would be obtained by developing the solution from time $t = 0$. In the initial stages, the melting rates are small and thus the solution is for the pure conduction process. As the surface temperature rises, the melting rate also rises. The values for the velocity and surface temperature can be obtained by stepping forward in time using time steps that are small enough such that the change in the surface velocity between steps is small and therefore the velocity derived in the previous step can be used directly in equation (3.23). With this new value of the surface temperature, an improved estimate of the melting velocity 'V' can be obtained, and the iteration repeated to give a convergent solution.

3.2.2 Step Input Intensity Laser Pulse with Convection Boundary Conditions:

The equation describing the heat accompanying with convection in a constant property one-dimensional material with a laser energy source is [118-121]: -

$$k \frac{\partial^2 T}{\partial x^2} + Sq = \rho C_p \frac{\partial T}{\partial t} \qquad (3.24)$$

The energy source term is modelled, for a material that absorbs internally the laser energy, as: -

$$Sq = A_b I_0 \delta \exp(-\delta x)$$

and

$$A_b = 1-R$$

where 'R' is the surface reflectance and $R=1-A_b$. This equation assumes no spatial variation of I_0 in the plane normal to the beam. In addition, the diffusion perpendicular to the beam 'x' direction can be ignored. Approximately 95% of the laser energy is absorbed within a depth of $\delta/3$. For metals in which δ is of the order of 10^5 cm^{-1} [111], therefore 95% of the laser energy will be absorbed within a depth of 3×10^{-5} cm. This can be considered as a skin effect. In the case of 'δ' is considerably

73

smaller and energy is deposited over a greater thickness. The initial condition is assumed to be a uniform temperature.

$$T(x,0) = T_0 \tag{3.25}$$

and the boundary conditions are: -

$$-k\frac{\partial T(0,t)}{\partial x} = h[T_\infty - T(0,t)] \tag{3.26}$$

and

$$\frac{\partial T(\infty,t)}{\partial x} = 0 \tag{3.27}$$

The maximum temperature will occur, in this case, at the surface instead of in-depth.

The temperature rises above the initial temperature is defined as $\theta = T - T_0$

The laser energy equation and the boundary conditions can be written as: -

$$\frac{\partial \theta}{\partial t} = \alpha \frac{\partial^2 \theta}{\partial x^2} + \frac{Sq}{\rho C_p} \tag{3.28}$$

Now, the initial condition becomes: -

$$T(0,t) \quad \theta(x,0) = 0 \tag{3.29}$$

and the boundary conditions are: -

$$\frac{\partial \theta(0,t)}{\partial x} + \frac{h}{k}[T_\infty - T_0 - \theta(0,t)] = 0 \qquad (3.30)$$

$$\frac{\partial \theta(\infty,t)}{\partial x} = 0 \qquad (3.31)$$

Let $\bar{\theta}(x,p)$ denotes the Laplace transform of $\theta(x,t)$ with respect to time 't'. Taking the Laplace transform of equation (3.28), it yields: -

$$p\,\bar{\theta}(x,p) - \theta(x,0) = \alpha \frac{d^2\,\bar{\theta}(x,p)}{dx^2} + \frac{I_0(1-R)\delta \exp(-\delta x)}{\rho C_p}\frac{1}{p} \qquad (3.32)$$

Making use of the initial condition on the temperature rises above the initial temperature, 'θ', and rearranging, equation (3.36) can be written as:

$$\frac{d^2\,\bar{\theta}(x,p)}{dx^2} - \frac{p}{\alpha}\bar{\theta}(x,p) = -\frac{I_0(1-R)\delta \exp(-\delta x)}{k}\frac{1}{p} \qquad (3.33)$$

The transformed boundary conditions become;

$$\frac{d\,\bar{\theta}(0,p)}{dx} + \frac{h}{k}\left[\frac{(T_\infty - T_0)}{p} - \bar{\theta}(0,p)\right] = 0 \qquad (3.34)$$

$$\frac{d\bar{\theta}(\infty,p)}{dx} = 0 \qquad\qquad (3.35)$$

The solution to equation (3.33) can be written as:

$$\bar{\theta}(x,p) = A\exp\left(\sqrt{\frac{p}{\alpha}}x\right) + B\exp\left(-\sqrt{\frac{p}{\alpha}}x\right) - \frac{I_0(1-R)\delta\exp(-\delta x)}{k}\frac{1}{p}\frac{1}{\delta^2 - \dfrac{p}{\alpha}} \qquad (3.36)$$

The constant 'A' must be zero for the temperature to remain finite at $x = \infty$. Applying equation (3.34), the 'B' can be evaluated. The final solution in the transform space is: -

$$\bar{\theta}(x,p) = \left[\frac{\dfrac{h(T\infty - T_0)}{k}\dfrac{1}{p} + \dfrac{I_0(1-R)\delta\left(\delta + \dfrac{h}{k}\right)}{k}\dfrac{1}{p}\dfrac{1}{\delta^2 - \dfrac{p}{\alpha}}}{\sqrt{\dfrac{p}{\alpha}\dfrac{h}{k}}}\right]\exp\left(-\sqrt{\frac{p}{\alpha}}x\right)$$

$$-\frac{I_0(1-R)\delta\exp(-\delta x)}{k}\frac{1}{p}\frac{1}{\delta^2 - \dfrac{p}{\alpha}} \qquad (3.37)$$

The inverse Laplace transform of equation (3.37) can be determined using standard Laplace transform tables. The following algebraic relationship will be helpful: -

$$\frac{1}{p(\sqrt{p}-b)(\sqrt{p}+b)(\sqrt{p}+a)} = -\frac{1}{ab^2}\frac{1}{p} - \frac{1}{a(a^2-b^2)}\frac{1}{\sqrt{p}(\sqrt{p}+a)}$$
$$-\frac{(a-b)}{2b^2(a^2-b^2)}\frac{1}{\sqrt{p}(\sqrt{p}-b)} \qquad (3.38)$$
$$+\frac{(a+b)}{2b^2(a^2-b^2)}\frac{1}{\sqrt{p}(\sqrt{p}+b)}$$

The following inverse Laplace transform relationships will be used [120]: -

$$\pounds^{-1}\left[\frac{a\exp(-k\sqrt{p})}{p(\sqrt{p}+a)}\right] = -\exp(a^2t+ak)\operatorname{erfc}\left(\frac{k}{2\sqrt{t}}+a\sqrt{t}\right)+\operatorname{erfc}\left(\frac{k}{2\sqrt{t}}\right)$$

$$\pounds^{-1}\left[\frac{\exp(-k\sqrt{p})}{p}\right] = \operatorname{erfc}\left(\frac{k}{2\sqrt{t}}\right)$$

$$\pounds^{-1}\left[\frac{\exp(-k\sqrt{p})}{\sqrt{p}(\sqrt{p}+a)}\right] = \exp(a^2t+ak)\operatorname{erfc}\left(\frac{k}{2\sqrt{t}}+a\sqrt{t}\right)$$

$$\pounds^{-1}\left[\frac{1}{p(p-b)}\right] = \frac{1}{b}[\exp(bt)-1]$$

The inverse transform of equation (3.37) can be written, using the above Laplace transform relationship, as: -

$$\theta = (T_\infty - T_0)\left[\operatorname{erfc}\left(\frac{x}{2\sqrt{\alpha t}}\right) - \exp\left(\frac{h^2}{k^2}\alpha t + \frac{h\,x}{k}\right)\operatorname{erfc}\left(\frac{x}{2\sqrt{\alpha t}} + \frac{h}{k}\sqrt{\alpha t}\right)\right]$$

$$+ \frac{I_0(1-R)}{\delta k}\left\{ \begin{aligned} &\left(1 + \frac{\delta k}{h}\right)\operatorname{erfc}\left(\frac{x}{2\sqrt{\alpha t}}\right) \\ &+ \frac{1}{\dfrac{h}{\delta k}\left(\dfrac{h}{\delta k} - 1\right)}\exp\left(\frac{h^2}{k^2}\alpha t + \frac{h\,x}{k}\right)\operatorname{erfc}\left(\frac{x}{2\sqrt{\alpha t}} + \frac{h}{k}\sqrt{\alpha t}\right) \\ &- \frac{1}{2}\left(\frac{\dfrac{h}{\delta k} + 1}{\dfrac{h}{\delta k} - 1}\right)\exp\left(\delta^2\alpha t + \delta x\right)\operatorname{erfc}\left(\frac{x}{2\sqrt{\alpha t}} + \delta\sqrt{\alpha t}\right) \\ &- \frac{1}{2}\exp\left(\delta^2\alpha t - \delta x\right)\operatorname{erfc}\left(\frac{x}{2\sqrt{\alpha t}} - \delta\sqrt{\alpha t}\right) + \exp(-\delta x)\left[\exp\left(\delta^2\alpha t\right) - 1\right] \end{aligned} \right\}$$

(3.39)

The term in equation (3.39) multiplied by $(T_\infty - T_0)$ is the solution for a semi-infinite material with uniform initial temperature T_0. The term multiplied by I_0 (1-R) accounts for heat flow due to the laser energy deposition. No energy source and convection boundary conditions account for heat loss or gain when T_∞ and T_0 are different.

Even when $T_0 = T_\infty$, there will still be heat loss because the energy deposition is causing the surface temperature to rise. Therefore, equation (3.39) can be written as:

$$\theta = \frac{I_0(1-R)}{\delta k}\left\{ \begin{array}{l} \left(1+\dfrac{\delta k}{h}\right)\operatorname{erfc}\left(\dfrac{x}{2\sqrt{\alpha t}}\right) \\[2ex] +\dfrac{1}{\dfrac{h}{\delta k}\left(\dfrac{h}{\delta k}-1\right)}\exp\left(\dfrac{h^2}{k^2}\alpha t+\dfrac{hx}{k}\right)\operatorname{erfc}\left(\dfrac{x}{2\sqrt{\alpha t}}+\dfrac{h}{k}\sqrt{\alpha t}\right) \\[2ex] -\dfrac{1}{2}\left(\dfrac{\dfrac{h}{\delta k}+1}{\dfrac{h}{\delta k}-1}\right)\exp\left(\delta^2\alpha t+\delta x\right)\operatorname{erfc}\left(\dfrac{x}{2\sqrt{\alpha t}}+\delta\sqrt{\alpha t}\right) \\[2ex] -\dfrac{1}{2}\exp\left(\delta^2\alpha t-\delta x\right)\operatorname{erfc}\left(\dfrac{x}{2\sqrt{\alpha t}}-\delta\sqrt{\alpha t}\right)+\exp(-\delta x)\left[\exp\left(\delta^2\alpha t\right)-1\right] \end{array} \right\}$$

or

$$\frac{T-T_0}{\dfrac{I_0(1-R)}{\delta k}} = \left(1+\frac{\delta k}{h}\right)\operatorname{erfc}\left(\frac{x}{2\sqrt{\alpha t}}\right)$$

$$+\frac{1}{\dfrac{h}{\delta k}\left(\dfrac{h}{\delta k}-1\right)}\exp\left(\frac{h^2}{k^2}\alpha t+\frac{hx}{k}\right)\operatorname{erfc}\left(\frac{x}{2\sqrt{\alpha t}}+\frac{h}{k}\sqrt{\alpha t}\right)$$

$$-\frac{1}{2}\left(\frac{\dfrac{h}{\delta k}+1}{\dfrac{h}{\delta k}-1}\right)\exp\left(\delta^2\alpha t+\delta x\right)\operatorname{erfc}\left(\frac{x}{2\sqrt{\alpha t}}+\delta\sqrt{\alpha t}\right) \qquad (3.40)$$

$$-\frac{1}{2}\exp\left(\delta^2\alpha t-\delta x\right)\operatorname{erfc}\left(\frac{x}{2\sqrt{\alpha t}}-\delta\sqrt{\alpha t}\right)$$

$$+\exp(-\delta x)\left[\exp\left(\delta^2\alpha t\right)-1\right]$$

Equation (3.40) is used when computing the temperature profiles in the substrate due to convective boundary condition.

CHAPTER- 4

RESULTS AND DISCUSSIONS

4.1 Heat Transfer Analysis

The temperature profiles obtained from the conduction-limited and non-conduction-limited heating are given below: -

The variations of surface temperature resulting from conduction-limited and non-conduction-limited heating with time are shown in figures (4.1) to (4.3). For both types of heating, the surface temperature rises rapidly in the beginning of the pulse. This may be due to heat transfer taking place through electron-phonon collisions inside the material, i.e., electrons close to the surface absorb the incident laser radiation and transfer their excess energy to phonon through an increased rate of collision. The higher the energy of the electron the higher the rate of collision. As the melting temperature is approached, the probability of molecules forming the liquid phase does not increase as much as the probability of collisions occurring at the surface. Consequently, the energy gained due to laser beam irradiation enhances the increase of internal energy of the melt, rather than increasing the number of

molecules, which exist in the liquid form [119]. Under these conditions, the internal energy of the substrate increases due to increased phonon energy, which in turn gives rise to high surface temperature. Figure (4.1) shows the results for two values of power intensity (I_0) for conduction-limited heating.

A comparison of figures (4.2) and (4.3) shows a similar trend of rise in temperature for non-conduction limited case with convective boundary conditions. As the intensity of the incident beam increases, however, the temperature rise also increases. This increase is more pronounced as the heating progresses. In this case, the energy transferred from the electrons to the lattice site atoms becomes considerable, i.e. the lattice site atom temperature rises at a relatively faster rate. The effect of heat transfer coefficient on the surface temperature profiles is negligible. This may occur because of the fact that the energy absorbed by the substrate is converted into internal energy rather than being transferred from the surface to the environment through the convection. It is, therefore, expected that the loss of energy due to convection from the surface is considerably smaller compared with the internal energy gain of the substrate.
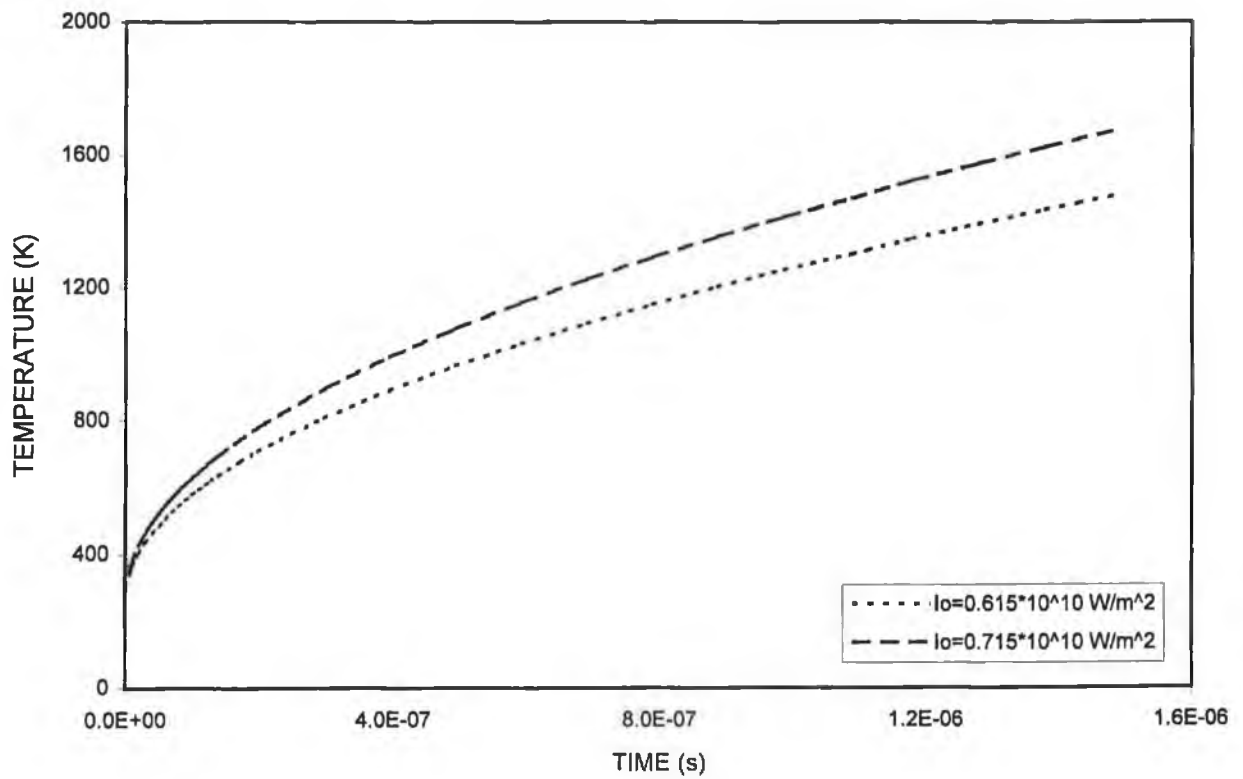
Figure-4.1   Variation of surface temperature predicted from the theory with time.
I$_0$ is the laser power intensity.

Using Equation No. 3.11.
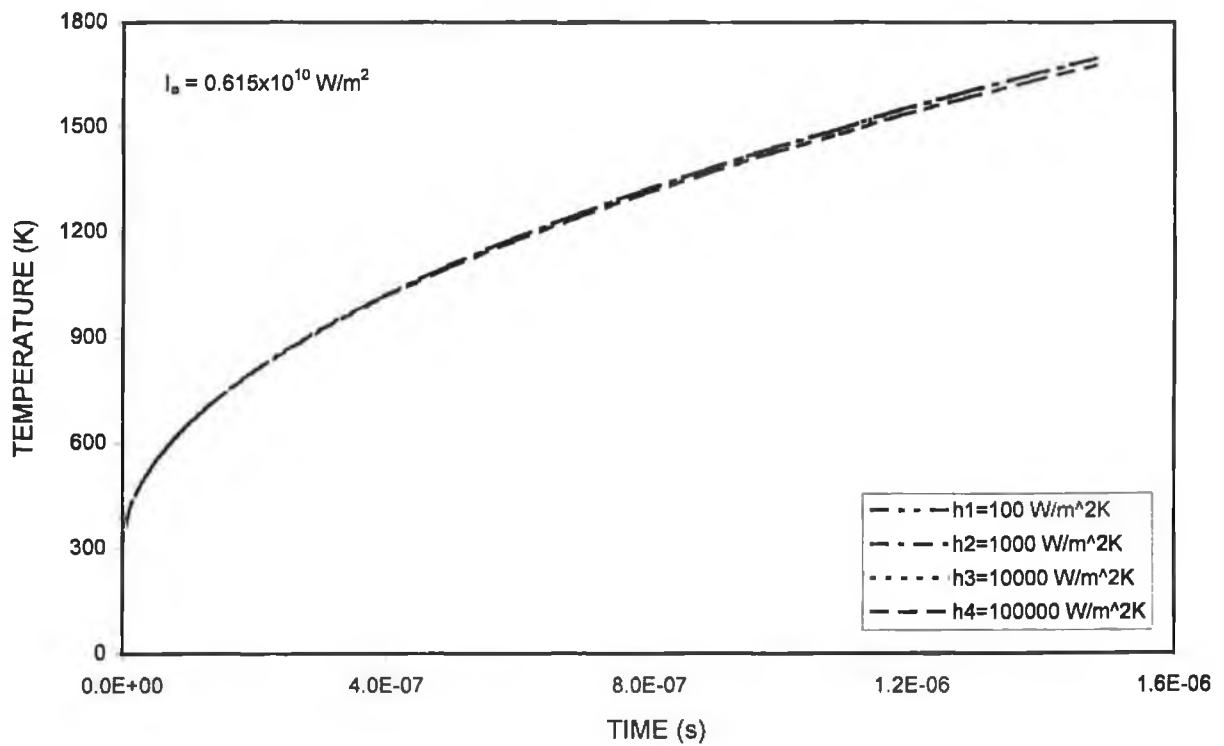
Figure-4.2   Variation of surface temperature predicted from the theory with time. I_0 is the laser power intensity and h is the heat transfer coefficient. Using Equation No. 3.40 when x=0, (x = 0 is the surface).
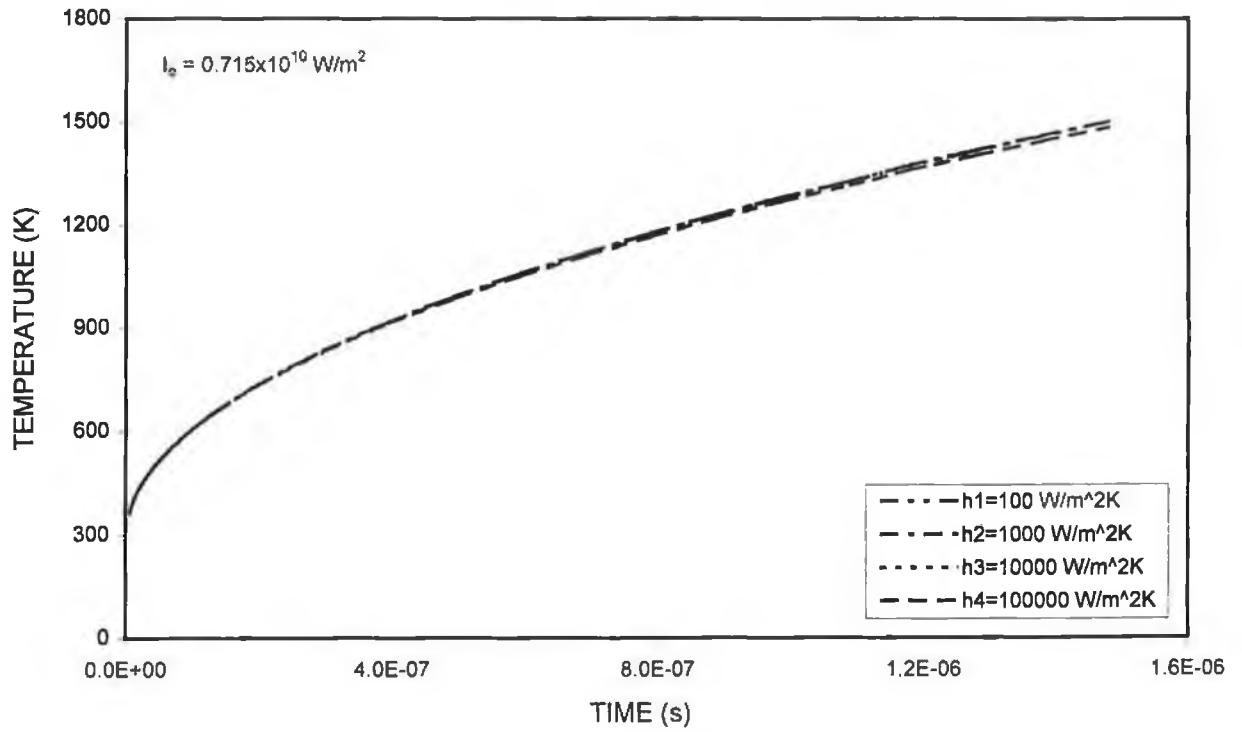
Figure-4.3   Variation of surface temperature predicted from the theory with time.
I_0 is the laser power intensity and h is the heat transfer coefficient.
Using Equation No. 3.40 when x=0, (x = 0 is the surface).

Figures (4.4) to (4.6) show the temperature profiles inside the substrate. In general, in the case of conduction-limited heating (figure 4.4), the temperature decays smoothly with increasing dimensionless distance. As the intensity increases, the resulting temperature profile is shifted towards higher values. In this case, the temperature shift in the surface region becomes slightly higher than that corresponding to some distance away from the surface. This may be due to the absorption process, i.e., the absorption of the incident beam is considerably high in the surface region, which in turn increases the internal energy gain in this region. The net result is the increase in the temperature in the surface region.
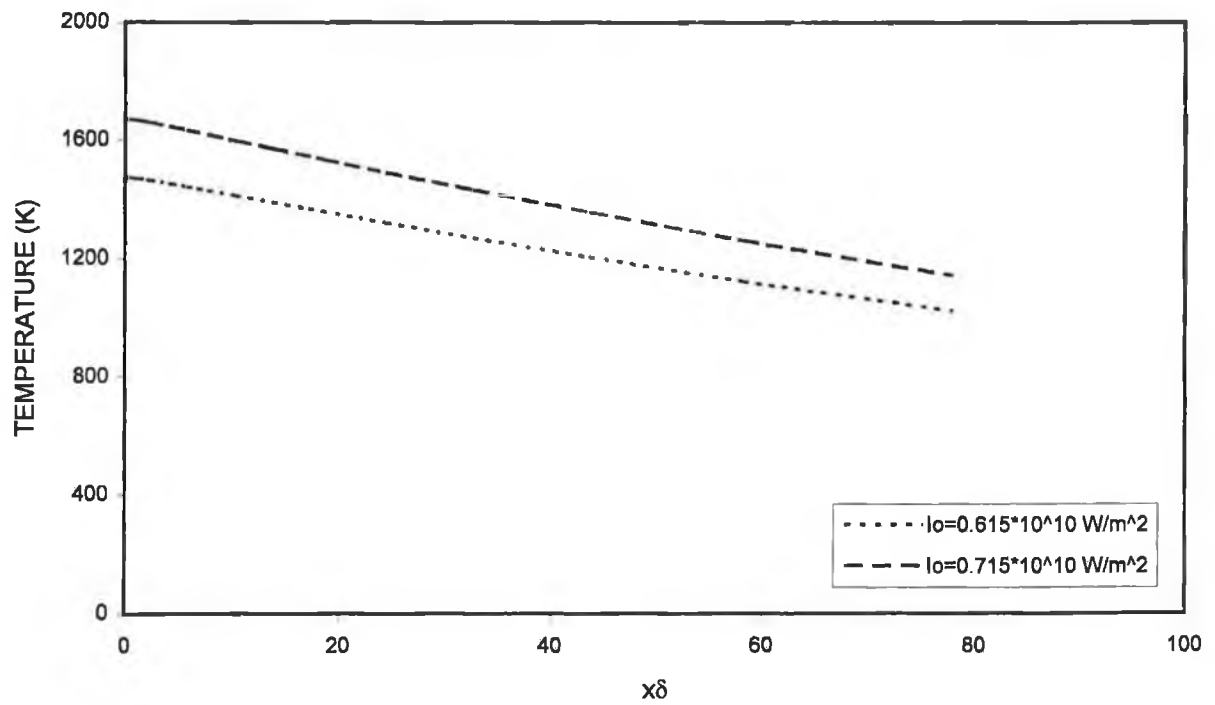
Figure-4.4   Temperature variation with dimensionless distance (xδ) inside the material.
I_0 is the laser power intensity ($\delta = 10^6$ 1/m).
Using Equation No. 3.11.
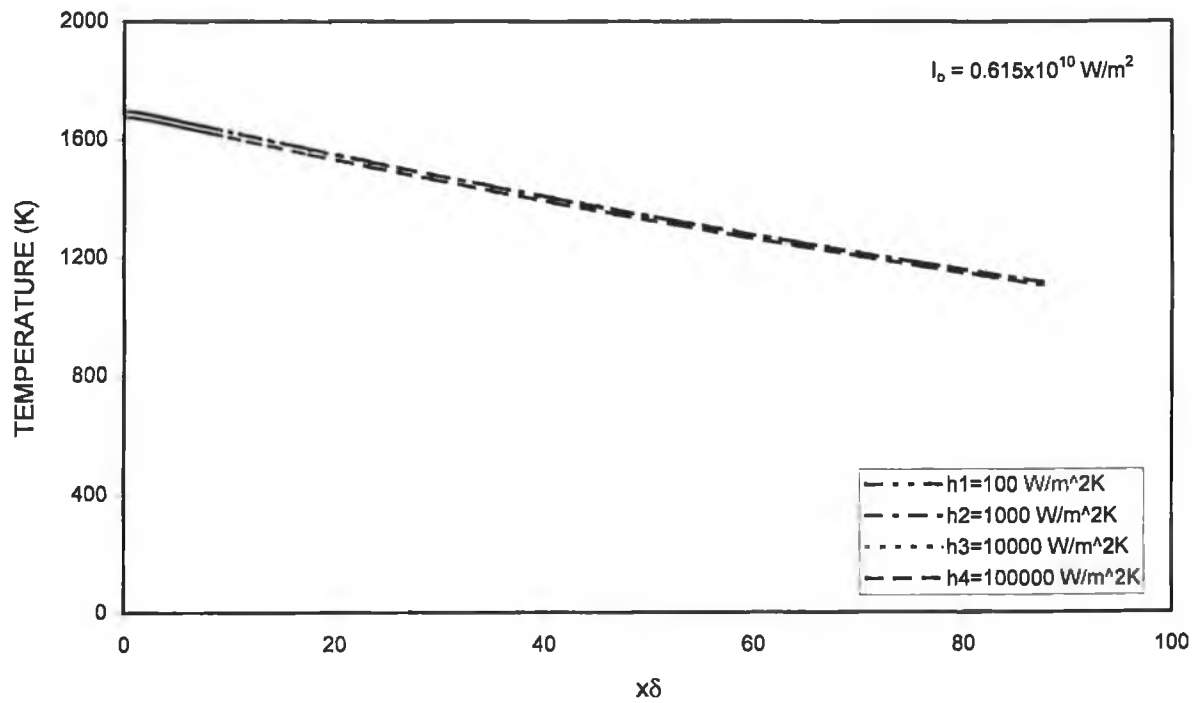
Figure-4.5   Temperature variation with dimensionless distance (xδ) inside the material.
I_0 is the laser power intensity and h is the heat transfer coefficient.
Using Equation No. 3.40 when x >= 0.
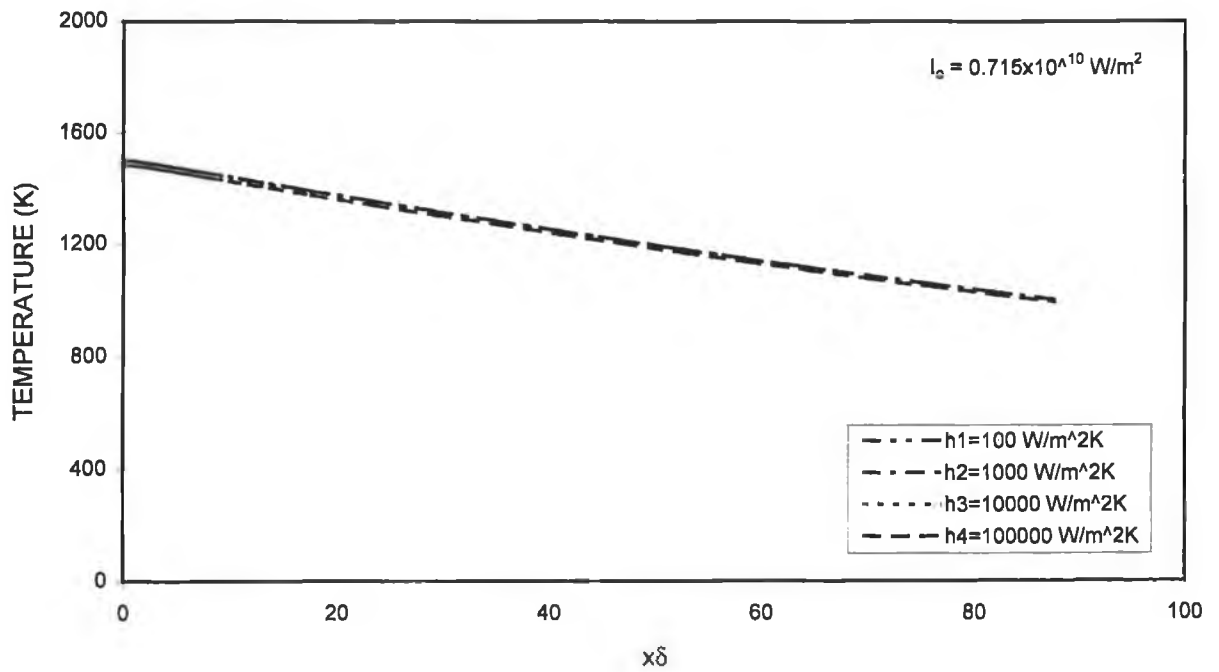
Figure-4.6 Temperature variation with dimensionless distance (xδ) inside the I_0 is the laser power intensity and h is the heat transfer coefficient. Using Equation No. 3.40 when x >= 0.

88

A similar argument is true for the non-conduction heating process as shown in figure (4.7). Due to the phase change occurring in the vicinity of the surface, however, the rise of the surface temperature slows down slightly. This occurs because of the phase change, which resulted during the melting process. In the melting region, where the temperature attains a value higher than the melting temperature of the substrate, a superheated liquid phase occurs. This gives rise to high melting region in the substrate. As the temperature becomes almost equal to, or slightly higher than, the substrate melting temperature the low melting region occurs in the substrate.
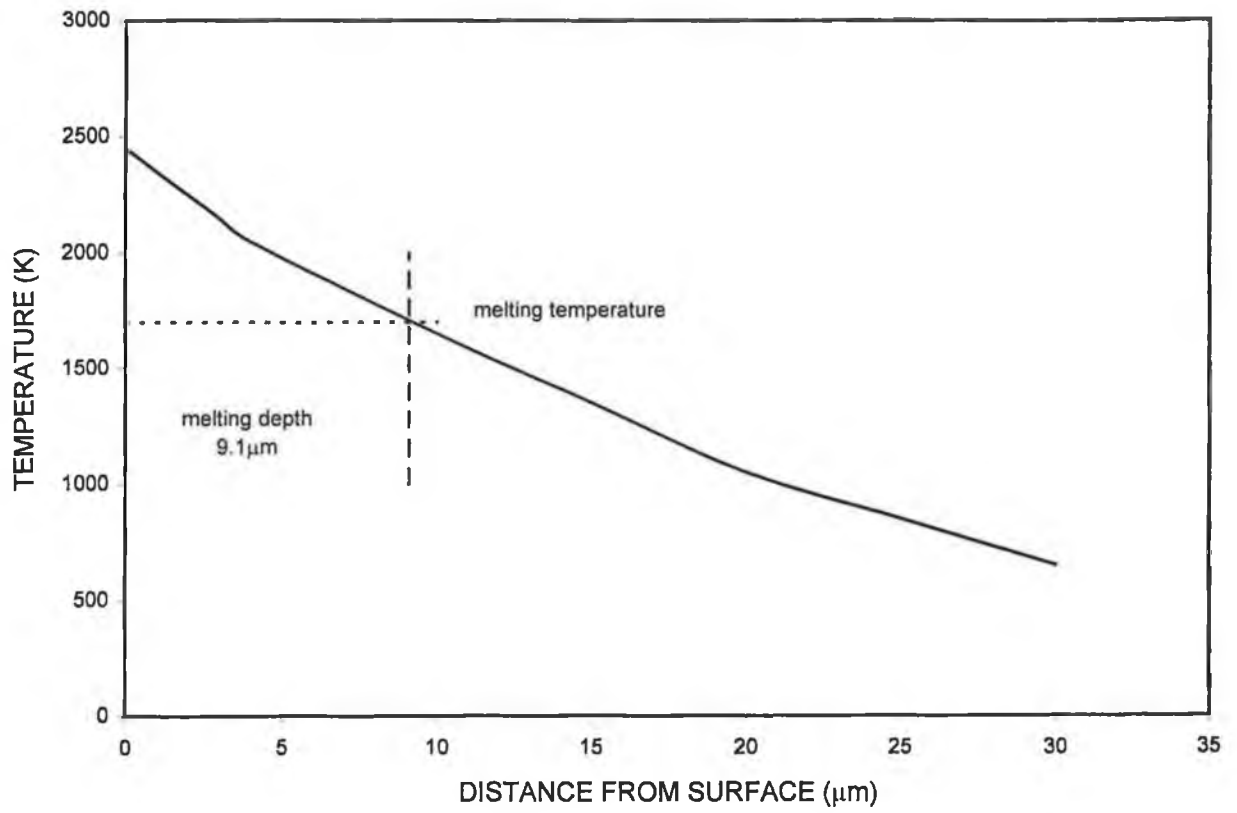
Figure-4.7   Temperature profiles inside the material predicte
Using Equation No. 3.22 when x >= 0.

The variation of temperature gradient dT/dt with time is shown in figures (4.8) to (4.10). The gradient dT/dt in figure (4.8) for conduction-limited heating decreases rapidly in the surface region and then attains a plateau with increasing time. The rapid decay of dT/dt indicates that the internal energy gain in the beginning of the pulse is considerable, in which case almost all of the energy absorbed by the substrate is converted into internal energy gain rather than conducted towards the bulk of the material. As the heating progresses, the conduction losses and the internal energy gain balance each other. In this case, the dT/dt almost reaches the steady state. It should also be noted that the effect of pulse intensity on the dT/dt is more pronounced in the early heating times. In addition, the effect of the heat transfer coefficient on dT/dt variation with time is negligible, i.e., the convective loss from the surface is minimal, as indicated before. This is shown in figures (4.9) and (4.10) for non-conduction heating case.
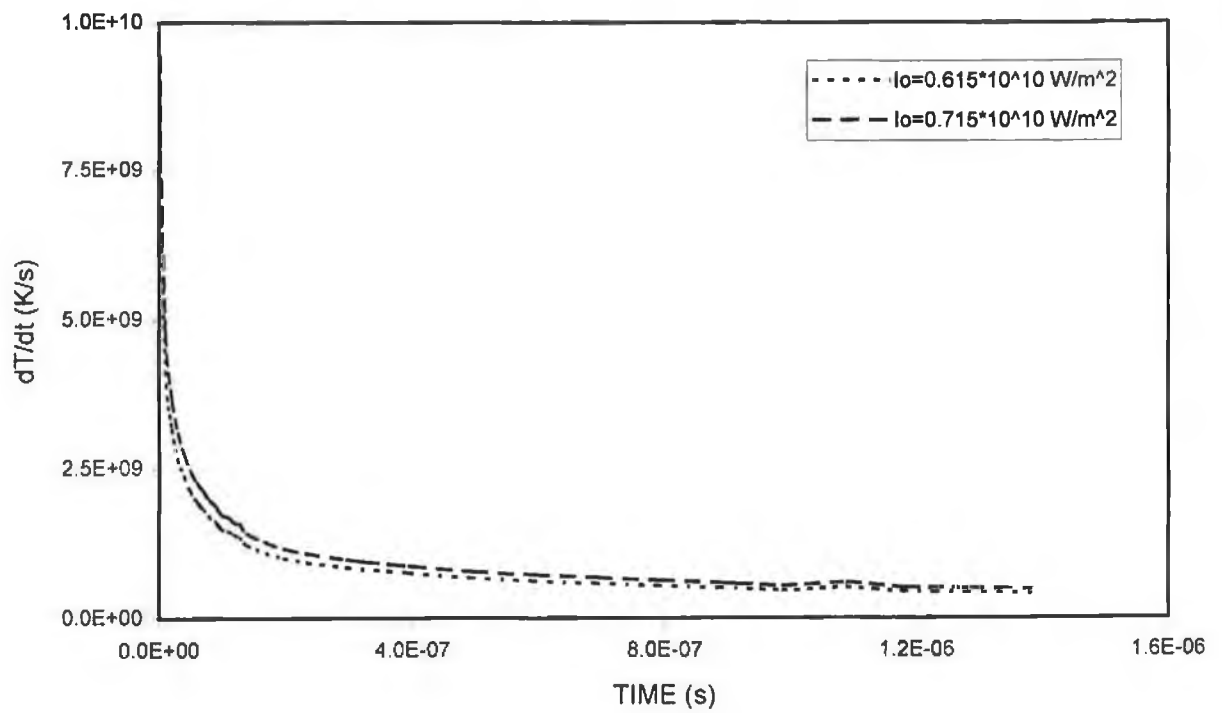
Figure-4.8   Variation of temperature gradient dT/dt with time predicted from the theory. I_0 is the laser power intensity.
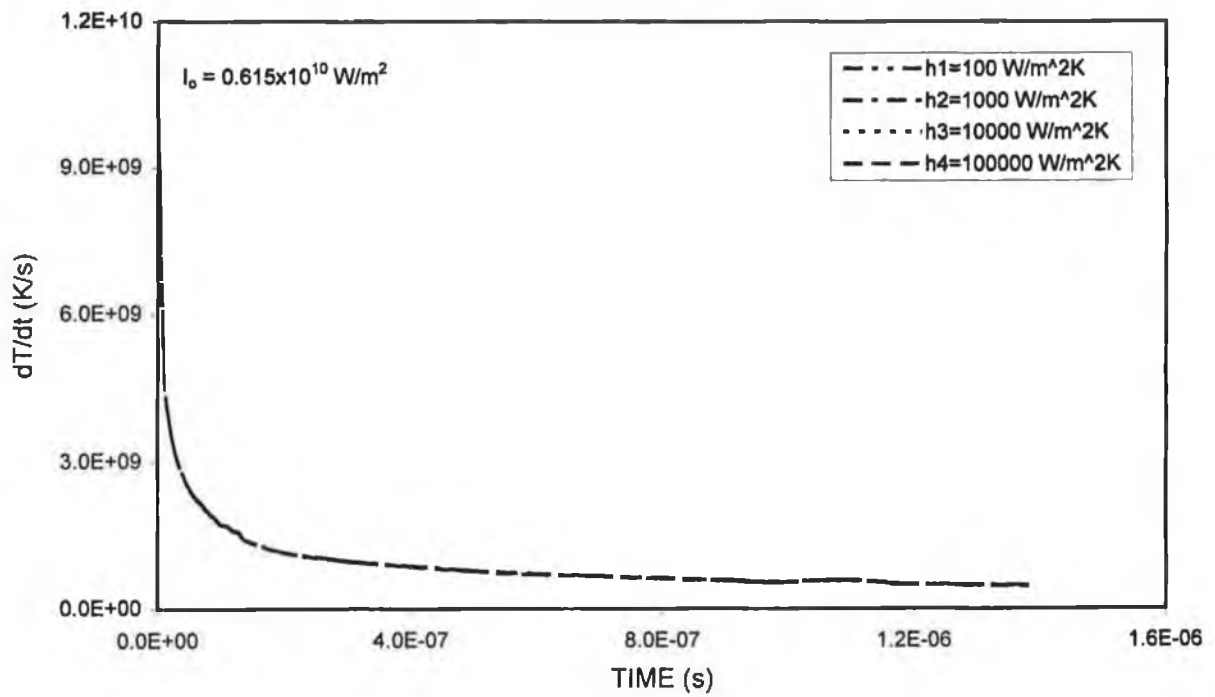
Using Equation No. 3.11

Figure-4.9 Variation of temperature gradient dT/dt with time predicted from the theory. I_0 is the laser power intensity and h is the heat transfer coefficient. Using Equation No. 3.40 when x=0.
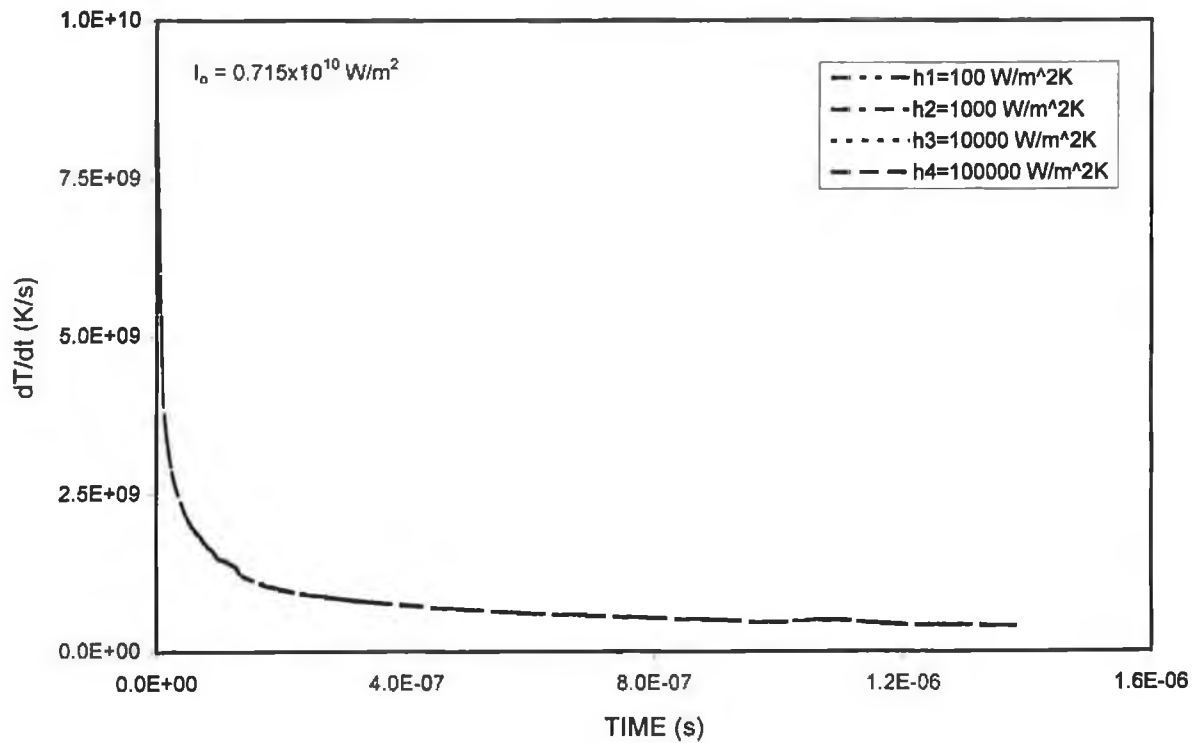
Figure-4.10   Variation of temperature gradient dT/dt with time predicted from the theory I_0 is the laser power intensity and h is the heat transfer coefficient.

Using Equation No. 3.40 when x=0.

Figures (4.11) to (4.13) show dT/dx variation with dimensionless distance (xδ). In general, the slope of the curves decreases reaching a minimum and then increases slightly where the temperature profile becomes almost asymptotic with xδ. In this case, the behavior of dT/dx with xδ may be distinguished into three regions, which are indicated in figure (4.11). In the first region, the heat gain due to laser irradiation dominates the losses due to the conduction, i.e., the internal energy increase is very high compared to conduction losses. In the second region, the slope has a minimum value. In this case, the energy gain due to incident laser beam balances the conduction losses, i.e., the internal energy of the substance remains almost constant. The dimensionless distance (xδ) corresponding to this point may be defined as the equilibrium distance and dT/dx becomes (dT/dx)$_{min}$. In the third region, the slope increases to reach a higher value. In this region, conduction losses are dominant and the energy gain due to the external field is insignificant, i.e., the internal energy decreases as the dimensionless distance increases. For the non-conduction-limited case, figures (4.12) and (4.13) show the influence of power intensity on the dT/dx variation with xδ. As the power intensity increases dT/dx attains the low values, in which case, the equilibrium distance moves towards the bulk of the workpiece material. Consequently, the effect of heat transfer coefficient on the resulting dT/dx curves is not considerable. This indicates that the convection losses from the surface are not substantial as mentioned earlier.
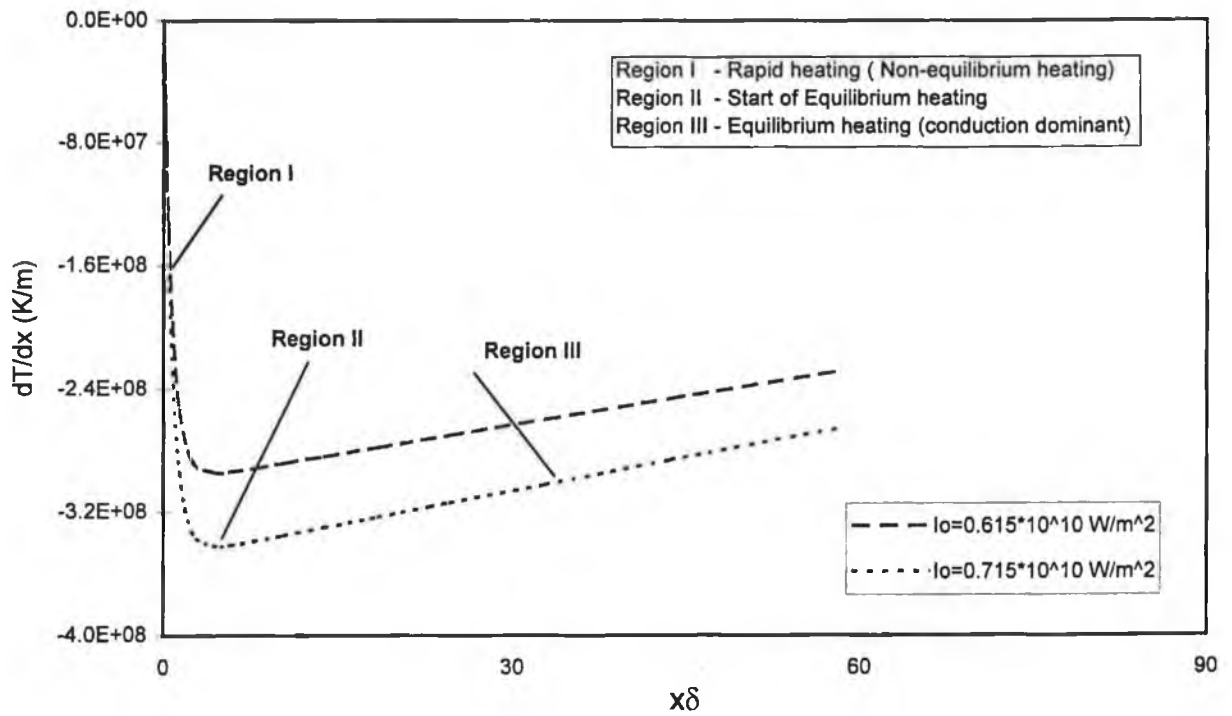
Figure-4.11   Variation of dT/dx with dimensionless distance (xδ) predicted from the theory.
I_0 is the laser power intensity ($\delta = 10^6$ 1/m).
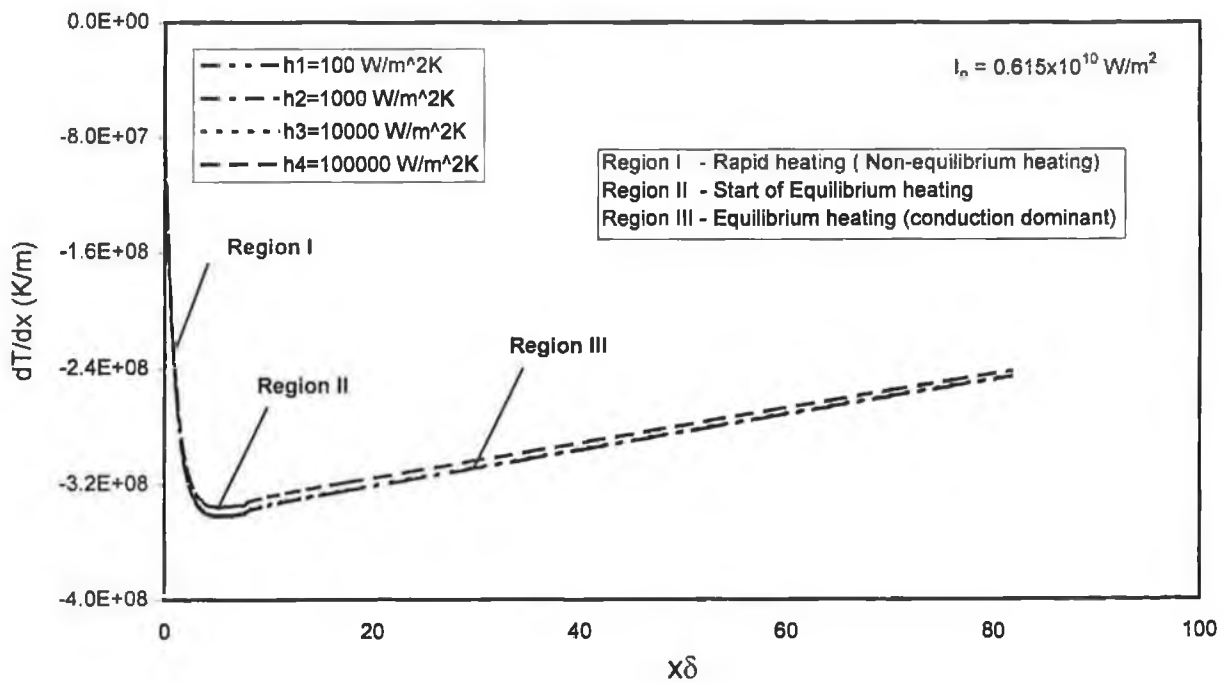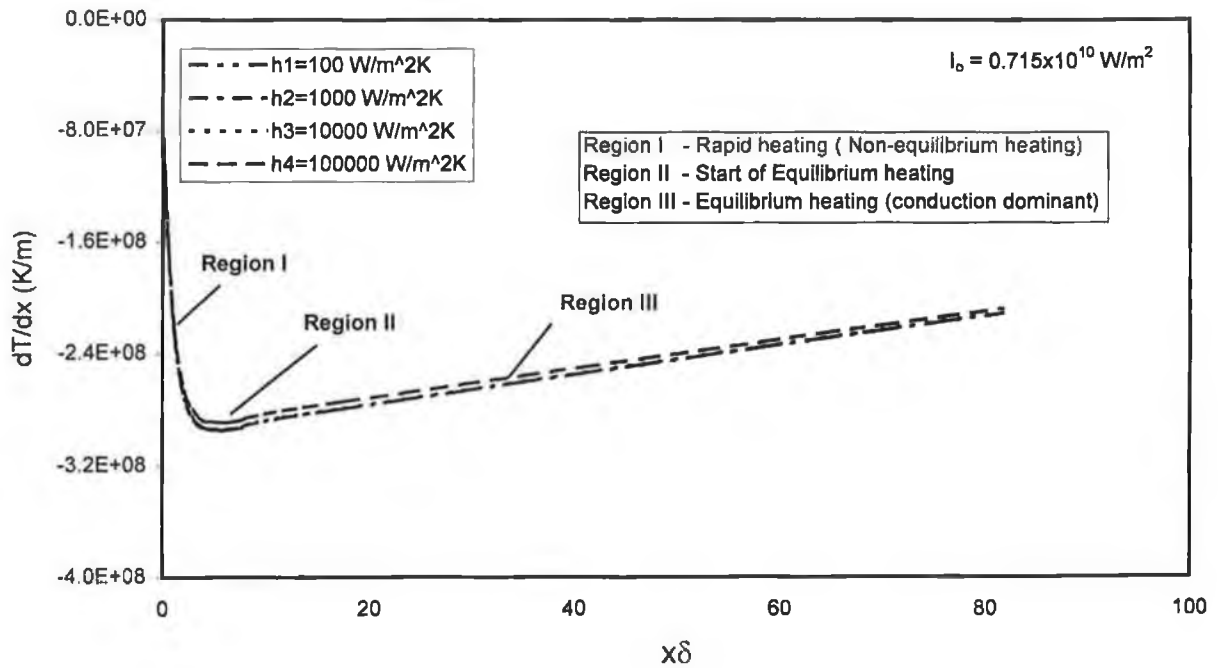Using Equation No. 3.10 when x >= 0.

Figure-4.12   Variation of dT/dx with dimensionless distance (xδ) predicted from the theory.
I_0 is the laser power intensity and h is the heat transfer coefficient.
Using Equation No. 3.40 when x >= 0.

Figure-4.13   Variation of dT/dx with dimensionless distance (xδ) predicted from the theory
I_0 is the laser power intensity and h is the heat transfer coefficient.
Using Equation No. 3.40 when x >= 0.

4.2 Plasma Nitriding Workpieces

SEM results for plasma nitrided samples are shown in figures (4.14a & b). Three distinct zones are evident from the photograph (figure (4.14a)). These include a compound layer (layer a), an inner layer (layer b) and an outer layer (layer c). The interface between layer 'a' and layer 'b' is sharp, while that between layer 'b' and layer 'c' is diffused. The thickness of these layers extends to 10 μm for the compound layer, 15 μm for the inner layer and 40 μm for the outer layer. These layers are composed of different nitride phases. The nitrided samples exhibit diffraction lines belonging to δ–TiN and ε–Ti$_2$N phases. The weight fraction of these phases varies within the nitrided layer and indicates that the concentration of the delta phase decreases with increasing depth while the α–Ti concentration increases. In layer 'a' the ε–Ti$_2$N + δ–TiN phases occur. The intermediate layer 'b', however, is composed of a nitrogen solution in titanium, α–(Ti,N), with or without ε–phase occurring. In between layers 'a' and 'b', a very thin layer is developed. This possesses δ and ε–phases. The creation of this layer may be due to a homogeneous reaction taking place in the early stages of the nitriding process, which forms TiN in the plasma layer deposits it on the surface. Consequently, the compound layer is composed of a δ–phase outermost layer, followed by a very thin inner layer containing ε and δ–phases. In layer 'c' precipitates occur near layer 'b'. The precipitates become dominant as the distance from layer 'b' increases to base material. This may be due to the fact that as the distance from the surface increases, the diffusion process-taking place along the grains slows down and becomes dynamically non-uniform. This is also evident from figure (4.14b). Considering the nitrogen concentration profile in the

99

matrix, the nitride formation will first occur on the substrate surface, due to the foremost encounter of the high nitrogen content. Once the maximum nitriding is reached, the crystallites lattice stage changes towards the face- centered cubic (f.c.c.).
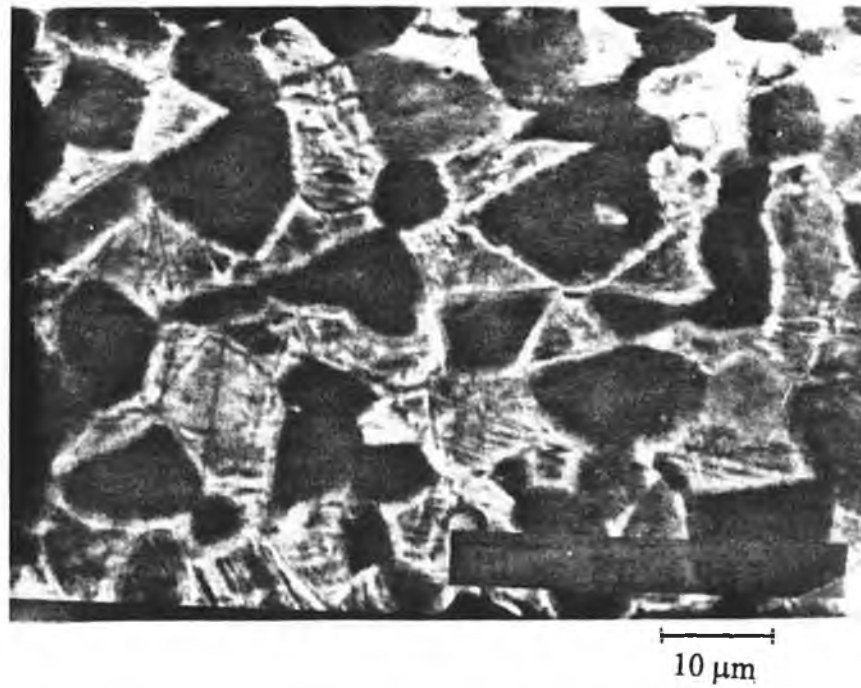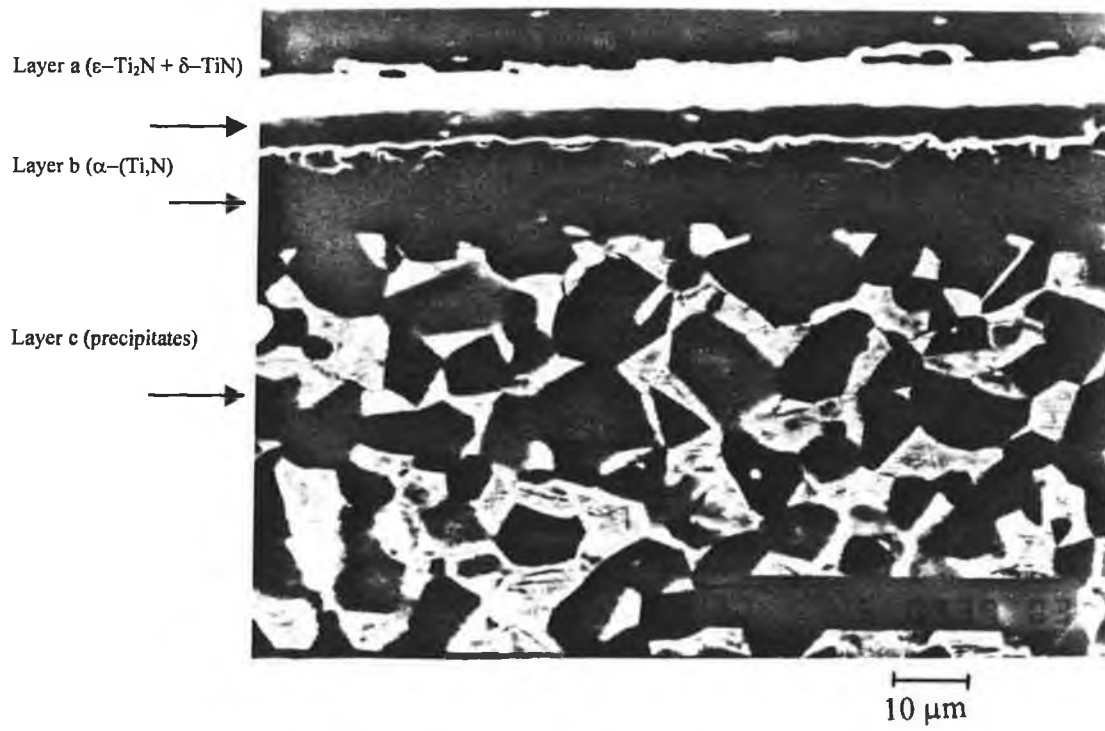
Layer a (ε–Ti_2N + δ–TiN)

Layer b (α–(Ti,N))

Layer c (precipitates)

10 μm

10 μm

Figure-4.14a and b   SEM photographs of plasma nitrided cross sectional
Temperature = 520 ^{o}C; Pressure = 0.5 kPa; Time = 65 ks

101

4.3 Microstructure

The micrographs of initially nitrided and laser-melted Ti-6Al-4V alloy are shown in figure (4.15). It may be seen that two melting regions exist close to the surface. In the first region, the substrate is heated to a temperature considerably higher than the melting temperature. In the second region, the workpiece temperature is slightly higher than the melting temperature. Consequently, these regions are called high and low melting regions, respectively. The demarcation zone between these regions is visible from the microphotograph (figure 4.15). The structure is dendritic in the heat-affected zone next to the low melting region.
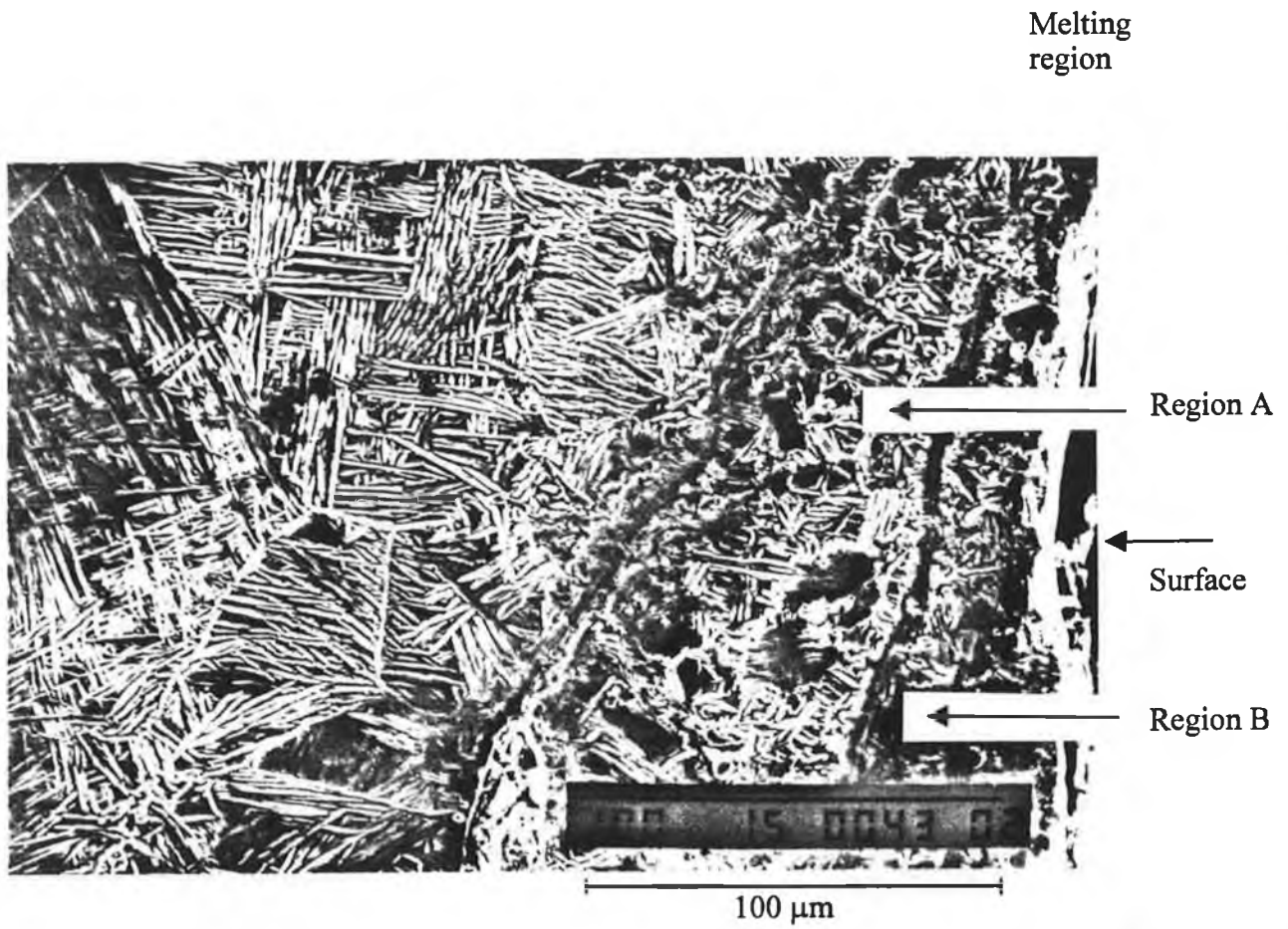
Figure-4.15   SEM micrograph of initially plasma nitrided and later laser melted of workpieces. Laser power intensity = 1.2 kW; Traverse speed = 0.6 m/min

In the high melting region, which is close to the surface, the oxide formation is evident in figure (4.16). The grain sizes are very small due to the rapid solidification in the vicinity of the surface It should be noted that the surface cools at a relatively higher rate than the bulk, due to the convection effect. In the low melting region, the grains are relatively larger in size, compared with high melting region. In general, the high melting region consists of cellular fractures. Moreover, it is expected that the nitride compounds almost disappear due to the heating effect in the case of high melting region. Since the melting was carried out under shielding gas of nitrogen, the effect of oxygen is minimal.
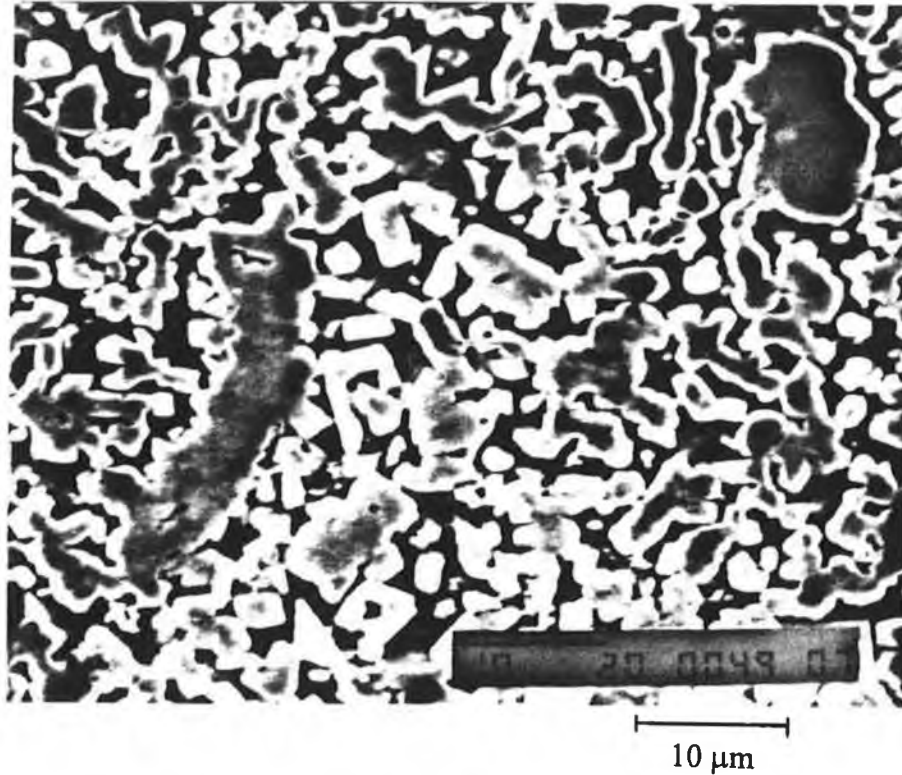
10 μm

Figure-4.16   High melting region occur close to surface
(Region A in figure 4.15)
Laser power intensity = 1.2 kW
Traverse speed = 0.6 m/min

The micro-cracks and some micro-holes, do however occur in the high melting region (figure 4.17). This may be to due to the attainment of a high cooling rate during the solidification, which in turn results in considerable stress development in this region. In addition, rapid solidification, because of the high cooling rate, results in the formation of an acicular α-phase, which is finer than the platelike α–phase. A prior β–phase grain boundary may be observed. In the case of low melting region, the cooling rate is lower than that corresponding to the high melting region.
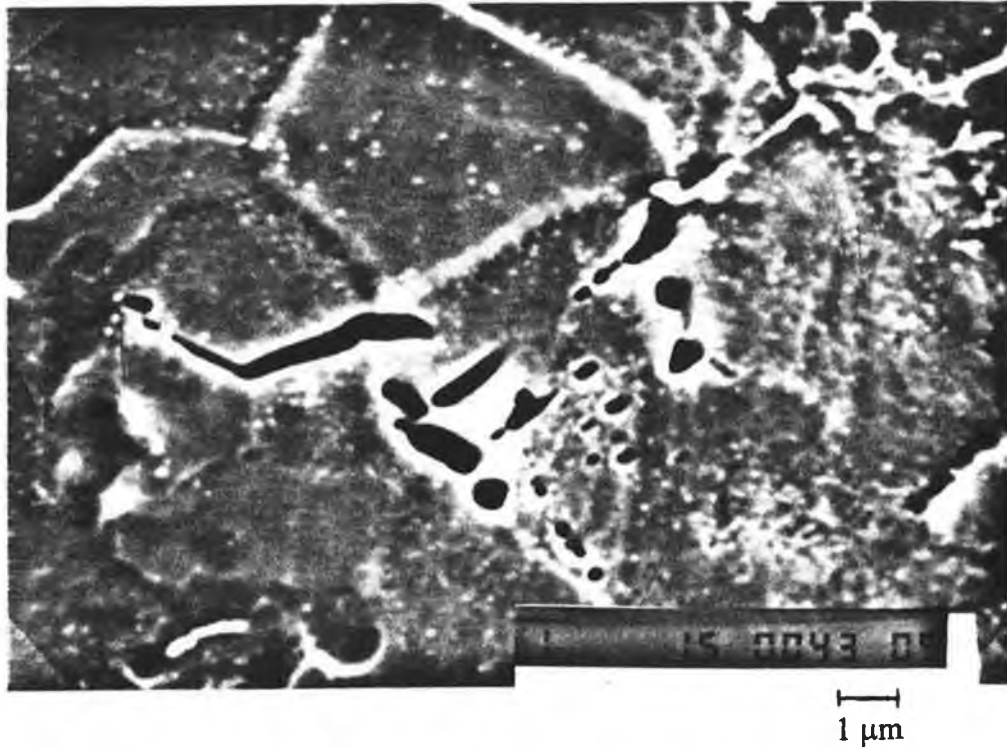
1 µm

Figure-4.17   Micro-cracks and micro-holes occur in high melting region
(Region B in figure 4.15). Laser power intensity = 1.2 kW
Traverse speed = 0.6 m/min

The structure, therefore, consists of transformed β–phase containing acicular α-phase (α–phase at prior β–phase grain boundaries), as observed in figure (4.18).
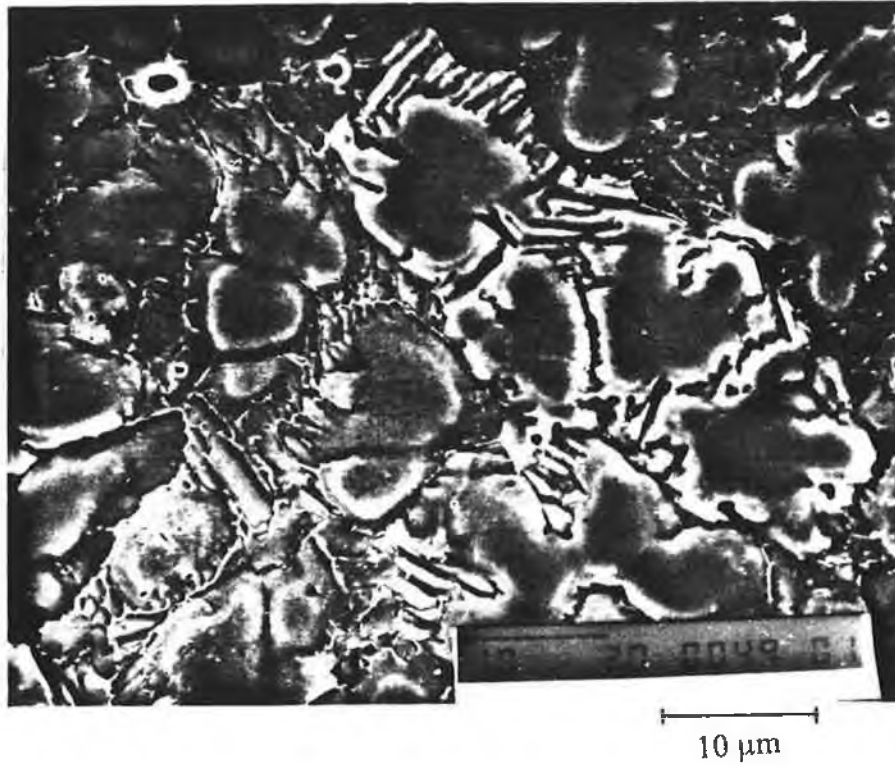
10 μm

Figure-4.18   Structure consists of transformed β–phase containing acicular α–phase

In the vicinity of the heat-affected zone, the structure containing transformed β–phase comprised of coarse phase and a fine acicular α-phase could be seen in figure (4.19). In the heat-affected zone, however, primarily the α' martensite is formed. Moreover, α+β microstructure can be seen next to heat-affected zone, i.e., the unaffected region consists of α+β microstructure. In general, laser treated surfaces consists of cellular and dendritic structures, i.e. at high cooling rates cellular structures are evident and being obscured by α– martensite.
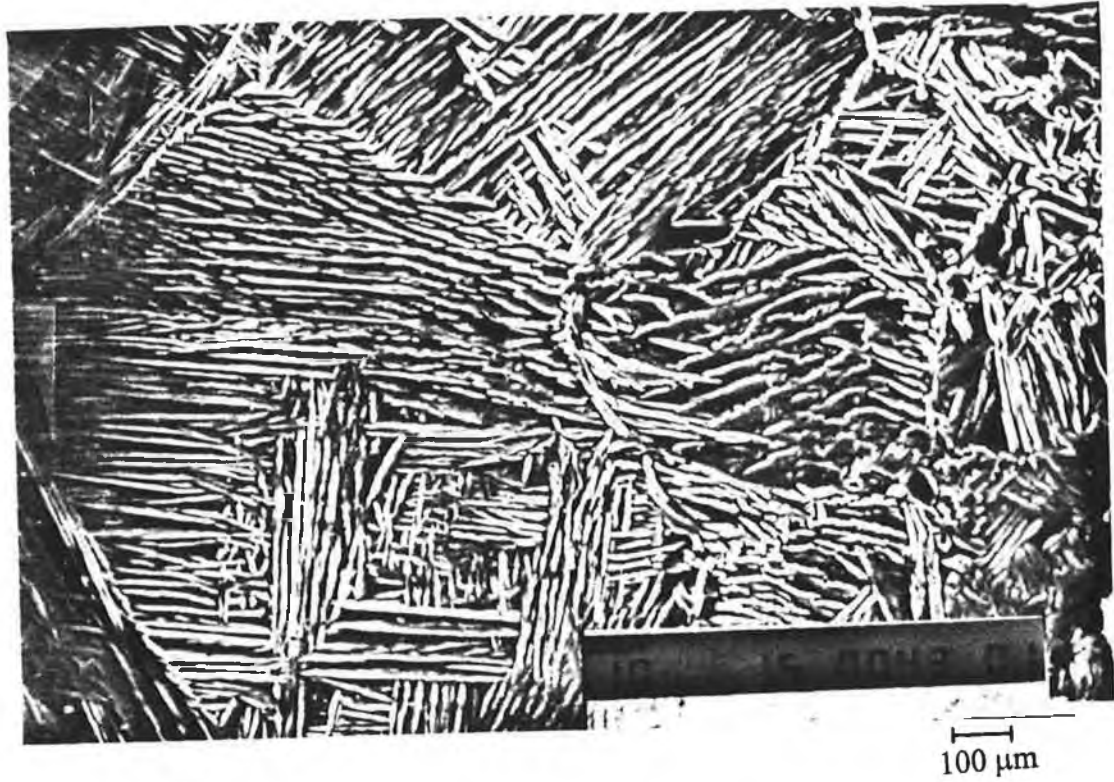
Figure-4.19   Structure containing transformed β–phase comprised of coarse phase.

4.4 Wear Tests

A visual inspection of the test samples showed that, for short nitriding times, the surface turns a bright yellow color. When the process time is increased, the surface changes to a bright golden color. When the temperature and nitriding time is increased, the sample surface turned to a darker color.

The friction coefficient test results are shown in figure (4.20). The results were obtained from the ball-on-disk wear experiment described in section 2.7. The effect of plasma nitriding can be clearly seen. For the untreated samples, severe scuffing-like wear was observed to occur on the surface after only a few wear cycles, whereas the nitrided samples displayed smooth wear characteristics for prolonged periods. It is also evident that the friction coefficient, after being relatively constant for a period at the start of the test, increases abruptly before breakthrough occurrs. The plasma nitrided surfaces give the lowest friction coeffeicent, followed by nitrided/laser-melted and untreated surfaces. Some scuffing-like wear occurred for the untreated workpieces after only few wear cycles.
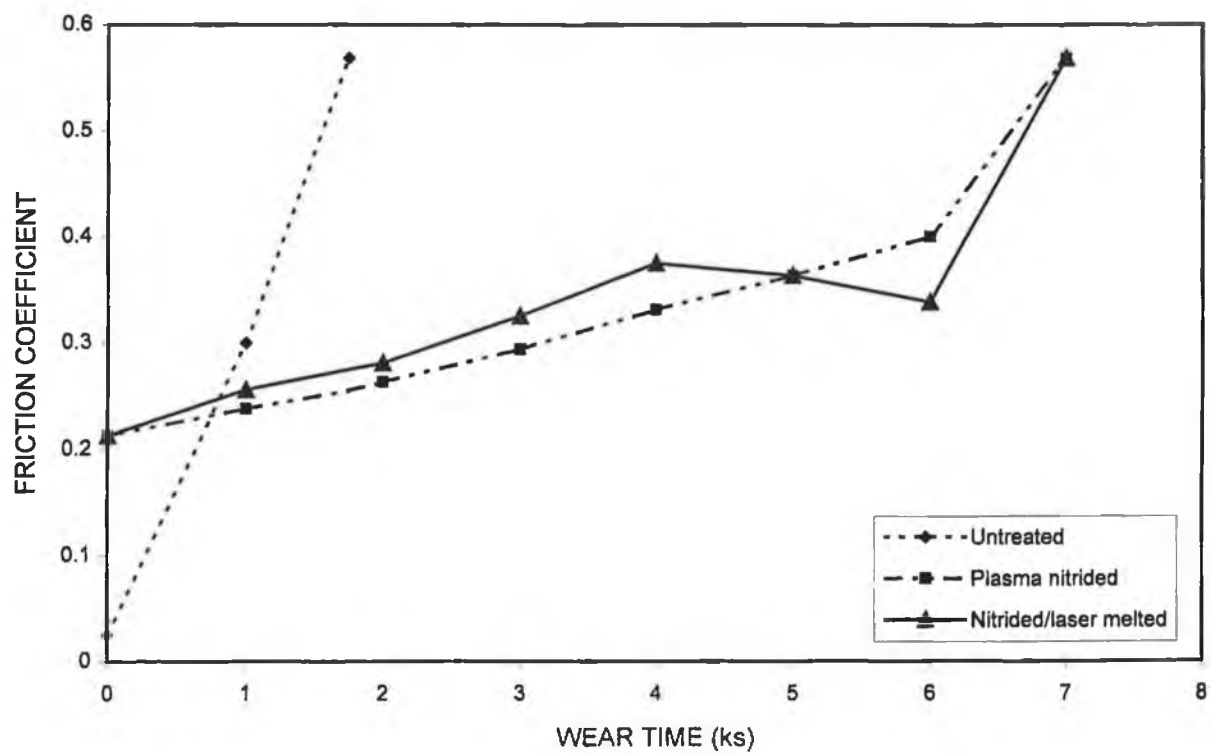
Figure-4.20   Variation of friction coefficient with wear time.

The variation of wear depth, resulting from the pin-on-disc tests, as a function of the number of cycles is shown in figure (4.21) for untreated, plasma-nitrided and nitrided/laser-melted workpieces. Three stages can be distinguished. The first stage corresponds to depth from zero to 0.75 KÅ below the surface. In this case, 30% of the total cycles take place for this region. In the second stage, scratch depth varies from 0.75 to 1.1 KÅ. This takes place 30%–90% of wears cycles. This indicates that the second stage contributes significantly to the wear resistance improvement since 60% of the wear time is spent in this region. The last stage exhibits the fastest wear rate of the three stages. In this case, rapid wear occurs during the last 10% of the cycle time. Wear behavior of the untreated sample is considerably poor.
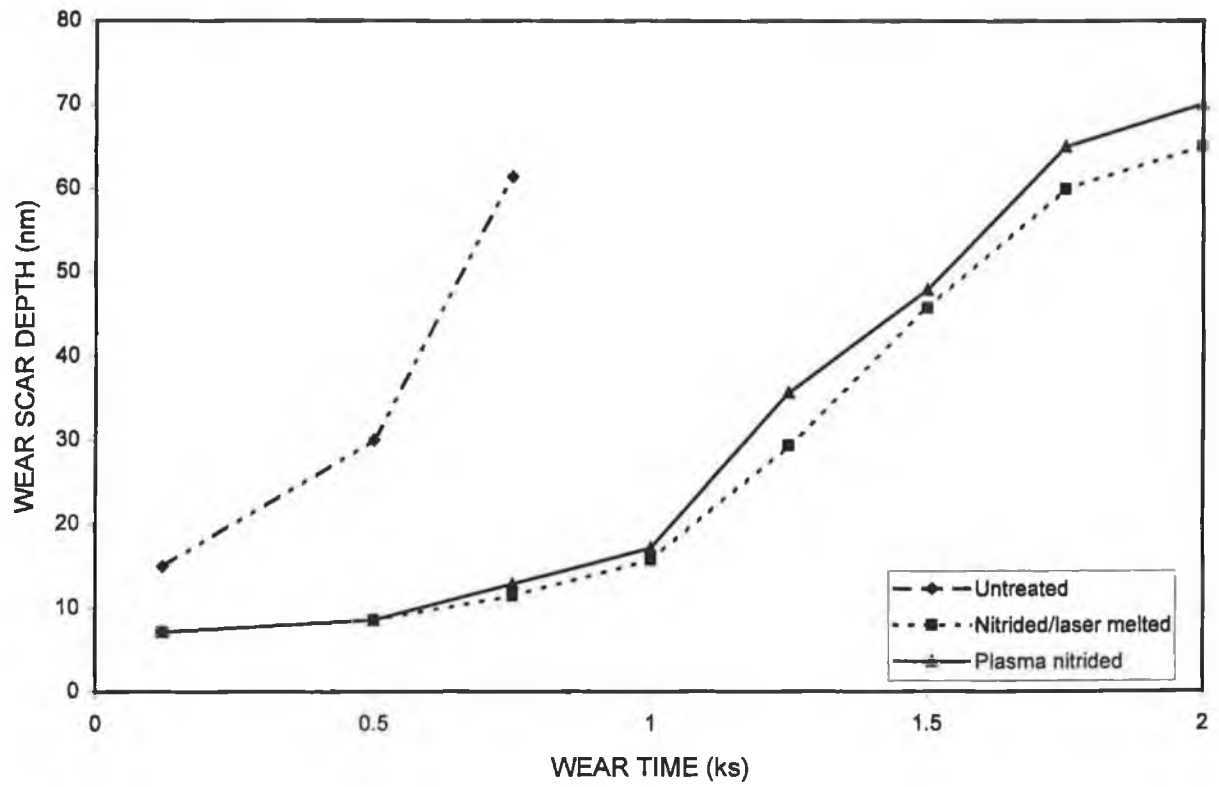
Figure-4.21   Variation of wear scar depth with wear time.

Figure (4.22) shows the variation of the cross sectional area of wear scars with number of cycles. It is evident that high temperature nitriding gives a better wear resistance than that corresponding to low temperature nitriding and untreated samples. This may be due to the elevated sample temperature, which increases the diffusion rate during nitriding process. High temperature nitriding results improved wear resistance. This may be related to nitrogen concentration in the surface region. The wear resistance of titanium nitride is much better than that of untreated sample and, therefore, it is reasonable to expect that the peak in the nitrogen concentration profile and minimum wear rate should coincide at the same depth. This difference may be explained in terms of the geometrical configuration of pin-on-disc wear tester. In this case, when the apex of the pin is at a given depth, the large area of the contact surface is at small depths. When the majority of the wear, therefore, takes place at depths around the nitrogen peak, the apex of the pin must pass the nitrogen peak and the minimum wear rate exceeds the depth of the nitrogen concentration peak.
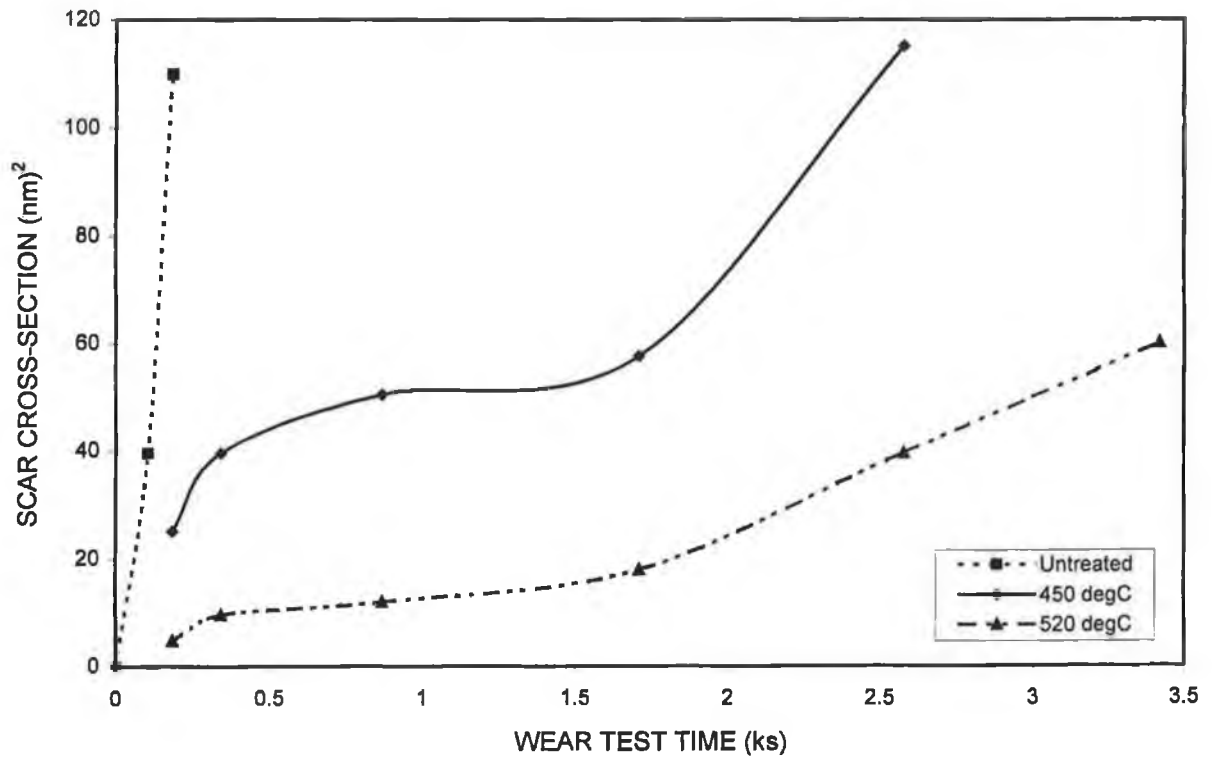
Figure-4.22   Scar cross-section versus wear test time for
Plasma nitrided workpiece at two different
temeprature ranges.

The surface of the workpieces obtained from the wear tests for nitrided/laser melted and untreated workpieces are given in figure (4.23). The plasma nitrided/laser-melted surface exhibits in reduced depth of scar marks compared to the untreated sample surface. The scratch size is almost uniform for the untreated surface. This scratch appearance, however, becomes non-uniform for the treated workpiece. The low wear resistance of the untreated workpiece is due to the $\alpha+\beta$ structures in the surface region of the untreated workpiece. The scratches developed at the untreated surface are deeper than the plasma nitrided and nitrided/laser melted surfaces. However, the surface damage is minimal in the case of plasma nitrided workpiece. The mechanism of material removal in all cases are almost the same involving flake formation and slip fragmentation which is consistent with early work [28].
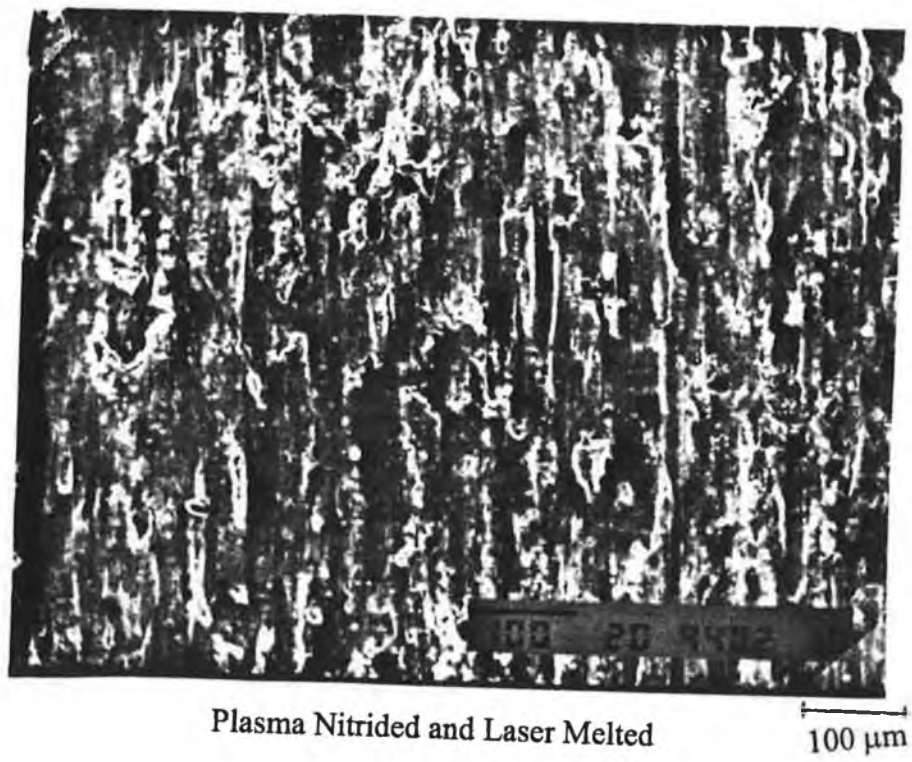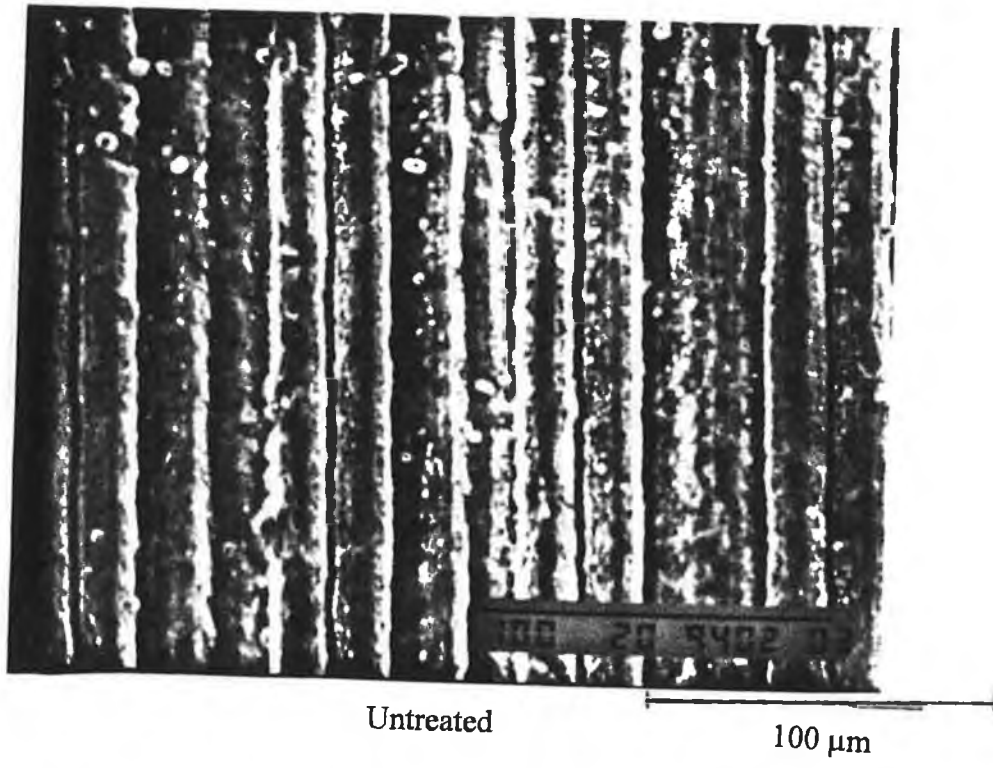
Untreated

100 μm

Plasma Nitrided and Laser Melted

100 μm

Figure-4.23   SEM microphotograph of cross-section of TiN coated sample.

119

4.5 Micro-hardness Measurement

The micro-hardness test results are shown in figure (4.24). The micro-hardness results include plasma-nitrided and plasma nitrided/laser-melted workpieces. Micro-hardness decreases with increasing distance from the surface. It should be noted that when nitrogen forms a solid solution as a consequence of nitriding in the alloy, it results in hardening dislocation pinning effects. Consequently, this dislocation pinning effect increases with increasing temperature. In addition, an increase in temperature increases the nitrogen diffusion process [36].

As the distance from the surface increases (outermost region), the original microstructure is dendritic, in which case the hardness increases slightly from the base material. In the case of nitride/laser-melted workpieces, the hardness obtained across the cross-section is slightly lower than that corresponding to the plasma-nitrided workpieces. This indicates that the deficiencies in nitride species is expected to give low hardness, but formation of a finer martensitic structures, due to laser-melting overcomes this and increases the hardness. In the region close to the workpiece surface the micro-hardness increases to a maximum, in which case, the laser-heated surface produces a structure comprising of smaller prior β grains and the transferred β changes from α' to the basket wave structure. In addition, the amount of α precipitation on the prior β phase grains boundaries is increased. In the low melting region, the micro-hardness reduces slightly. This is due to the fact that the structure consists of large prior β grains, which have transformed to martesite, together with a small amount of grain boundary α.
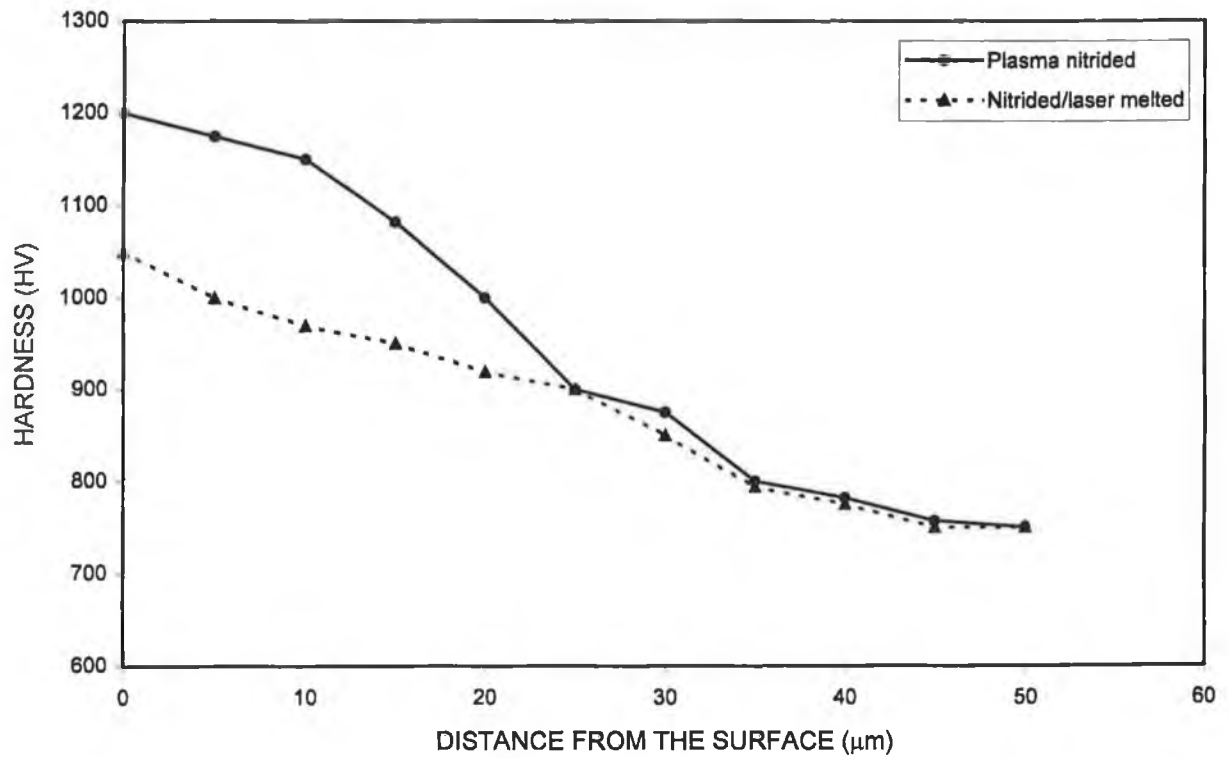
Figure-4.24   Variation of micro-hardness with distance
below the surface for plasma nitrided and nitrided/laser melted workpieces.

Figure (4.25) shows EDS spectrum, while Table-4.1 gives the elemental distribution in nitriding/laser-melted and untreated regions. It can be seen that aluminum is depleted in the high melting region. In addition, the titanium depletion in both high and low melting regions is small. The depletion in aluminum may be attributed to its low melting and evaporation temperatures. In this case, it is expected that aluminum may be ejected due to the melt pressure developed in the high melting region.

	Ti	Al	V	Cu	Cr	Fe	O
No treatment	Balance	6	4	0.03	0.01	0.32	0.20
Laser melted Low-melt region	Balance	5	4	0.03	0.01	0.32	unknown
Laser melted High-melt region	Balance	3	4.5	0.03	0.01	0.32	unknown

Table-4.1   Elemental Distribution in Plasma Nitrided and Laser Melted Regions

Figure-4.25   EDS Spectrum of Ti-6Al-4V alloy
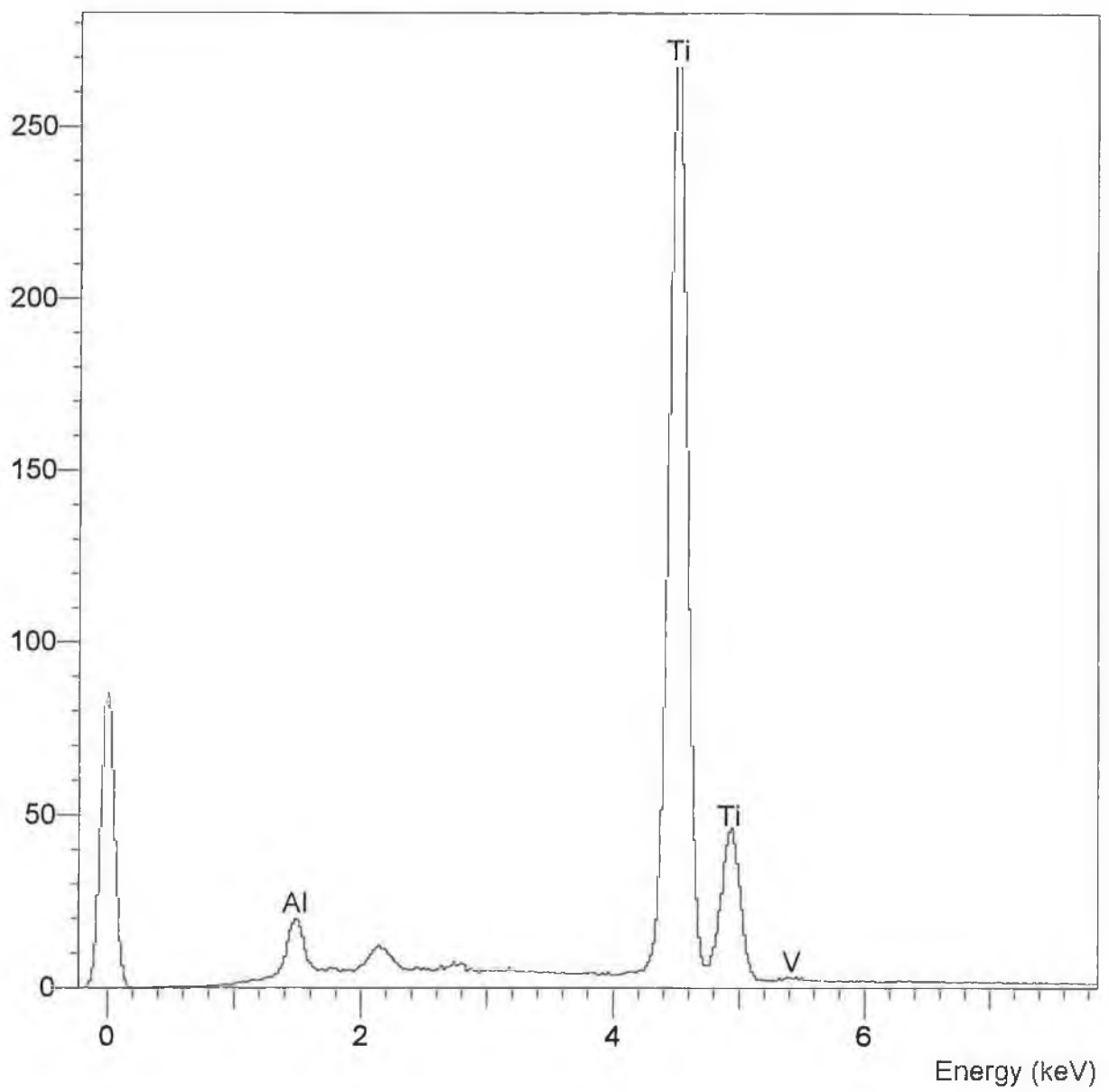
The XRD results as shown in figure (4.26) show that the structure of the nitrided samples exhibited diffraction lines belonging to δ–TiN and ε–Ti$_2$N phases. The weight fractions of these phases vary within the nitrided layer and indicate that the concentration of the δ–phase decreases with increasing depth while the α–Ti concentration increases.

untreated

(202) (004) (201) (112) (200) (103) (110) (102) (101) (002) (100)

plasma nitrided

1 2 3 4 5 6 7 8 9 10 11

1	2	3	4	5	6	7	8	9	10	11
ε–Ti2N (302)	δ–TiN (222)	δ–TiN (311)	ε–Ti2N (202)	ε–Ti2N (311)	ε–Ti2N (102)	δ–TiN (220)	ε–Ti2N (002)	δ–TiN (200)	δ–TiN (111)	ε–Ti2N (101)

Diffraction angle (2 theta)

Figure-4.26   XRD Results for plasma nitrided sample

125

4.6   PVD Coating Samples

The SEM photograph of cross-sections of a TiN coated sample is shown in figure (4.27). For the TiN coated samples a homogeneously distributed coat is obtained and the coat thickness extends to 2 μm.
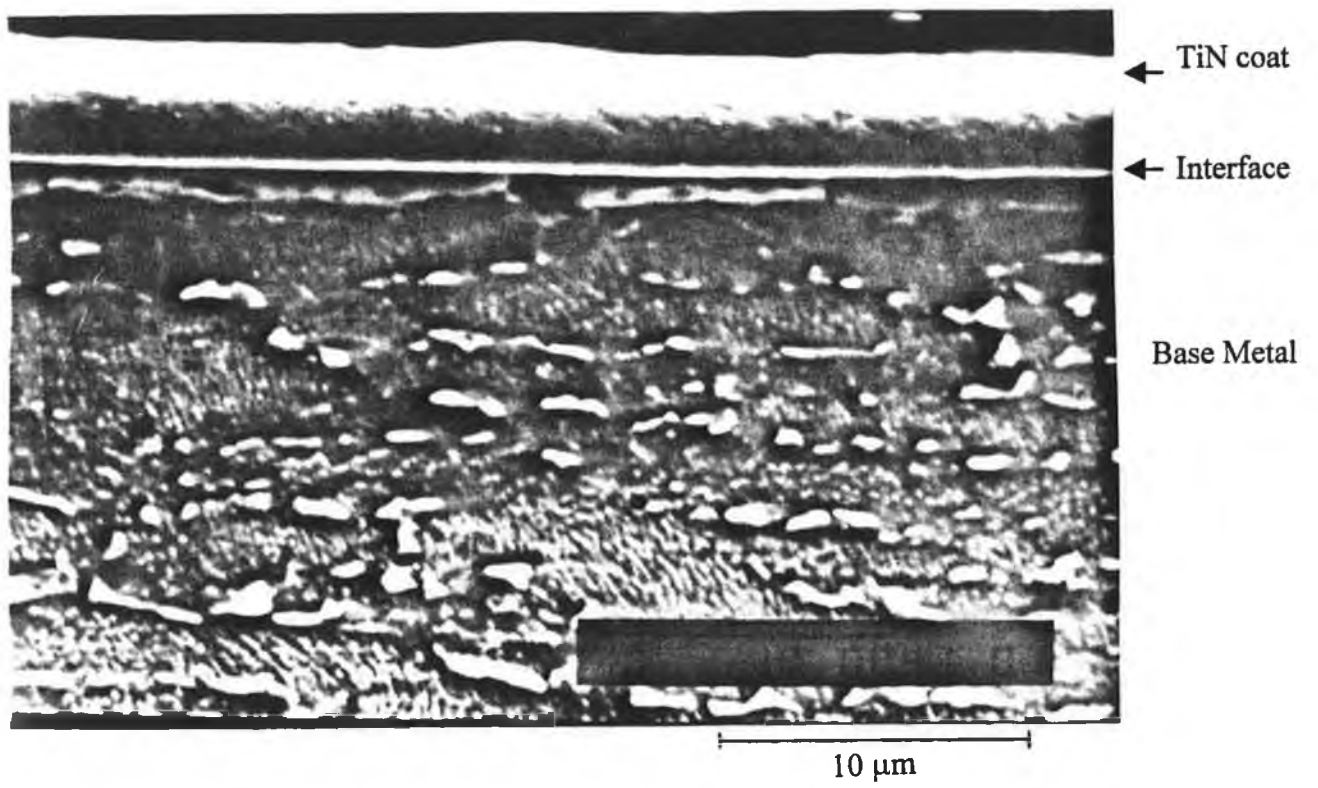
Figure-4.27   SEM microphotograph of cross-section of TiN coated sample.

Figure (4.28) shows the wear test results obtained under different loading conditions. The wear plots show that wear occurs more slowly in coated samples compared to uncoated workpieces. For coated workpieces, an abrupt change in wear depth occurs during the sliding tests. The wear depth, however, increases continuously for uncoated workpieces. This may suggest a transition between two distinct stages of wear in coated workpieces. Moreover, during the initial stage, the measured wear depth shows relatively small increase with increasing sliding time. However, as the sliding time increases, the initial wear stage changes to a second stage in which case the wear scar size increases rapidly. The wear scar size is shown in figure (4.29) for two normal loads. The wear scar size increases as the sliding time increases, however, the rate of increase in scar size accelerates after a certain sliding time. In this case, two distinct wear behavior patterns are possible as discussed for figure (4.28).
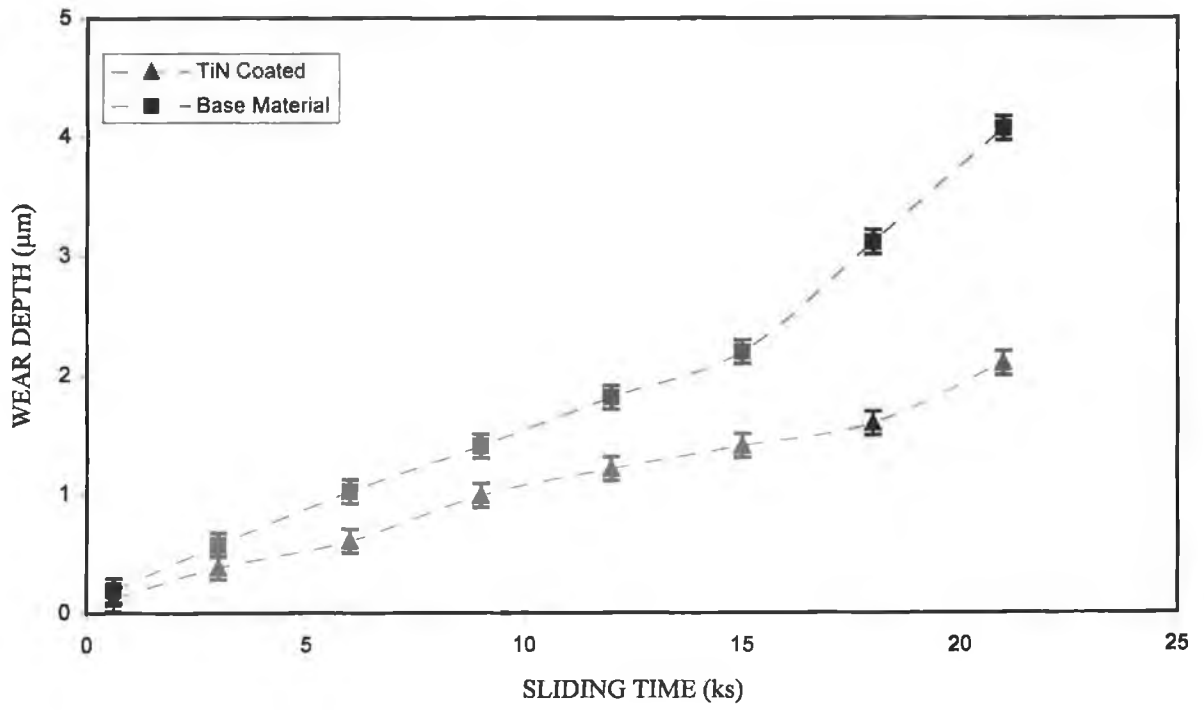
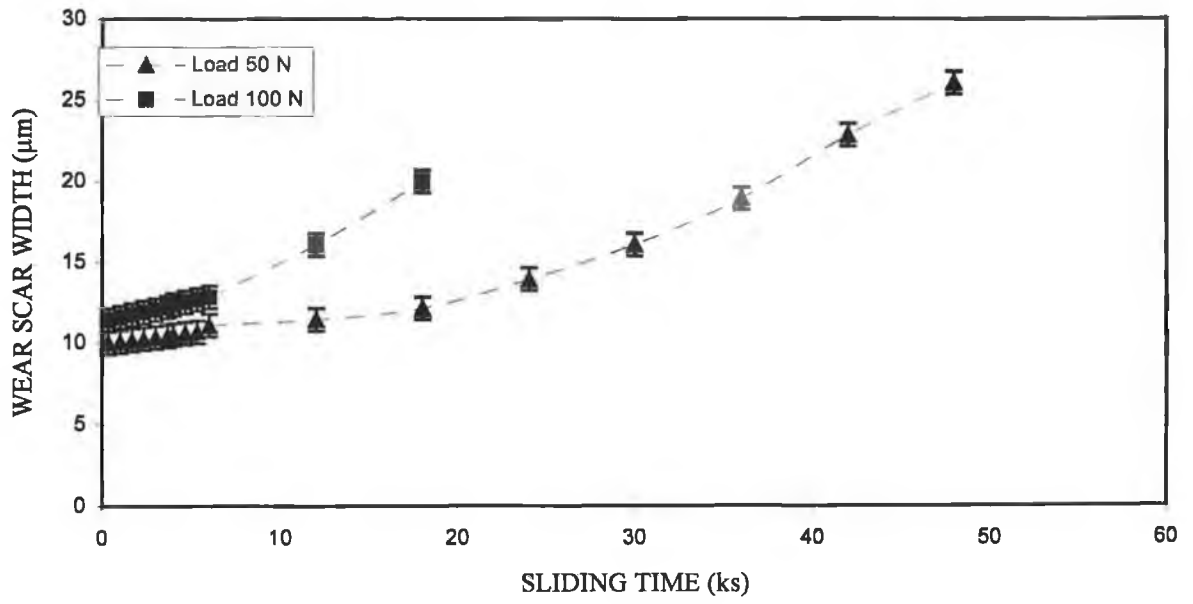Figure-4.28   Wear depth with sliding time for a normal load of 50 N.

129

Figure-4.29   Wear scar width with sliding time for two normal load
conditions, for TiN coated workpieces.

When examining the wear surfaces after various durations of wear, the transition of wear appearance was revealed, which may also be evident from figure (4.30). It is apparent from the cross section of the worn surfaces that the thinning of the coat layer occurs in the early stage of the wear. The fine scratches or furrows appearing on the wear surface, however, they may also indicate the presence of abrasive wear in the direction of sliding. Prolonged wear resulted in the exposure of the substrate material in the wear scars. Furthermore, the substrate appearance starts at the central region of the wear scar where the stress is higher. It later extends rapidly up to the circumference of the scar. In the case of the second stage of the wear, the material is removed both from the substrate and the circumferentially remaining coating layer. Moreover, the rate of wear increases rapidly since the material removal from the substrate is quicker than that corresponding to coated layer. However, the coat fractured, during wear test, does not peal-off from the surface. This may be due to the one or all of the following reasons. (i) the adhesion of the coated layer on the base material is considerable due to nitride interface between the coat and the substance, and (ii) on abrupt change in elastic module of coat and base material occur, in this case, nitride interface acts as a transition zone between the coat and the base material.
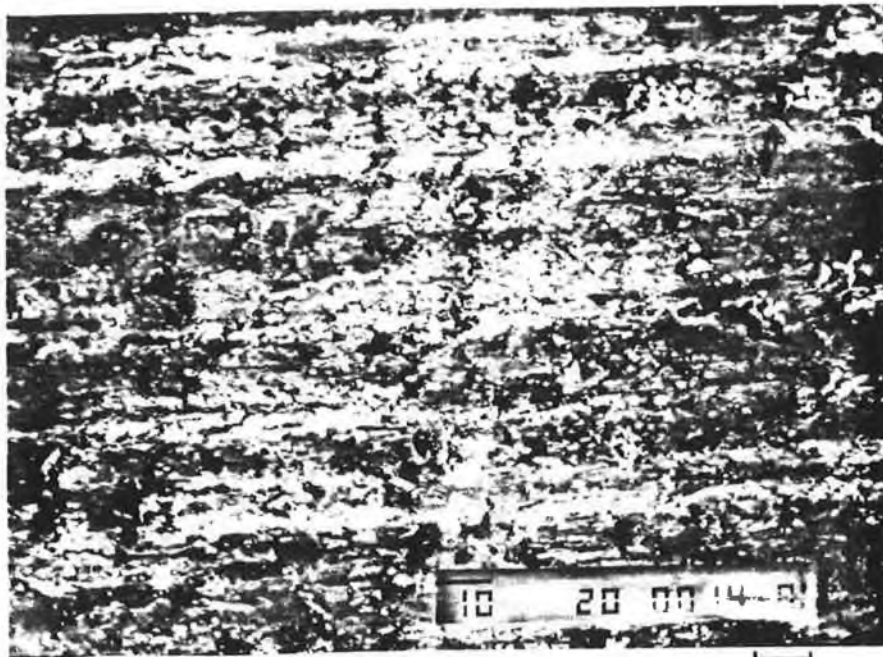
Top view

Surface   10 μm
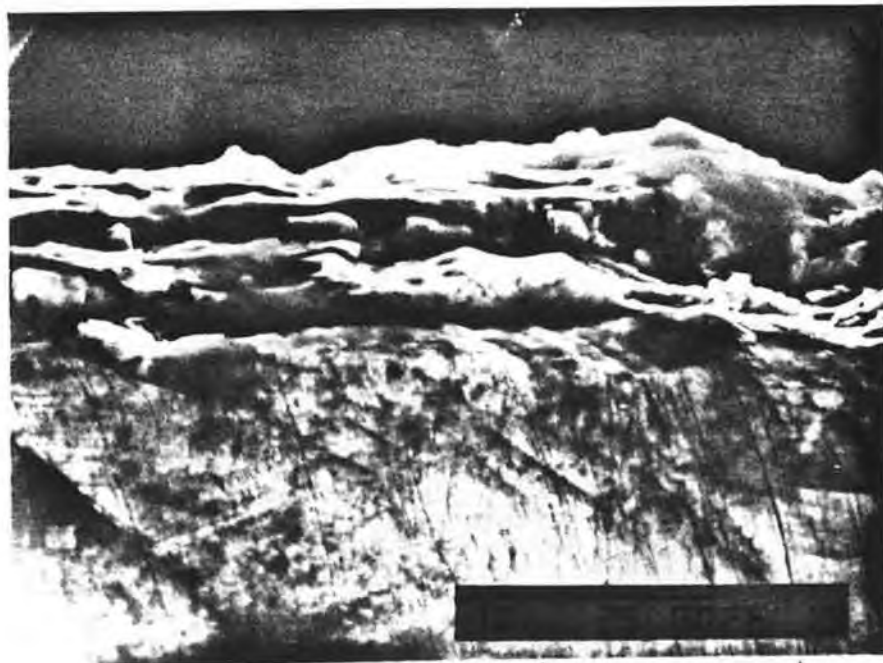
Coat

Thining of
TiN

Cross-section   10 μm

Figure-4.30 Top and Cross Sectional View of the TiN coated Workpiece

Figure (4.31) shows a typical change of friction coefficient with sliding time. The friction coefficient remains almost constant for sometimes, however, an increase in the friction coefficient occurs as the scars developed at the surface. It may be seen from the friction coefficient curve that in the initial stage of the friction test the friction coefficient appears to be the same for all workpiece surfaces. However, as the test duration increases only the untreated surface show an increase in the friction coefficient.
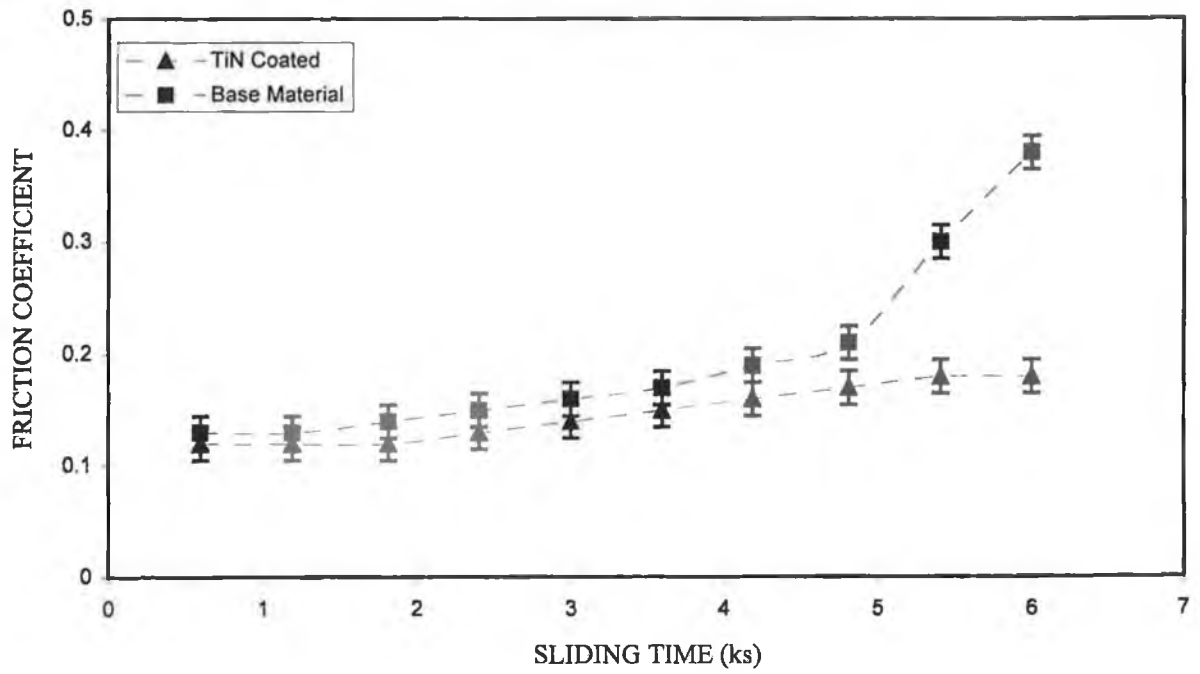
Figure-4.31   Friction coefficient with sliding time (Load = 100 N).

CHAPTER- 5

Conclusions and Future work

5.1 Conclusions

The conclusions derived from the present study are given as follows: -

1. Theoretical predictions pointed out that when the melting temperature is reached, the liquid temperature in the high melting region rises. The region in which the melting occurs at the saturation liquid temperature, however, is called the low melting region. Moreover, the equilibrium point may be attained during the heating cycle. In this case, convective and conduction losses balance the energy gain by the substance via laser radiation.

2. The laser power intensity has considerable influence on the resulting temperature profile, i.e., temperature attains high values at high power intensities.

3.   The heat transfer coefficient on the resulting temperature profiles has negligible effect. In this case, convective losses are minimal compared with internal energy gain of the substrate.

4.   The nitrided samples exhibit diffraction lines of δ-TiN and ε-Ti$_2$N phases. As the depth increases, the concentrations of the ε-Ti$_2$N increases while the concentration of the δ-phase decreases.

5.   The results of plasma nitriding demonstrate that three distinct layers develop in the nitrided zones in the vicinity of the surface, namely: inner, intermediate and outer layers. The thickness of these layers extends to 10 μm for the compound layer, 15 μm for the intermediate layer and 40 μm for the outer layer. These include compound layer (ε-Ti$_2$N + δ-TiN phases occurring in the inner layer) and α-(TiN) phases with or without ε-Ti$_2$N phases occurring in the intermediate layer. In the outer layer, the nitride precipitates are dominant and distributed evenly at a location close to the intermediate layer. Precipitates occur at the lower end of this layer. After laser heating process, however, the nitride species almost disappear, which are especially true for high melting regions. The oxide compound is not seen since the laser melting process was carried out at shielding ambient.

6.   In general due to the high cooling rate, plasma nitrided/laser-melted workpieces consist of cellular and dentritic structures. The cellular structures are evident and are being obscured by α' martensite. At relatively low cooling

rates, however, the structure consists of transformed β containing acicular α: α at prior β grain boundaries.

7. Due to the high cooling rate, the rapid solidification produces acicular α. In the case of low melting regions, however, the structure consists of transformed β containing acicular α: α at prior β grain boundaries can be observed. The heat affected zone possesses primarily α' martensite. As it is expected, α+β microstructure is evident in the unaffected region. Cellular and dentritic structures occur in the nitriding/laser-melted regions. The dentiritic region of the nitrided workpiece, however, consists of TiN.

8. The wear resistance depends mainly on the compounds formed at the surface and their resistance to abrasion. It is clear from the photographic observations that the scratches developed at the untreated surface are deeper than those corresponding to the plasma nitriding and nitrided/laser-melted surfaces. Furthermore, a sharp boundary exists between the high and low melting regions. The surface damage is minimal, however, in the case of the plasma nitrided workpiece. Plasma nitrided/laser-melted surfaces give a considerable increase in the wear properties.

9. The lowest friction coefficient occurs at the surfaces of the plasma nitrided, followed by plasma nitrided/laser-melted and untreated surfaces.

10. The resulting profiles from the micro-hardness test show that the trends of the hardness obtained across the cross-section of the nitrided sample are slightly

lower than that for the plasma nitrided/laser-melted sample. This indicates that the deficiency in nitride species is expected to give low hardness, but the formation of finer martensitic structures, due to laser melting, overcomes this and increases the hardness.

5.2 Future work

The future work may be listed as follows: -

- The duplex treatment of the workpieces can be considered. In this case, pre-plasma nitriding before TiN PVD coating can be carried out. This may improve the adhesion of the coat on to the substrate.

- Laser assisted nitriding can be taken into account. An experimental set-up can be designed and realized in this regard. This may provide cost-effective nitriding of the workpieces.

- Corrosion properties of the plasma nitrided and PVD coated workpieces can be investigated.

REFERENCES

[1] E. Lang, Coatings for High Temperature Applications, Applied Science Publishers, 1983.

[2] S. Grainger, Engineering Coatings-Design and Application, Abington Publishing, 1989.

[3] B. L. Mordike, "State of the Art of Surface Engineering with High Energy Beams", Key Engineering Materials, Vol. 46 and 47, pp. 13-26, 1990.

[4] D.T. Quinto, G.J. Wolfe and P.C. Jindal, "High Temperature Micro-hardness of Hard Coatings Produced by Physical and Chemical Vapour Deposition", Thin Solid Films, Vol. 153, pp. 19-36, 1987.

[5] H.K. Pulker, Wear and Corrosion Resistant by CVD and PVD, Ellis Horwood-Publishers, 1989.

[6] J. Musil, L. Bardos, A. Rajsky, J. Vyskocil, B. Dolezal, G. Loncar, K. Dadourek and V. Kubicek, "TiN_x Coatings Prepared by D.C. Reactive Magnetron Sputtering", Thin Solid Films, Vol. 136, pp. 229-239, 1986.

[7] S. Kanamori, "Investigation of Reactively Sputtered TiN Films for Diffusion Barriers", Thin Solid Films, Vol. 136, pp. 229-239, 1986.

[8] B. Rauschenbach, "Formation of Compounds by High-Flux Nitrogen Ion Implantation in Titanium", Journal of Materials Science, Vol. 21, pp. 395-404, 1986.

[9] E. Erturk and H.J. Heuvel, "Adhesion and Structure of TiN Arc Coatings", Thin Solid films, Vol. 153, pp. 135-147, 1987.

[10] K. Ichii, K. Fujimura and T. Takase, "Sputtering, Deposition and Diffusion in Ion-Nitriding of an Austenitic Stainless Steel", Materials Science and Engineering, A140, pp. 442-447, 1991.

[11] R.A. Swady, H.A. Ja'fer and R.P. Howson, "The Reactive Sputtering of Thin Films of TiN at Low Target Voltages", Vacuum, Vol. 44, No. 3-4, pp. 297-301, 1993.

[12] X. Huang J. Cuddy, N. Goel and N.L. Richards, "Effect of Heat Treatment on the Microstructure of a Metastable β–Titanium Ally", Journal of Materials Engineering and Performance, Vol. 3, No. 4, pp. 560-566, 1994.

[13] N.F. Mott and H. Jones, Theory of the Properties of Metals and Alloys, Dover Publication, London, 1978.

[14] M.Y. Al-Jaroudi, H.G.T. Hentzell and J. Valli, "The Influence of the TiN Deposition Temperature on the Critical Load and Hardness of Hardened Steels", Thin Solid Films, Vol. 154, pp. 425-429, 1987.

[15] N. El-Tayeb, "The Variation of Hardness and Wear Coefficient in Sliding wear of Copper and Aluminium Alloys", Wear, Vol. 174, pp. 63-69, 1994.

[16] M. V. Stappen, L.M. Stals, M. Kerkhofs and C. Quaeyhaegens, "State of the Art for the Industrial Use of Ceramic PVD Coatings", Surface and Coatings Technology, Vol. 74-75, pp. 629-633, 1995.

[17] T. Wierzchon, J. Rudnicki, M. Hering and R. Niedbala, "Formation and Properties of Nitrided Layers Produced in Pulsed Plasma at a Frequency Between 100 and 600 kHz", Vacuum, Vol. 48, No. 6, 1997.

[18] P. Hedenqvist and S. Hogmark, "Experiences from Scratch Testing of Tribological PVD Coatings", Tribology International, Vol. 30, No. 7, pp. 507-516, 1997.

[19] O. Knotek, T. Leyendeclcer and F. Jungblut, "On the Properties of Physically Vapour-Deposited Ti-Al-V-N Coatings, Thin Solid Films, Vol. 153, pp. 83-90, 1987.

[20] W. Mader, H.F. Fischmeister and E. Bergmann, "Defect Structure of Ion-Plated Titanium Nitride Coatings", Thin Solid Film, Vol. 182, pp. 141-152, 1989.

[21] P. Stevenson and A. Matthews, "PVD Equipment Design: Concepts for Increased Production Throuhput", Surface and Coatings Technology, Vol. 74-75, pp. 770-780, 1995.

[22] M.M. Tosic, I. Terzic and R. Gligorijevic, "Plasma Nitriding of Powder Metal Steel", Vacuum, Vol. 40, No. ½, pp. 131-134, 1990.

[23] Y. Sun and T. Bell, "Plasma Surface Engineering of Low Alloy Steel", Materials Science and Engineering, A140, pp. 419-434, 1991.

[24] M.M. Tosic and R. Gligorijevic, "Plasma nitriding Improvements of Fatigue Properties of Nodular Cast Iron Crankshafts", Materials Science and Engineering, A140, pp. 469-473, 1991.

[25] M.B. Karamis and R. Ipek, "An Evaluation of the Using Possibilities of the Carbonitrided Simple Steels Instead of Carburized Low Alloy Steels (Wear properties)", Applied Surface Science, Vol. 119, pp. 25-33, 1997.

[26] S. Yerramareddy and S. Bahadur, "Effect of Operational Variables, Microstructure and Mechanical Properties on the Erosion of Ti-6Al-4V", Wear, 142, pp. 253-263, 1991.

[27] M.V. Stappen, B. Malliet, L. Stals, L. D. Schepper, J.R. Roos and J.P. Celis, "Characterization of TiN Coatings Deposited on Plasma Nitrided Tool Steel Surfaces", Materials Science and Engineering, A140, pp. 554-562, 1991.

[28] M. Ignatiev, E. Kovalev and I. Melekhin, "Investigation of the Hardening of a Titanium Alloy by Laser Nitriding", Wear, 166, pp. 233-236, 1993.

[29] A. Schulz, H.R. Stock and P. Mayr, "Physical Vapour Deposition of TiN Hard Coatings with Additional Electron Beam Heat Treatment", Materials Science and Engineering, A140, pp. 639-646, 1991.

[30] M. Zlatanovic, T. Gredic, N. Popovic and Z. Bogdanov, "Matching of TiN Coating Structures by Plasma Nitriding of Substrates", Vacuum, Vol. 44, No. 2, pp. 83-88, 1993.

[31] D. G. Konitzer, B. C. Muddle, H. L. Fraser and R. Kircheim, "Titanium, Science and Technology", Vol. 1, Ed. By G. Lutgering, U. Zwicker and W. Burak (DGM, Oberusel, West Germany), pp. 405-410, 1985.

[32] J.C. Wiliams, "Titanium Technology: Present Status and Future Trends", Eds. F.H. Froes, T. Eylon and H.B. Bomberger, Titanium Development Association, pp. 75-86, 1985.

[33] K.G. Budinski, "Tribological Properties of Titanium Alloys", Wear, Vol. 151, pp. 203-217, 1991.

[34] R. Grun and H. Gunther, "Plasma Nitriding in Industry Problems, New Solutions and Limits", Materials Science Engineering, Vol. 140, pp. 435-441, 1991.

[35] N. Laidani, J. Perriere, D. Lincot, A. Gicquel and J. Amauroux, "Nitriding of Bulk Titanium and Thin Titanium Films in a NH3 Low Pressure Plasma", Appl. Surface Science, Vol. 36, pp. 520-529, 1989.

[36] A. Gicquel, N. Laidani, P. Saillard and I. Amauroux, "Plasma and Nitrides: Application to the Nitriding of Titanium", Pure and Appl. Chem., Vol. 62, No. 9, pp. 1743-1750, 1990.

[37] J.F. Lin and J.H. Horng, "Analysis of the Tribological Behaviour and Wear Mechanisms of Titanium Nitride Coating", Wear 171, pp. 59-69, 1994.

[38] J. Kourtev, R. Pascova and E. Weibmantel, "A Modified Method for Arc Deposition of Ti-N Thin Films", Vacuum, Vol. 48, No. 1, pp. 7-12, 1997.

[39] J. Folhers, D.R.F. West and W.M. Steen, "Laser Surface Melting and Alloying of Titanium", Laser Surface Treatment of Metals, pp. 451-460, 1986.

[40] O.V. Akgun and O.T. Inal, "Laser Surface Modification of Ti-6Al-4V Alloy", Journal of Materials Science, Vol. 29, pp. 1159-1168, 1994.

[41] B.S. Yilbas and M. Sami, "Laser Melting of Ti-15Al-20Nb Alloy", Journal of Materials Engineering and Performance, Vol. 5, No. 1, pp. 124-128, 1996.

[42] T. Bell, M.H. Sohi, J.R. Betz and A. Bloyce, "Energy Beams in Second Generation Surface Engineering of Aluminum and Titanium Alloys", Key Engineering Materials, Vols. 46 and 47, pp. 69-84, 1990.

[43] B.S. Yilbas, A.Z. Sahin, M. Sami, A. Goban and R. Bozdogan, "Study into Laser Heating of Ti-14Al-21Nb Alloy to Improve Properties", Optics and Laser in Engineering, Vol. 23, pp. 53-64, 1995.

[44] H. Xin, S. Mridha and T.N. Baker, "The Effect of Laser Surface Nitriding with a Spinning Laser Beam on the Wear Resistance of Commercial Purity Titanium", Journal of Materials Science, Vol. 31, pp. 22-30, 1996.

[45] M. Toyal and K. Mukherjee, "Thermal and Microstructural Analysis for Laser Surface Hardening of Steel", J.of Appl. Phys., V. 75, N. 8, pp.3855-3861, 1994.

[46] M. Osawa, "Improving the Corrosion Resistance of Cast Iron by Laser Surface Melting", Corrosion Engineering, Vol. 45, pp. 25-34, 1996.

[47] B. Malliet, J.P. Celis, J.R. Roose, L.M. Stals and M. V. Stappen, "Wear Phenomena in the System TiN-Coated High Speed Steel Disk Against a Chromium Steel Pin", Wear, Vol. 142, pp. 151-170, 1991.

[48] G. Fischer, G.E. Welsch, M-C. Kim and R.D. Schieman, "Effect of Nitrogen Ion Implantation on Tribological Properties of Metallic Surfaces", Wear, Vol. 146, pp. 1-23, 1991.

[49] I.L. Singer, S. Fayeulle and P.O. Ehni, "Friction and Wear Behavior of TiN in Air: The Chemistry of Transfer Films and Debris Formation", Wear, Vol. 149, pp. 375-394, 1991.

[50] R.F. Huang, L.S. Wen, L.P. Guo, J. Gong B.H. Yu and H. Bangert, "Micro-Structural and Indentation Characterization of Ti/TiN Multilayer Films", Surface and Coatings Technology, Vol. 50, pp. 97-101, 1992.

[51] A. Mucha and M. Braun, "Requisite Parameters for Optimal Wear Performance of Nitrogen-Implantted Titanium and Ti-6Al-4V", Surface and Coatings Technology, Vol. 50, pp. 135-139, 1992.

[52] A. Chen, J. Blanchard, S.H. Han, J.R. Conrad, R.A. Dodd, P. Fetherston and F.J. Worzala, "A Study of Nitrogen Ion-Implanted Ti-6Al-4V ELI by Plasma Source Ion Implantation at High Temperature", Journal of Materials Engineering and Performance, pp. 845-848, 1992.

[53] G.M. Mehrotra, V.K. Jain, H.M. Urdianyk and B.D. Barton, "Effect of Ion Implantation on Friction and Wear Behavior of Steels", Wear, Vol. 159, pp. 47-55, 1992.

[54] Y.L. Su, J.S. Lin, L.I. Shiau and J.D. Wu, "A Tribological Investigation of Physical Vapour Deposition TiN Coatings Paired with Surface Treated Steels for Machine Element Applications", Wear, Vol. 167, pp. 73-83, 1993.

[55] E. Vancoille, J.P. Celis and J.R. Roos, "Dry Sliding Wear of TiN Based Ternary PVD Coatings", Wear, Vol. 165, pp. 41-49, 1993.

[56] Y.L. Su and J.S. Lin, "An Investigation of the Tribological Potential of TiN, CrN and TiN+CrN Physical Vapor Deposited Coatings in Machine Element Applications", Wear 170, pp. 45-53, 1993.

[57] K.J. Yoon, S.J. Cho, S.S. Kim, M.S. Yoon and S.H. Yang, "Wear Mechanism of TiN-Coated High-Speed Steel During Sliding", Wear 170, pp. 101-108, 1993.

[58] G.H. Shehata and A.M.A. Moussa, "Nd: YAG Laser Alloying of High-Speed Steel Tools with BN and Ti/BN and the Effects on Turning Performance", Wear 170, pp. 199-210, 1993.

[59] M.V. Stappen, M. Kerkhofs, C. Quaeyhaegens and L. Stals, "Introduction in Industry of a Duplex Treatment Consisting of Plasam Nitriding and PVD Deposition of TiN", Surface and Coatings Technology, Vol. 62, pp. 655-661, 1993.

[60] Z.P. Huang, Y. Sun and T. Bell, "Friction Behaviour of TiN, CrN and (TiAl)N Coatings", Wear 173, pp. 13-20, 1994.

[61] S. Hogmark and P. Hedenqvist, "Tribological Characterization of Thin, Hard Coatings", Wear 179, pp. 147-154, 1994.

[62] N. Dingremont, E. Bergmann, P. Collignon and H. Michel, "Optimization of Duplex Coatings Built from Nitriding and Ion Plating with Continuous and Discontinuous Operation for Construction and Hot Working Steels", Surface and Coatings Technology, Vol. 72, pp. 163-168, 1995.

[63] D. Muller, Y.R. Cho and E. Fromm, "Adhesion Strength of Ductile Aluminium and Brittle TiN Coatings on Steel, Aluminium and Copper, Measured by Fracture Mechanics Tests", Surface and Coatings Technology, Vol. 74-75, pp. 849-856, 1995.

[64] I. Milosev, H.-H. Strehblow and B. Navinsek, "XPS in the Study of High-Temperature Oxidation of CrN and TiN Hard Coatings", Surface and Coatings Technology, Vol. 74-75, pp. 897-902, 1995.

[65] F. Alonso, A. Arizaga, S. Quainton, J.J. Ugarte, J.L. Viviente and J.I. Onate, "Mechanical Properties and Structure of Ti-6Al-4V Alloy Implanted with

Different Light Ions", Surface and Coatings Technology, Vol. 74-75, pp. 986-992, 1995.

[66] M. Larsson, M. Bromark, P. Hedenqvist and S. Hogmark, "Deposition and Mechanical Properties of Multilayered PVD Ti-TiN Coatings", Surface and Coatings Technology, Vol. 76-77, pp. 202-205, 1995.

[67] K.J. Ma, A. Bloyce and T. Bell, "Examination of Mechanical Properties and Failure Mechanisms of TiN and T-TiN multilayer Coatings", Surface and Coatings Technology, Vol. 76-77, pp. 297-302, 1995.

[68] E.J. Bienk, H. Reitz and N.J. Mikkelsen, "Wear and Friction Properties of Hard PVD Coatings", Surface and Coatings Technology, Vol. 76-77, pp. 475-480, 1995.

[69] J. Zhou and S. Bahadur, "Erosion-Corrosion of Ti-6Al-4V in Elevated Temperature Air Environment", Wear 186-187, pp. 332-339, 1995.

[70] J.M. Robinson and R.C. Reed, "Water Droplet Erosion of Laser Surface Treated Ti-6Al-4V", Wear 186-187, pp. 360-367, 1995.

[71] C. Gerdes, A. Karimi and H.W. Bieler, "Water Droplet Erosion and Microstructure of Laser-Nitrided T-6Al-4V", Wear 186-187, pp. 368-374, 1995.

[72] B.S. Yilbas, A.Z. Sahin, S.A.M. Said, J. Nickel and A Goban, "Investigation into Some Tribological Properties of Plasma Nitrided Hot-Worked tool Steel AISI H11", Journal of Materials Engineering and Performance, Vol. 5(2), pp. 220-224, 1996.

[73] A. Kobayashi, " Surface Nitridation of Titanium Metal By Means of a Gas Tunnel Type plasma Jet", Journal of Materials Engineering and Performance, Vol. 5(3), pp. 373-382, 1996.

[74] B.S. Yilbas, A. Coban, J. Nickel, M. Sunar, M. Sami and B.J. Abdul-Aleem, "Investigation into Nitrided Spur Gears", Journal of Materials Engineering and Performance, 5, pp. 728-733, 1996.

[75] Y.Y. Guu, J.F. Lin and C-F. Ai, "The Tribological Characteristics of Titanium Nitride Coatings, Part-I, Coating Thickness Effects", Wear 194, pp. 12-21, 1996.

[76] Y.Y. Guu and J.F. Lin, "The Tribological Characteristics of Titanium Nitride Coatings, Part-II, Comparisons of Two Deposition Processes", Wear 194, pp. 22-29, 1996.

[77] H.S. Kwok, H.S. Kim, D.H. Kim, W.P. Shen, X.W. Sun and R.F. Xiao, "Correlation Between Plasma Dynamics and Thin Film Properties in Pulsed Laser Deposition", Applied Surface Science 109/110, pp.595-600, 1997.

[78]   H.U. Krebs, M. Stormer, S. Fahler, O. Bremert, M. Hamp, A. Pundt, H. Teichler, W. Blum and T.H. Metzger, "Structural Properties of Laser Deposited Metallic Alloys and Multilayers", Applied Surface Science 109/110, pp.563-569, 1997.

[79]   Z. Xingzhong, L. Jiajun, Z. Baoliang, M. Hezhuo and L. Zhenbi, "Wear Mechanisms of Ti (C,N) Ceramic in Sliding Contact with Stainless Steel", Journal of Materials Science 32, pp.2963-2968, 1997.

[80]   G.D. Davis, G.B. Groff and R.A. Zatorski, "Plasma Spray Coatings as Treatments for Aluminum, Titanium and Steel Adherends", Surface and Interface Analysis, Vol.25, pp.366-373, 1997.

[81]   M. Scholl, "Abrasive wear of Titanium Nitride Coating", Wear 203-204, pp. 57-64, 1997.

[82]   A. Molinari, G. Straffelini, B. Tesi, T. Bacci and G. Pradelli, "Effects of Load and Sliding Speed on the Tribological Behaviour of Ti-6Al-4V plasma Nitrided at Different Temperatures", Wear 203-204, pp. 447-454, 1997.

[83]   S. Novak and M. Komac, "Wear of Cermet Cutting Tools Coated with Physically Vapour Deposited TiN", Wear 205, pp. 160-168, 1997.

[84]   J. Khedkar, A. S. Khanna and K. M. Gupt, " Tribological Behaviour of Plasma and Laser Coated Steels", Wear 205, pp. 220-227, 1997.

[85]   A. Molinari, G. Straffelini, B. Tesi and T. Bacci, "Dry Sliding Wear Mechanisms of the Ti-6Al-4V Alloy", Wear 208, pp. 105-112, 1997.

[86]   R. S. De Sousa and C. Alves, "Overheating of Plasma-Nitrided Workpieces with Cylindrical Blind holes", Journal of Materials Engineering and Performance, Vol. 6(3), pp. 300-302, 1997.

[87]   S. Novak, M. Sokovic, B. Navinsek, M. Komac and B. Pracek, "On the Wear of TiN (PVD) Coated Cermet Cutting Tools", Vacuum, Vol. 48, No. 2, pp. 107-112, 1997.

[88]   C.V. Franco, L.C. Fontana, D. Bechi, A.E. Martinelli and J.L.R. Muzrt, "An Electrochemical Study of Magnetron-Sputtered Ti- and TiN-Coated Steel", Corrosion Science, Vol. 40, No. 1, pp. 103-112, 1998.

[89]   S. Kalpakjian, Manufacturing Process for Engineering Materials, 3rd ed., Addison-Welsley Publ. Company, 1997.

[90]   S.C. Lee, W.Y. Ho and T.M. Chen, "Prevention of Hydrogen Degradation in Titanium by Deposition of TiN Thin Film", Journal of Materials Engineering and Performance, Vol. 3, No. 6, pp. 740-743, 1994.

[91] K. D. Bruyn, J.P. Celis, J.R. Roos, L.M. Stals and M.V. Stappen, "Coating Thickness and Surface Roughness of TiN-Coated High Speed Steel in Relation to Coating Functionality", Wear, Vol. 166, pp. 127-129, 1993.

[92] R. E. Reed-Hill and R. Abbaschian, Physical Metallurgy Principles, 3rd ed., PWS Publ. Company, 1994.

[93] W. D. Callister, Material Science and Engineering, 3rd ed., John Wiley Sons, Inc., 1994.

[94] N. Zhang, W. Zhai, Y. Wang and A. Wagendristel, "X-ray Studies of Ti-N Coatings", Vacuum, Vol. 44, No. 1, pp. 51-53, 1993.

[95] G. Chryssolouris, Laser Machining, Theory and Practice, Springer-Verlag, 1991.

[96] M. Sami, Heat Transfer Mechanisms Governing Laser Metal Interactions, M.Sc., Mech. Eng. Dept., King Fahd University of Petroleum and Minerals, 1993.

[97] W.M. Steen, "Surface Coating Using a Laser", International Conference of Advances in Surface Coating Technology, London, Vol. 1, 1978.

[98] M.K. El-Adawi, M.A. Abdel-Naby and S.A. Shalaby, "Laser Heating of a Two-Layer System with Constant Surface Absorption: An Exact Solution", Int. J. Heat and Mass Trans., Vol. 38, pp. 947-952, 1995.

[99] D. Whitesed, R.E. Goffeith and M.N. Srinivdson, "The Effect of Laser Trimming on Properties of Ti-6Al-4V Sheet", Materials and Manufacturing Process, Vol. 10, No. 6, pp. 1201-1214, 1995.

[100] H. Czichos, Tribology, Elsevier Scientific Publishing Company, 1978.

[101] Y. Sun, T. Bell and G. Wood, "Wear Behaviour of Plasma-Nitrided Martensitic Stainless Steel", Wear, Vol. 178, pp. 131-138, 1994.

[102] R.T. Guiva, A.A. Levchenko, I.A. Tananko, V.A. Guiva and E.Y. Sittsevaya, "Enhancement of the Wear Resistance of Pieces Made of 30KhGSN2A and 38KhS Steels by Laser Treatment", Materials Science, Vol. 31, No. 5, pp. 105-109, 1195.

[103] D.A. Rigney, "Comments on the Sliding Wear of Metals", Tribology International, Vol. 30, No. 5, pp. 361-367, 1997.

[104] G.W. Critchlow, J. Hampshire, R. Kingdon, Z. Naeem, A.B. Smith and D.G. Teer, "Adhesion of Wear Resistant Hard Coatings to Steel Substrates", Tribology International, Vol. 30, No. 7, pp. 499-506, 1997.

[105] E-S. Yoon, H. Kong, O-K. Kwon and J-E. Oh, "Evaluation of Frictional Characteristics for a Pin-on-Disc Apparatus with Different Dynamic Parameters", Wear, Vol. 203-204, pp. 341-349, 1997.

[106] D.A. Rigney, "The Roles of Hardness in the Sliding Behaviour of Materials", Wear, Vol. 175, pp. 63-69, 1994.

[107] B.S. Yilbas, R. Davies and Z. Yilbas, "Surface Line and Plug Flow Models Governing Laser Produced Vapor from Metallic Surface", Pamana J. of Phys., Vol. 38, pp. 195-209, 1992.

[108] B. S. Yilbas and A. Z. Al-Garni, "Some Aspects of Laser Heating of Engineering Materials", Journal of Laser Applications, Vol. 8, pp. 197-204, 1996.

[109] C. Kittel, Introduction to Solid State Physics, 4th Ed. Wiley, New York, 1971.

[110] B.S. Yilbas, "Heating of Metals at a Free Surface by Laser Irradiation – an Electron Kinetic Theory Approach", Int. J. Engg. Sci., Vol. 24, No. 8, pp. 1325-1334, 1986.

[111] J.F. Ready, Industrial Applications of Lasers, Academic Press, New York, 1978.

[112] B.S. Yilbas and K. Apalak, "The Basic Concepts of Heat Transfer Mechanism During Laser Drilling of Metals", Egypt J. Phys., Vol. 18, No. 2, pp. 133-156, 1987.

[113] B.S. Yilbas and A.Z. Sahin, "Laser Heating Mechanism Including Evaporation Process", Int. Comm. In. Heat and Mass Trans., Vol. 21, pp. 509-518, 1994.

[114] B. S. Yilbas, A. Z. Sahin and R. Davier, "Laser Heating Mechanism Including Evaporation Process Initiating Laser Drilling", Int. J. Mech. Tools Manufact., Vol. 35, No. 7, pp. 1047-1062, 1995.

[115] B.S. Yilbas, PhD Thesis, Mech. Eng. Dept., University of Birmingham, 1980.

[116] H. Mingli, P.J. Bishop and A. Minardi, "Prediction of Cavity Shape and Material Removal Rates Using a Two-Dimensional Axisymmetric Heat Conduction Model for Fibrous Ceramic Insulation and Comparison with Experiment", J. of Laser Applications, Vol. 5, pp. 33-40, 1993.

[117] G. Simon, U. Gratzke and J. Kross, "Analysis of Heat Conduction in Deep Penetration Welding with a Time-Modulated Laser Pulse", J. Phys. D.: Appl. Phys., Vol. 26, pp. 862-869, 1993.

[118] B.S. Yilbas, "Analytical Solution for the Heat Conduction Mechanism Appropriate to the Laser Heating Process", Int. Comm. in Heat and Mass Transfer, V. 20, N. 4, pp. 545-555, 1993.

[119] B.S. Yilbas and M. Sami, "Heating Mechanism Including Evaporation Process-Semiclassical and Kinetic Theory Approaches", Jap. J. Appl. Phys., Vol. 34, pp. 6391-6400, 1995.

[120] B.F. Blackwell, "Temperature Profile in Semi-Infinite Body with Exponential Source and Convective Conditions, ASME J. of Heat Transfer, Vol. 112, pp. 567-571, 1990.

[121] P. Archambault and A. Azim, "Inverse Resolution of Heat-Transfer Equation: Application Steel and Aluminum Alloy Quenching", Journal of Materials Engineering and Performance, Vol. 4, pp. 730-736, 1995.

PAPERS IN CONFERENCE AND JOURNAL:

1. M.A. Mohammed, B.S. Yilbas and M.S.J. Hashmi, "Wear Properties of Plasma Nitrided and Laser Melted Ti-6Al-4V Alloy", International Conference of Advances in Materials & Processing Technologies -APMT'97.

2. M.A. Mohammed, M.S.J. Hashmi and B.S. Yilbas, "A Study Into Effects of CO_2 Laser Melting of Nitrided Ti-6Al-4V Alloy", ASM Journal of Materials Engineering and Performance, Vol. 6, No. 5, pp. 642-648, 1997.